ISSN 2348-0386

Journal of Aerospace Science and Applications

Volume No. 10
Issue No. 2
May- August 2025

ENRICHED PUBLICATIONS PVT.LTD

JE - 18,Gupta Colony, Khirki Extn,
Malviya Nagar, New Delhi - 110017.
E- Mail: info@enrichedpublication.com
Phone :- +91-8877340707

ISSN 2348-0386

Journal of Aerospace Science and Applications

Aims and Scope

The Journal of Aerospace Science and Applications published three issues yearly by Enriched publications. Journal of Aerospace Science and Applications is peer reviewed journal and monitored by a team of reputed editorial board members. This journal consists of research articles, reviews, and case studies on Aerospace Research. This journal mainly focuses on the latest and most common subjects of its domain.

Authors are invited to submit papers on new advances in the following topics to aerospace applications:

- Materials and structures
- Flight mechanics
- Navigation, guidance and control
- Electromagnetism and radar
- Signal and image processing
- Information processing
- Human behaviour
- Robotics and intelligent systems

ISSN 2348-0386

Journal of Aerospace Science and Applications

Managing Editor
Mr. Amit Prasad

ISSN 2348-0386

Journal of Aerospace Science and Applications

(Volume No. 10, Issue No. 2, May- August 2025)

Contents

ISSN 2348-0386

Single action control for oleo-pneumatic shock absorbers in CS-23 aircraft

Felix Willich a, , Jadran Vrabec b, , Florian Holzapfel a,
a Institute of Flight System Dynamics, Technical University Munich, Boltzmannstr. 15, 85748 Garching, Germany b Thermodynamics, Technical University of Berlin, Ernst-Reuter-Platz 1, 10587, Berlin, Germany

A B S T R A C T

A novel open-loop semi-passive control concept for oleo-pneumatic shock absorbers of CS-23 aircraft is presented.This concept enables the control of the damping characteristics in diverse impact scenarios with a singleconfiguration before touchdown. This approach maintains low energy consumption and allows for the applicationof slower actuators. The damping properties are optimized to achieve the best possible uniform decelerationduring compression in various impact scenarios. Integration of this concept is focused on a trailing armsuspension, where the controller takes the interaction between the wheel and the ground at the point of impact aswell as the orientation change of the shock absorber during deflection into account. This approach shows minimalmaximum load in systems with uniform deceleration curves. For uncontrolled systems, the guaranteed overshootcauses the restoring forces to amplify the tendency for a bounced landing, if the recoil is not effectively damped,especially when ground forces or lift are present. Therefore, the shock absorber is augmented with a conedmetering pin to provide increased damping at low deflections. To ensure a comparable analysis of the systemregarding rebound tendency, a decompression efficiency criterion is introduced, which can be determined viadrop tests. The influence of the metering pin and the single configuration control (separate and combined) onthe system's performance (minimal load and rebounce tendency) is examined under varying load conditions. It is shown that the semi-passive concepts improve overall performance across various load scenarios.
Keywords:Semi-passive shock absorberSingle action controlOleo-pneumatic dampingTrailing arm suspensionMetering pin Impact scenario adaptationRebound tendency reduction

INTRODUCTION

Much research and development was dedicated to landing gear suspension systems, with the dual objective of enhancing safety while reducing weight. In this context, oleo-pneumatic shock absorbers play a crucial role, as they are the most widely used solution for minimizingthe load on the aircraft structure [21,32], where the maximum force becomes minimal, cf. Fig. 1 b). These devices usually have a fixed dampingcharacteristic (passive), where the impact energy is absorbed by a gasspring and dissipated by viscous friction in a throttle. They are typicallydesigned as a single-acting variant, where an oil chamber is pressedagainst a chamber containing nitrogen. Upon impact, the force generates a pressure gradient between its two chambers, causing flow and compress the gas [7]. The generated force decelerates the system in vertical direction.

ISSN 2348-0386

For these passive devices, the deceleration during compression varies across different impact scenarios, defined as specific combinations of suspension mass, sink rate, and ground speed. This behavior is undesirablebecause the generated force may impair the occupant's comfort, injecthigh loads into the aircraft structure, and lead to bounced landings.Moreover, the system must be designed with substantial reinforcementto withstand the maximum load, increasing its weight. For example, ifthe damping is too soft for a particular impact scenario, cf. Fig. 1 c),the shock absorber will overshoot its steady-state position, resulting ina sizable restoring force that causes oscillation after touchdown. Theovershoot also amplifies the tendency to a bounced landing in the pres-

List of Symbols

Alphabetic Symbols

A_p	cross-section area of the piston
A_t	cross-section area of the throttle
C_c	ideal contraction coefficient
$C_{hyd,v}$	flow conductivity of the valve
e	error of the load estimation
F	suspension load force
F_d	damping force
F_s	force in the loaded steady-state
g	gravitational acceleration
j	electric current
m	mass
p	pressure in the lower chamber
p_0	pressure in the unloaded steady-state
p_s	pressure in the loaded steady-state
p_{atm}	atmospheric pressure
r_d	throttle radius
R_{hyd}	hydraulic resistance
t	time
V_0	gas volume in the unloaded state
v_g	ground speed
v_s	sink speed
W	impact energy
x	carriage displacement
x_d	shock absorber deflection
x_{ds}	shock absorber deflection in the loaded steady-state

Greek Symbols

γ	damper path length
ε	force ratio
η_c	compression efficiency
η_d	decompression efficiency
κ	adiabatic exponent of nitrogen
ξ	hydraulic resistance coefficient of the throttle
ϱ	oil density
σ	standard deviation

ence of ground forces or lift. Furthermore, the suspension components are subjected to significant stress caused by the restoring force, as therecoil energy is not entirely dissipated until the steady-state position isreached. Therefore, some devices have a coned metering pin that impedes the oil flow through the throttle at deep deflection. While otherprofiling options are available, the performance gains are marginal. Due to its simple design, the coned metering pin offers manufacturing advantages that reduce production costs. Nevertheless, the performancerestriction caused by the inability to adapt the damping characteristicto different landing scenarios is an inherent limitation of passive shockabsorbers [3,31,36].

If the damping is too hard, cf. Fig. 1 a), the landing gear suspension is rapidly slowed down due to large viscous forces, which prevents excessive overshoot. Hence, a bounced landing is less likely, as the maximumrestoring forces are much lower than in the soft damping case. However,the components are also subjected to a high load during compression,which can lead to component fatigue [10] and high load transmissioninto the aircraft structure. In summary, passive shock absorbers are inherently less efficient in their performance in varying touchdown scenarios, which is widely acknowledged. Consequently, several mechatronicsolutions, including semi-active and active systems, are being investigated.

Karnopp et al. [22] described a force generator capable of responding to standard feedback signals from the oscillating system. This force generator does not require the power supply of a servo mechanism.They also showed that it can achieve a performance similar to an active system. In addition, physical implementations of the concept arediscussed and compared with the system's behavior in the real world[22]. Based on earlier contributions, several papers have been publishedthat further investigate control algorithms of active/semi-active actuators. Ghiringhelli [15] evaluated a semi-active control for landing gearin general aviation aircraft, emphasizing its simplicity, reduced weight,and safety over fully active systems by modifying the oil orifice section. Ghiringhelli et al. [16] compared the behavior of a semi-activecontrol on a drop test model with that of a complete landing simulation. The control resulted in a significant reduction of the peak loadin both simulations. Their results differ when comparing the drop testsimulation with the landing simulation for the symmetric touchdown case. Holnicki-Szulc et al. [18,19] presented an overview of systemsadapting to the dynamic load caused by the landing impact, called Adaptive Impact Absorption (AIA). The actuators are controlled by sensorsand algorithms that predict and identify the landing impact. Dong et al. [8] presented a human-simulated intelligent control (HSIC) concept for a semi-active suspension based on a magnetorheological (MR) fluid, which considers different drop masses and sink velocities. Ahuré Powell et al. [1] investigated an adaptive suspension also based on a MRfluid for light helicopters that can continuously adjust the vertical liftload in response to different operating conditions. Ji-Young et al. [42]presented a control strategy for MR dampers in different landing scenarios. The maximum spring deflection was estimated based on sink rateand energy conservation, and the optimal total force for magnetic fieldcontrol was calculated. The results were compared with the landing behavior based on a Skyhook controller and a passive system. Pirooz etal. [33] presented a robust approach for active control of landing gearsuspensions that reduces vibration during taxiing and landing impact.A PID controller was used as the control algorithm and compared to thebehavior of a passive system. Electro-hydraulic systems capable of actively controlling the damping behavior were considered. Luong et al.[27] proposed a new method for controlling the shock absorber using aneural network, which can consider different touchdown scenarios andoperate autonomously without system-related knowledge. Luong et al.[28] presented a robust control for a MR shock absorber system in aircraft landing gears to improve the efficiency of absorbing impact energyin different touchdown scenarios with parametric uncertainties. Luonget al. [29] provided a supervised neural network-based controller for aMR shock absorber in the suspension of an aircraft, which adjusts thedamping force by varying the magnetic field. Arik et al. [2] investigated the behavior of an active pressure-controlled suspension systemwith a fuzzy controller to reduce impact vibrations. Bang-Hyun et al.[20] presented a MR landing gear suspension system with a damping force controlled by a magnetic field. Hui et al. [26] developed a nonlinear high-speed solenoid valve model and validated it with drop tests. Afuzzy PD controller was designed for semi-active control, effectively improving the control performance and reducing the impact load duringlanding. Mikulowski et al. [30] presented the limits for improvements inactive control and suggested some strategies, using a model of a passivelanding gear as a reference.

Despite this extensive research, there are several reasons why active systems are not commonly used on CS-23 aircraft [11]: Their complexdesign makes such systems more expensive and prone to failure, andtheir implementation is restricted by the limited dynamics of the actuators [12,23]. In addition, the safe interaction of actors, sensors, andcontrol algorithms must be proven, which increases effort and cost asthe mechatronization of the overall system rises. Instead, conservativesolutions with a minimum of well-proven sensors, actuators, and simplecontrol software are advantageous. Semi-passive systems, first intro-

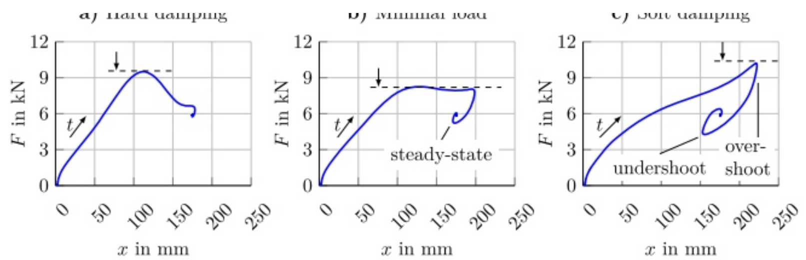

Fig. 1. Force response of the landing gear suspension as a function of the suspension deflection for (a) too hard damping configuration, (b) minimal load damping configuration, and (c) too soft damping configuration for a specific impact scenario.

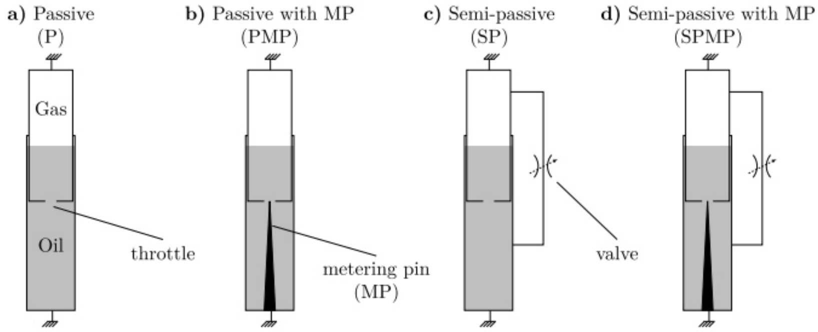

Fig. 2. Investigated passive oleo-pneumatic shock absorber with (a) and without metering pin (b). Investigated semi-passive oleo-pneumatic shock absorber with (c) and without metering pin (d).

duced by Rami et al. [12], offer a compromise and were little studied so far [17]. A semi-passive system performs an a priori single controlaction that optimally configures the degree of damping in response tomeasured or estimated external influences, ensuring low energy consumption before the actual touchdown occurs. During the event, theshock absorber behaves passively, eliminating the need for continuousclosed-loop feedback from sensor signals. This behavior minimizes therequired stability analysis, and the overall system is more robust due toits more straightforward design. Since there is time to adjust the desiredsettings, slower and more proven actuators can be used. In the event ofa power failure, the passive fallback mechanism persists, representing asignificant safety advantage [41].

This contribution presents a novel semi-passive concept that employs a proportional valve in a bypass parallel to a throttle, cf. Figs. 2 c) and d).The throttle provides a baseline hydraulic resistance, which essentiallyserves as a passive fallback mechanism in the event of power failure.In contrast to existing semi-active and active damping systems, this approach supplements the proven passive technology with an adaptablesolution, which minimizes energy consumption and enables adaptationto load conditions. The results show a comparable load distribution andrebound tendency, which distinguishes from methods previously investigated in the literature. The valve presets the flow resistance for diverseload conditions, thereby ensuring an almost uniform load distribution,evaluated via compression efficiency. This objective implies a minimalmaximum load, presented below, and has not yet been investigated inthe literature. This finding istechnology-independent and can be appliedto a variety of shock absorber types. Therefore, due to the inevitableovershoot, the shock absorber was augmented with a coned meteringpin that provides the required damping at deep deflection due to theincreased rebound tendency of such devices. This work studies the influence of the metering pin and single configuration control on systemperformance, both separately − see Figs. 2 a), b), and c) − and combined − cf. Fig. 2 d) − focusing on minimum load and the tendency torebound under various load conditions. In order to ensure comparability between different systems concerning rebound tendency, a criterion or decompression efficiency is introduced that can be determined by drop tests and that was derived in this work. This method has not beendocumented in the literature and is independent of any specific technology, allowing for a broad range of applications. Its derivation is akin tothe compression effect, ensuring consistency. Furthermore, this criterionobjectively assesses a damping system's tendency to rebound. Accordingly, a detailed simulation model was developed for the control systemdesign, which was validated with laboratory data from a drop test benchunder diverse load conditions, cf. Fig. 3. This technology was integratedinto a trailing arm suspension, which brings a few challenges: The sudden acceleration of the wheel from zero to ground speed upon impactcauses an additional force acting on the shock absorber, which affectsthe energy absorption efficiency and was taken into account in the control law. The wheel-ground interaction can be emulated on the drop testbench by accelerating the wheel to ground speed before the carriage isreleased. Furthermore, the orientation of the shock absorber changes depending on deflection due to the inherent geometry of the trailing armsuspension. Consequently, a uniform load on the landing gear suspension does not result in a uniform load on the shock absorber, and viceversa, which is a design conflict inherent in trailing arm suspensions.For instance, if the maximum load of the shock absorber is minimal, thesuspension's damping would be overly hard. Conversely, if the deceleration of the suspension is uniform, the damping at the shock absorberis overly soft. For diverse load scenarios, the maximum load is on aver age 2.3% $\approx$ 3.8%) higher than the possible minimal maximum load,cf. Fig. 1 b). Since this deviation is rather small, it is focussed here onthe design of the shock absorber, which seeks to provide a uniform load distribution.

2. Experiment and methods

The drop tests performed are based on the CS-23, which apply to aircraft with a maximum weight of 5, 670 kg [11], ensuring compliance with established standards for aircraft landing gear performance.In the experiment, the carriage was loaded with different drop masses

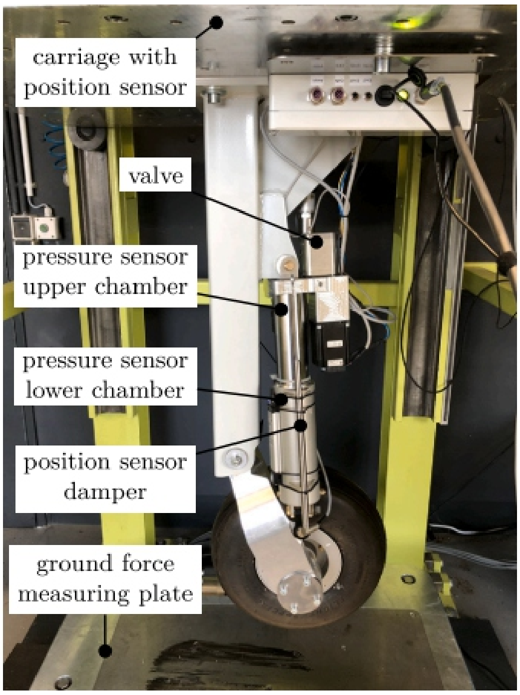

Fig. 3. Drop test bench of HEGGEMANN AG with a mechatronic shock absorber integrated into a trailing arm suspension.

(m = 300 kg, 400 kg, 500 kg), and the suspension with the shock absorber and tire was installed under the carriage, cf. Fig. 3. The bench was equipped with inductive displacement sensors on the carrier, shock absorber, and pressure sensors in both shock absorber chambers. The carriage was mechanically controlled by an electronic release system, determining the impact speed v_s with which the suspension falls onto the base plate. This was done for $v_s = 1.5\,\mathrm{m \cdot s^{-1}}$ and $2\,\mathrm{m \cdot s^{-1}}$. For some tests, the wheel was accelerated to ground speed $v_g = 28.2\,\mathrm{m \cdot s^{-1}}$ before impact. For every combination of m, v_s, and v_g, the valve was set to open, semi-open, or closed by setting the respective control current in Ampere. Moreover, specific outlier drop tests were performed, including scenarios for m = 500 kg load at larger impact speeds $v_s = 1.7\,\mathrm{m \cdot s^{-1}}$ and $2\,\mathrm{m \cdot s^{-1}}$. The shock absorber was charged with $0.42\,\mathrm{dm^3}$ of hydraulic oil (MIL-PRF-5606) and then pressurized with nitrogen until the internal pressure reached 14.5 bar at an ambient temperature of 10 ◦C. Each measurement contains seven time series data sets, i.e. pressure in theupper and lower damper chambers, ground force, shock absorber displacement, suspension deflection, initial wheel speed, and valve current,cf. Fig. 3. The model-based development of the system was describedin detail by Willich et al. [40], which allows for reliable statementsabout the functionality and possible adjustment ranges of the mechatronic shock absorber in actual use.

These experimental data were used for model parameter identification and validation, enabling virtual tests for optimization and controlinvestigations. The simulation model comprehensively covered the es sential physical aspects, such as the dynamic interaction between thecomponents, the hydraulic force modeling, and the shock absorber behavior under various load conditions. The validation process included isolating submodels, i.e. tire and shock absorber, and their composition based on laboratory data. The shock absorber submodel has beenvalidated in detail by Willich et al. [38,39]. For the validation of thedynamic behavior of the wheel, camera images that provided information about the deformation of the wheel tread were evaluated. Thesuspension model was automatically translated from CATIA [6] to TheMathworks - Simscape Multibody [37] to capture the rigid body dynam ics/interaction and mass distribution. Moreover, friction in the landinggear suspension has a significant influence on dynamics, which can exceed 10% of the hydraulic forces [23], and was therefore considered indetail. The modeling of the hydraulic forces is based on established principles of fluid dynamics, which ensures that the behavior of the shock absorber under different load conditions is simulated with sufficient accuracy without the need for excessive computing effort. In addition, the oil-gas interaction was modeled in detail according to Willich etal. [38,39]. Since the two fluids are not separated by a separator, whichis a standard design, the gas is absorbed by the oil during compression and desorbed during expansion, which leads to a hysteresis in thepressure-volume relation of the gas. In addition, the gas heats up dueto the firm compression, which influences the spring effect of the device. As a reference, the DA-42 aircraft, which has a maximum takeoffweight of 1, 420 kg [9], was used. Based on this, it was assumed that anaverage load of approximately 650 kg is applied to each main landinggear leg at impact. Furthermore, a ground speed of 25 m ·s−1 and a sinkspeed of 1.5 m ·s−1 were chosen, as these are typical values observed in landing scenarios.

3. Theory and calculation

3.1. A constant force implies minimal load and a guaranteed overshoot

In this section, we present a novel approach to show that maintaining a constant force during the compression phase implies minimizing maximum load, regardless of the shock absorber technology used. Furthermore, for systems where the maximum load is minimal, it is shownthat overshooting is guaranteed, which increases the tendency for abounced landing, if the recoil is not efficiently damped. The analysispresented here serves as a theoretical basis and motivation for introducing a decompression criterion and, consequently, for the design decisionto add a metering pin to mitigate the rebound tendency.Let w > 0 represent the impact energy that is either dissipated orstored. This energy is given by the integral

$$W = \int_{0}^{x_s} F_i(x, \dot{x}) dx \tag{1}$$

for any given shock absorber configuration denoted by $i \in \mathbb{N}$ within a specific impact scenario. The force $F_i(x, \dot{x})$ is strictly positive and the vertical displacement x is measured in positive direction. For a given impact scenario, the steady-state (x_s, F_s) with $F_s = F_i(x_s, 0)$ is the same for every shock absorber configuration, assuming that the spring property remains constant.

It is assumed that a shock absorber configuration $j \neq i$ exists, which is able to generate a constant force $F_{c\,j}$ during compression, cf. Fig. 4. Since the energy to be dissipated/stored in a certain impact scenario is the same for every shock absorber configuration, the following relation holds

$$\begin{aligned} W &= \int_{0}^{x_{\max j}} F_j(x, \dot{x}) \mathrm{d}x + \int_{x_{\max j}}^{x_s} F_j(x, \dot{x}) \mathrm{d}x \\ \Leftrightarrow W &= F_{c\,j} \cdot x_{\max j} + \int_{x_{\max j}}^{x_s} F_j(x, \dot{x}) \mathrm{d}x. \end{aligned} \tag{2}$$

Until maximum deflection is reached, no change of direction of the velocity and acceleration takes place so that x ≥ 0 and x ≥ 0. At maximum deflection, the velocity and acceleration are temporarily zero as thedeflection velocity changes sign. Here, the constant force is equal to the spring force $F_{c\,j} = F(x_{\max j}, 0)$.

Since the spring curve force F(x, 0) increases strictly monotonically, an overshoot beyond the steady-stateposition xs > 0 is guaranteed for the j -th shock absorber configuration,because

$$F_{c\,j} = F(x_{\max\,j}, 0) = m(g + \ddot{x}) > mg = F_s = F(x_s, 0) \tag{3}$$

during compression implies $x_{\max\,j} > x_s$.

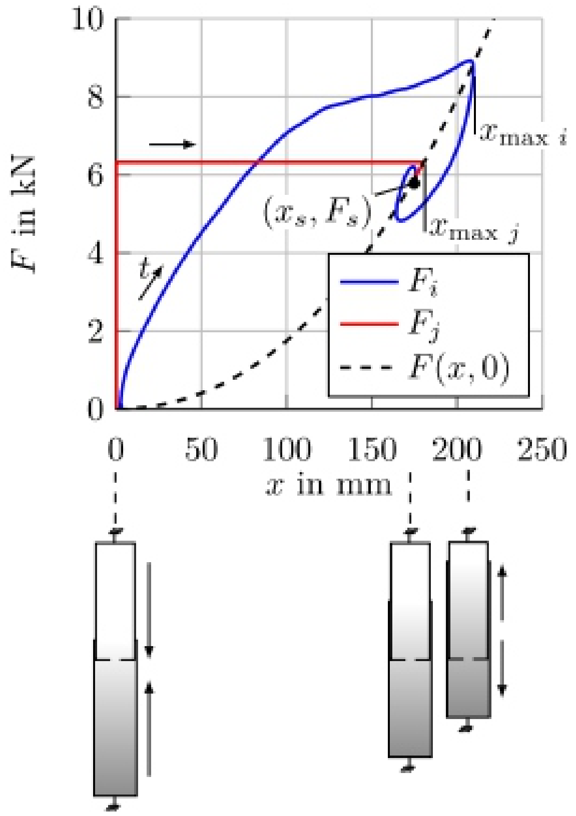

Fig. 4. Comparison of ideal energy absorption (red line) during touchdown with that of a non-ideal one (blue line). (For interpretation of the colors in the figure(s), the reader is referred to the web version of this article.)

The impact energy w is strictly positive, and therefore, the maximum norms can be applied to Eqs. (1) and (2) and equalized with each other

$$\left\| F_{c\,j} \cdot x_{\max\,j} + \int_{x_{\max\,j}}^{x_s} F_j(x, \dot{x}) \mathrm{d}x \right\|_\infty = \left\| \int_0^{x_s} F_i(x, \dot{x}) \mathrm{d}x \right\|_\infty . \tag{4}$$

For the left-hand side of Eq. (4), a lower bound is obtained, applying the reverse triangular inequality $\|p + q\| \geq |\|p\| - \|q\||$, as derived in the appendix

$$\left\| F_{c\,j} \cdot x_{\max j} + \int_{x_{\max j}} F_j(x,\dot{x})\mathrm{d}x \right\|_\infty \\ = \left| F_{c\,j} \cdot x_{\max j} - \left\| \int_{x_{\max j}}^{x_s} F_j(x,\dot{x})\mathrm{d}x \right\|_\infty \right| \tag{5}$$

with

$$p = F_{c\,j} \cdot x_{\max j} \qquad \text{and} \qquad q = \int_{x_{\max j}}^{x_s} F_j(x,\dot{x})\mathrm{d}x. \tag{6}$$

The constant force $F_{c\,j}$ is greater than any force during decompression, as the inertial force changes sign after the maximum deflection $x_{\max j}$. Therefore,

$$F_{c\,j} > \max_{x \in [x_s, x_{\max j}[} \left| F_j(x,\dot{x}) \right| \tag{7}$$

holds, related to the force occurring in the decompression phase in the half-open interval $\left[x_s, x_{\max j}\right[$.

For the integral on the right-hand side of Eq. (5), a lower bound applying the triangle inequality considering Eq. (7) is obtained

$$\left\| \int_{x_{\max j}}^{x_s} F_j(x,\dot{x})\mathrm{d}x \right\|_\infty \leq \int_{x_s}^{x_{\max j}} \left\| F_j(x,\dot{x}) \right\|_\infty \mathrm{d}x \\ = \left(x_{\max j} - x_s\right) \cdot \max_{x \in [x_s, x_{\max j}[} \left| F_j(x,\dot{x}) \right| < \left(x_{\max j} - x_s\right) \cdot F_{c\,j}. \tag{8}$$

Multiplying both sides of Eq. (8) with -1 and, subsequently adding the term $F_{c\,j} \cdot x_{\max j}$ on both sides, yields

$$
\begin{aligned}
&-\left\| \int_{x_{\max j}}^{x_s} F_j(x,\dot{x})\mathrm{d}x \right\|_\infty > -\left(x_{\max j} - x_s\right)\cdot F_{cj} \\
&\Leftrightarrow F_{cj}\cdot x_{\max j} - \left\| \int_{x_{\max j}}^{x_s} F_j(x,\dot{x})\mathrm{d}x \right\|_\infty > F_{cj}\cdot x_{\max j} - \left(x_{\max j} - x_s\right)\cdot F_{cj} \\
&= F_{cj}\cdot x_s.
\end{aligned} \tag{9}
$$

Since $F_{cj}\cdot x_s > 0$, the left-hand side of Eq. (9) is also strictly positive so that the absolute value can be applied to both sides

$$
\left| \left|F_{cj}\right| \cdot x_{\max j} - \left\| \int_{x_{\max j}}^{x_s} F_j(x,\dot{x})\mathrm{d}x \right\|_\infty \right| > \left|F_{cj}\cdot x_s\right| = F_{cj}\cdot x_s. \tag{10}
$$

The right-hand side of Eq. (10) is therefore a lower bound for the lefthand side of Eq. (4), taking Eq. (5) into account

$$
\begin{aligned}
&\left\| F_{cj}\cdot x_{\max j} + \int_{x_{\max j}}^{x_s} F_j(x,\dot{x})\mathrm{d}x \right\|_\infty \\
&\geq \left| F_{cj}\cdot x_{\max j} - \left\| \int_{x_{\max j}}^{x_s} F_j(x,\dot{x})\mathrm{d}x \right\|_\infty \right| > F_{cj}\cdot x_s.
\end{aligned} \tag{11}
$$

For the right-hand side of Eq. (4), an upper bound is obtained by applying the triangle inequality for integ

$$
\left\| \int_0^{x_s} F_i(x,\dot{x})\mathrm{d}x \right\|_\infty \leq \int_0^{x_s} \left\| F_i(x,\dot{x}) \right\|_\infty \mathrm{d}x = x_s \cdot \max_{x\in[0,x_s]} \left|F_i(x,\dot{x})\right|. \tag{12}
$$

Considering Eqs. (4), (11), and (12), the following inequality chain applies

$$F_{cj} \cdot x_s < \left\| F_{cj} \cdot x_{\max j} + \int_{x_{\max j}}^{x_s} F_j(x,\dot{x})\mathrm{d}x \right\|_\infty$$
$$= \left\| \int_0^{x_s} F_i(x,\dot{x})\mathrm{d}x \right\|_\infty \leq x_s \max_{x\in[0,x_s]} \left|F_i(x,\dot{x})\right| \qquad (13)$$
$$\Leftrightarrow F_{cj} < \max_{x\in[0,x_s]} \left|F_i(x,\dot{x})\right| .$$

Therefore, the constant force fcj, generated by the j-th shock absorber configuration during compression, is lower than any generated forcewith an arbitrary shock absorber configuration i with i ≠ j, and thusminimal, which had to be shown.

3.2. Force profile efficiency criteria

Efficiency criteria measure how shock absorbers manage energydissipation and dynamic responses under varying impact conditions,whereby n = 0 represents inefficiency and n = 1 denotes optimal perfor mance. To evaluate the objective of a uniform force profile, the commoncompression efficiency criterion [13,41] was used

$$\eta_c := \frac{1}{x_{\max i} \cdot \max_{x\in[0,x_{\max i}]} \left|F_i(x,\dot{x})\right|} \int_0^{x_{\max i}} F_i(x,\dot{x})\mathrm{d}x, \qquad (14)$$

which can be derived from the integral

$$W = \int_{t_1}^{t_2} F_i(x,\dot{x})\,|\dot{x}|\,\mathrm{d}t, \qquad (15)$$

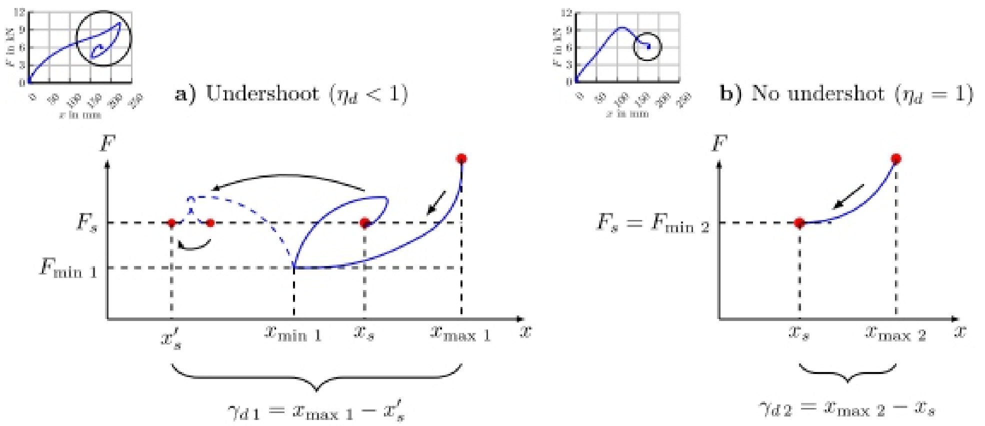

Fig. 5. Comparison of the decompression phases of a soft-damping configuration (a) with that of a hard-damping configuration (b).

which is evaluated for the compression phase between $t_1 = t(0)$ and $t_2 = t(x_{\max i})$. Since $\dot{x}$ is positive, Eq. (15) can be simplified to

$$W_c = \int_0^{x_{\max i}} F_i(x, \dot{x})\mathrm{d}x \tag{16}$$

by substituting $\mathrm{d}x = \dot{x} \cdot \mathrm{d}t$ and equalizing to its maximum norm, where the majorant is obtained through the application of the triangle inequality

$$\begin{aligned} W_c = \int_0^{x_{\max i}} F_i(x, \dot{x})\mathrm{d}x &= \left\| \int_0^{x_{\max i}} F_i(x, \dot{x})\mathrm{d}x \right\|_\infty \\ &\leq \int_0^{x_{\max i}} \left\| F_i(x, \dot{x}) \right\|_\infty \mathrm{d}x = x_{\max i} \cdot \max_{x \in [0, x_{\max i}]} \left| F_i(x, \dot{x}) \right| . \end{aligned} \tag{17}$$

Dividing the right-hand side of Eq. (17) yields Eq. (14). Consequently, the efficiency nc = 1 is the maximum value that can only be achievedby the -th shock absorber configuration, cf. Fig. 4 (red line), where theforce profile is uniform since the numerator and denominator in Eq. (14)cancel each other out. According to the results from Sect. 3.1, it followsthat the load is minimal for nc = 1.An important contribution of this work is the introduction of thedecompression efficiency, which provides a useful criterion for comparing the rebound tendency of shock absorber systems from drop tests.To preserve consistency concerning the compression criterion, the samederivation origin Eq. (15) was used, applying the minorant and the decompression integral limits $t_1 = t(x_{\max i})$ and $t_2 = t(x_s)$

$$\gamma_d \cdot \min_{x \in [x_s, x_{\max i}[} \left| F_i(x, \dot{x}) \right| \leq \int_{t(x_{\max i})}^{t(x_s)} F_i(x, \dot{x}) \, |\dot{x}| \, \mathrm{d}t \tag{18}$$

with

$$\gamma_d = \int_{t(x_{\max i})}^{t(x_s)} |\dot{x}| \, \mathrm{d}t, \tag{19}$$

instead. Eq. (18) can be rewritten as

$$\begin{aligned} & \gamma_d \cdot \min_{x \in [x_s, x_{\max i}[} \left| F_i(x, \dot{x}) \right| \leq \gamma_d \cdot F_\mu \\ \Leftrightarrow & \min_{x \in [x_s, x_{\max i}[} \left| F_i(x, \dot{x}) \right| \leq F_\mu \\ \Leftrightarrow & \frac{\min_{x \in [x_s, x_{\max i}[} \left| F_i(x, \dot{x}) \right|}{F_\mu} \leq 1 \end{aligned} \tag{20}$$

according to the mean value theorem for definite integrals [34], where fu is the mean force in the interval [xs, x max i[. The left-hand side of Eq. (20)would be a suitable candidate for the definition of the decompressionefficiency. However, we recommend choosing the steady-state force fsas the reference value

$$\eta_d := \frac{\min_{x \in [x_s, x_{\max i}[} \left| F_i(x, \dot{x}) \right|}{F_s}, \tag{21}$$

instead of fu, as this is advantageous and nd still becomes maximal if no undershoot occurs. The main advantage is that Eq. (21) can becalculated without knowing the deflection speed or position of the shockabsorber, while for fu, this must be measured. In addition, nd convergesexactly to unity if there is no undershoot, which is not the case if fu is used as a reference. This substitution is possible because

$$\min_{x \in [x_s, x_{\max i}[} \left| F_i(x, \dot{x}) \right| \leq F_s \leq F_\mu \tag{22}$$

holds in general. If the system is weakly damped, the force oscillates around the steady-state deflection (xs, fs), cf. Fig. 5 a), with the meanforce converging to the force in the steady-state position fs over moreextended periods such that fu ≈ fs applies. If the system is well dampedso that no undershoot occurs, cf. Fig. 5 b)

$$\min_{x \in [x_s, x_{\max i}[} |F_i(x, \dot{x})| = F_s < F_\mu \tag{23}$$

applies.

4. Concept design

This section introduces the novel semi-passive damping concept with metering pin (SPMP), cf. Fig. 2 d). Presetting the valve once before impact minimizes the maximum force acting on the system. However, sinceit was shown that the overshoot is guaranteed, which requires harderdamping at low deflection to reduce the rebounce tendency, we decidedto augment the shock absorber with a metering pin. This concept provides high compression and decompression efficiency over a large loadspectrum, if the landing conditions are predicted precisely to ensurethe correct valve presetting. However, in actual landings, variations inthe load distribution due to pitching, rolling, lift, or ground unevenness(e.g., in two- or three-point landing scenarios) cause uncertainties thatmust be accepted, as no further control actions occur. The aircraft sinkspeed, ground speed, and load significantly influence impact dynamicsduring touchdown, which can be analyzed with drop tests.

4.1. Load estimation

To estimate the load, a simple approach for a single main landing gear struct was suggested [29]

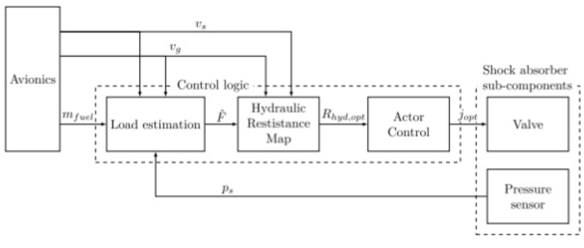

Fig. 6. Semi-passive single action control network of the SP and SPMP variants.

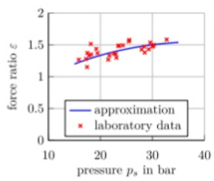

Fig. 7. Ratio between the stationary damping force and total weight force acting on the shock absorber as a function of stationary gas pressure.

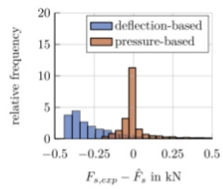

Fig. 8. Stationary load estimation error for the pressure-based and deflection-based approaches for a total of 3,000 different drop tests and a load bin width of 0.05 kN. The brown bars represent the intersection of blue and orange bars.

$$\hat{F} = \hat{F}_s - 0.5 \cdot \left(g \int_{t_t}^{t_l} \dot{m}_{fuel} \mathrm{d}t - \hat{F}_{lift}(v_s, v_g) \right), \quad (24)$$

where a two-point landing scenario was assumed with an evenly distributed load between the two main landing gear legs, which is considered by the factor of 0.5 in Eq. (24). For actual touchdowns, the effects of lift and fuel consumption on aircraft weight and the resulting reduction of load upon touchdown must be considered, cf. Eq. (24). According to Ghiringhelli [15], the work done by the lift forces is often uncertainand typically approximated by reducing the potential energy by a factor of 0.66. In drop tests, this can be considered by reducing the dropmass.The weight force f s before take-off can be determined from the stationary damping force per stru

$$\hat{F}_d = A_p \left(p_s - p_{atm}\right) \quad (25)$$

by evaluating the pressure ps from sensor data or from the measured shock absorber deflection xds before take-off. For trailing arm suspensions, the forces fs and fd are not equal, as the shock absorber changesits orientation, depending on the deflection and thus also the verticalcomponent of the damping force, which is corrected for the steady-statecase by multiplication with the force ratio �

$$\begin{aligned} & F_d \approx \varepsilon F_s \\ \Leftrightarrow & \hat{F}_s \approx \frac{A_p}{\varepsilon} \left(p_s - p_{atm}\right), \end{aligned} \quad (26)$$

cf. Fig. 7. If there is no pressure sensor, the signal from the position sensor $x_{d\,s}$ can be used by applying the adiabatic equation for p_s [14]

$$\hat{F}_s \approx \frac{A_p}{\varepsilon} \left(p_0 \left(\frac{V_0}{V_0 - A_p x_{d\,s}} \right)^{\kappa} - p_{atm} \right). \quad (27)$$

The standard deviation of the pressure-based load estimation error is $\sigma \approx 0.38\,\mathrm{kN}$ and the mean estimation error was $\bar{e} = \overline{F_{s,exp} - F_s} \approx -0.09\,\mathrm{kN}$, cf. Fig. 8. Although both estimation concepts can be used, the

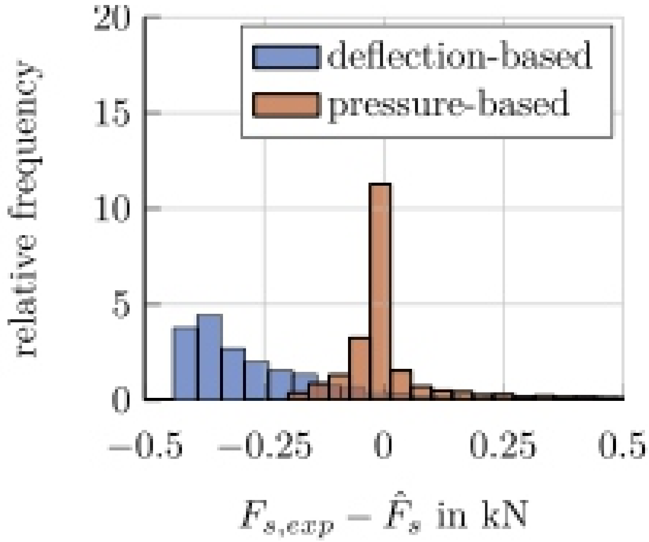

Fig. 8. Stationary load estimation error for the pressure-based and deflection-based approaches for a total of 3,000 different drop tests and a load bin width of 0.05 kN. The brown bars represent the intersection of blue and orange bars.

Table 1
Load estimation properties.

Parameter	Value
p_{atm}	1.013 bar
p_0	14.5 bar
A_p	1731 mm^2
V_0	0.27 dm^3
κ	1.4

deflection-based approach has a larger standard deviation of $\sigma \approx 0.44$ kN and mean error of $\bar{e} \approx -0.18$ kN. The pressure-based approach within the semi-passive variants with (SPMP) and without metering pin (SPMP) significantly reduces standard deviation and average estimation error, increasing its practicality and reliability in real applications. The properties of the load estimation approach are listed in Table 1.

4.2. Hydraulic resistance map

By systematically varying numerous combinations of these influences in drop test simulations, the hydraulic resistance was tuned by varying the opening degree of the valve to minimize the shock absorber'sload. Subsequently, the hydraulic resistance map was generated, whichdepends on the estimated load, sink speed, and ground speed as inputs,where the latter can be calculated from the data of radar altimetersand other navigation sources. The estimated load, measured sink speed,and ground speed feed into the hydraulic resistance map, cf. Fig. 6,which provides the optimal hydraulic resistance to achieve the minimum load on the shock absorber during compression. This map resultsfrom detailed evaluations during model development, validation, andoptimization, showing the specific dependencies of the optimum hydraulic resistance on these parameters. In particular, it shows a linearrelation between the optimum hydraulic resistance and the load as wellas the ground speed, cf. Figs. 9 a) and c). In Fig. 9 a), the SPMP variant

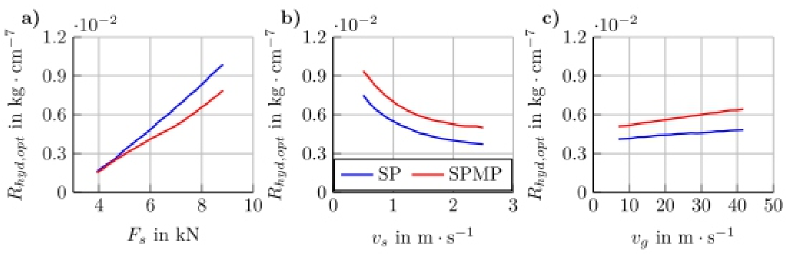

Fig. 9. Minimal load hydraulic resistance as a function of the drop load (a) for a sink speed $v_s = 1.5\,\mathrm{m \cdot s^{-1}}$ and ground speed $v_g = 25\,\mathrm{m \cdot s^{-1}}$, with v_s and v_g held constant. Minimal load hydraulic resistance as a function of the sink speed (b) for a ground speed $v_g = 25\,\mathrm{m \cdot s^{-1}}$ and drop load $F_s = 6.37\,\mathrm{kN}$, with F_s and v_g held constant. Minimal load hydraulic resistance as a function of the ground speed (c) for a sink speed $v_s = 1.5\,\mathrm{m \cdot s^{-1}}$ and drop load $F_s = 6.37\,\mathrm{kN}$, with F_s and v_s held constant.

has a lower gradient than the SP variant, as with the same drop mass, the metering pin dissipates a more significant amount of kinetic energyover the entire deflection due to the cross-sectional constriction at thethrottle. Hence, an overall lower initial hydraulic resistance is requiredto distribute the load as evenly as possible. In Fig. 9 b), the optimum hydraulic resistance decreases as the sink speed rises. The reason for thisis that the viscous forces are proportional to the square of the flow velocity of the oil. However, the higher the sink speed upon impact, the larger the viscous force that slows down the system. In order to minimize the load, the hydraulic resistance must, therefore, be lower at ahigh sink speed and rise as the sink speed decreases.

These findings reveal that future development of the hydraulic resistance map can also be determined with little effort carried out at the drop test bench, which reduces model development effort and cost.For the linear relationship between the optimal hydraulic resistance andload as well as ground speed, at least two data points are needed to adequately approximate a straight line, cf. Figs. 9 a) and c). An additionalpoint is necessary to accurately define the curvature of the non-linearrelationship with sink speed by a second-order polynomial, cf. Fig. 9 b). Consequently, at least $2 \cdot 2 \cdot 3 = 12$ supporting points to construct the hydraulic resistance map should be strategically determined on the droptest bench.

4.3. Open-loop control law

The pressure differential between the upper and lower chambers is proportional to the square of the resulting flow rate [4,35]

$$\begin{aligned} &\Delta p = R_{hyd} \dot{V} \left| \dot{V} \right| \\ &\Leftrightarrow \dot{V} = \operatorname{sgn}(\Delta p) \sqrt{\frac{|\Delta p|}{R_{hyd}}} \end{aligned} \tag{28}$$

for $|\dot{V}| > 0$, $R_{hyd} > 0$ and $\operatorname{sgn}(\Delta p) \neq 0$. The hydraulic resistance R_{hyd} describes the interaction between the flow rate and the pressure loss in the system. It corresponds directly to the system's physical parameters, such as damper geometry and fluid properties. The total volume flow rate is the sum of the valve and throttle volume flow rate, which finally leads to an expression for the total hydraulic resistance

$$\begin{aligned} &\dot{V} = \dot{V}_v + \dot{V}_t \\ &\Leftrightarrow \operatorname{sgn}(\Delta p) \sqrt{\frac{|\Delta p|}{R_{hyd}}} = \operatorname{sgn}(\Delta p) \sqrt{\frac{|\Delta p|}{R_{hyd,v}}} + \operatorname{sgn}(\Delta p) \sqrt{\frac{|\Delta p|}{R_{hyd,t}}} \\ &\Leftrightarrow \frac{1}{\sqrt{R_{hyd}}} = \frac{1}{\sqrt{R_{hyd,t}}} + \frac{1}{\sqrt{R_{hyd,v}}}. \end{aligned} \tag{29}$$

Rearranging Eq. (29) and including the throttle resistance term [25]

$$R_{hyd,t} = \xi \frac{\varrho}{2 C_c^2 A_t^2} \tag{30}$$

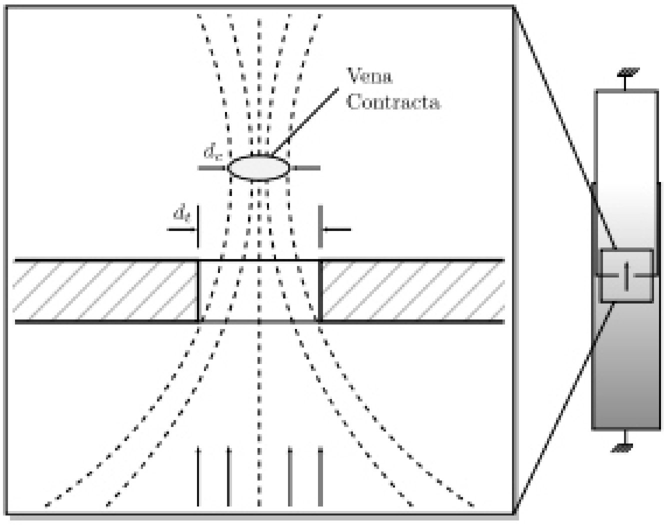

Fig. 10. Flow behavior at the throttle.

yields

$$\frac{1}{\sqrt{R_{hyd,v}}} = \frac{1}{\sqrt{R_{hyd}}} - C_c A_t \sqrt{\frac{2}{\xi \varrho}}, \tag{31}$$

which is sufficiently accurate for turbulent flows that appear for all landing scenarios in the transient state [4]. In Eq. (30), the effects of the Vena Contracta are accounted for by using the ideal contraction coefficient [24]. This phenomenon describes the narrowing of the fluidcross-section immediately after the throttle, cf. Fig. 10, where the flowvelocity is at its maximum.The equation for the valve flow rate, given by

$$\Delta p = R_{hyd,v} \dot{V}_v \left| \dot{V}_v \right|, \tag{32}$$

was utilized to represent pressure loss through the valve, considering $|\Delta p| > 0$. After rearrangement, Eq. (32) yields

$$C_{hyd,v}(j) := \mathrm{sgn}(\Delta p) \frac{\dot{V}_v}{\sqrt{|\Delta p|}} = \frac{1}{\sqrt{R_{hyd,v}(j)}}, \tag{33}$$

which describes the flow conductivity chydv as a function of electric valve current at constant pressure difference. The valve manufacturerusually publishes this characteristic curve. Eq. (33) was rearranged forthe actor current j and inserted into Eq. (31)

$$C_{hyd,v}(j) = \frac{1}{\sqrt{R_{hyd}}} - C_c A_t \sqrt{\frac{2}{\xi \varrho}}$$
$$\Leftrightarrow j_{opt} = C^{-1}_{hyd,v}\left(\frac{1}{\sqrt{R_{hyd,opt}}} - C_c A_t \sqrt{\frac{2}{\xi \varrho}}\right), \tag{34}$$

which is the actor control law, cf. Fig. 6. The properties of the control law approach are listed in Table 2.

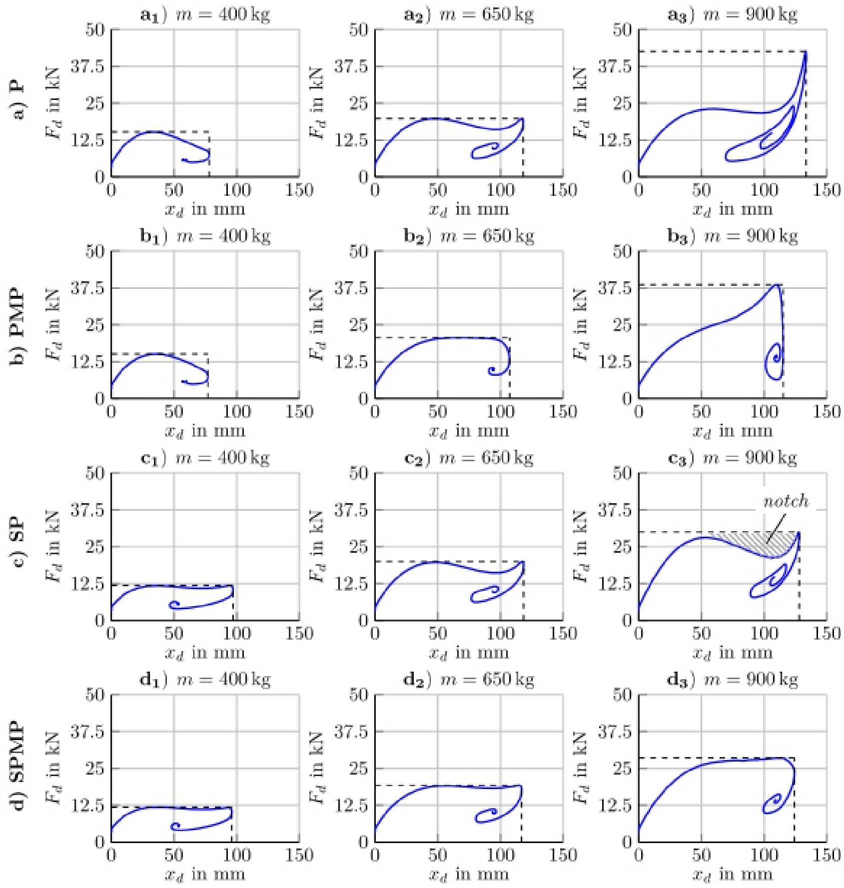

Fig. 11. Comparison of the shock absorber variants P, PMP, SP, and SPMP for a drop mass of $m = 400\,\mathrm{kg}$, $650\,\mathrm{kg}$, and $900\,\mathrm{kg}$ at a sink speed of $v_s = 1.5\,\mathrm{m \cdot s^{-1}}$ and a ground speed of $v_g = 25\,\mathrm{m \cdot s^{-1}}$.

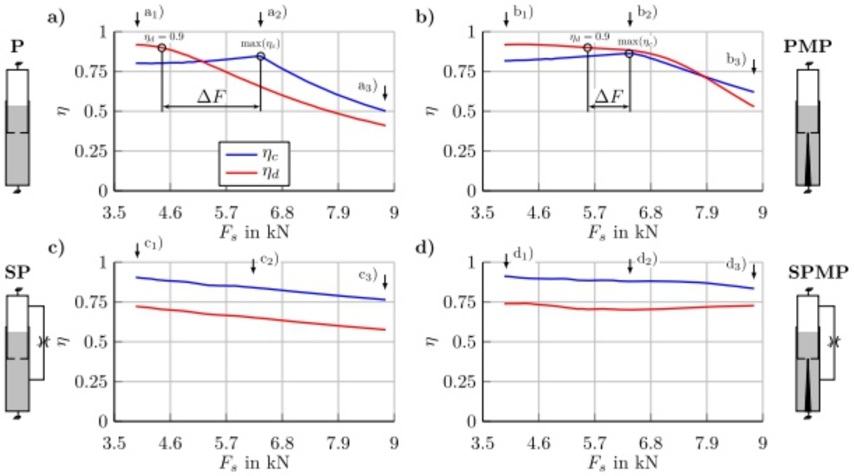

Fig. 12. Compression and decompression efficiencies as a function of the drop load for a sink speed of $v_s = 1.5\,\mathrm{m \cdot s^{-1}}$ and a ground speed of $v_g = 25\,\mathrm{m \cdot s^{-1}}$ for the shock absorber variants P, PMP, SP, and SPMP, whereby v_s and v_g are held constant.

Table 2
Control law properties.

Parameter	Value
ϱ	$867.6\,\mathrm{kg \cdot m^{-3}}$ [5]
A_t (SP, SPMP)	$3.14\,\mathrm{mm^2}$
C_c	0.611 [24]
ξ	0.015

5. Results

In Fig. 11, the shock absorber variants P, PMP, SP, and SPMP are compared for three load scenarios. For the load scenarios, the dropmasses were simulated at = 400 kg, 650 kg, and 900 kg, with thesame sink speed = 1.5 m · s−1) and ground speed = 25 m · s−1)in each case. For the passive variant P, the throttle radius was set to = 1.25 mm to obtain the lowest maximum load during compressionat a drop test mass of = 650 kg, cf. Fig. 11 a2). In order to archive thehighest compression efficiency for the PMP variant with a drop test massof = 650 kg, the throttle radius was set to = 1.3 mm, cf. Fig. 11 b2).For both semi-passive variants (SP, SPMP), the throttle radius was set = 1 mm to cover a wide range of operating load scenarios. A high loadwould require a large hydraulic resistance, cf. Fig. 9 a), which is ensuredby a small throttle flow area with a closed valve. The hydraulic resistance must be smaller at low load, which can be achieved by openingthe valve.

g is too hard for a drop mass of = 400 kg, which leads to a 3.2 kN higher maximum load compared to the semi-passive variants, compareFigs. 11 a1) and b1) with Figs. 11 c1) and d1). For a larger drop test massof = 900 kg, the damping of the passive variants is too soft, whichleads to high restoring forces, cf. Figs. 11 a3) to d3). Here, the SPMP variant achieves the lowest maximum load of 28.4 kN, followed by SP(29.7 kN), PMP (38.5 kN) and P (42.5 kN), which is a significant reduction of the maximum load for the semi-passive variants compared to thepassive ones. The application of a metering pin in the SPMP variant further improves the load distribution during deflection, as the notch in theSP variant is much less pronounced, cf. Fig. 11 c3).

In Fig. 12, the compression efficiency, cf. Eq. (14), and decompression efficiency, cf. Eq. (21), for all shock absorber variants are shown asa function of the drop load at a sink speed of = 1.5 m·s−1 and a groundspeed of = 25 m ·s−1. The efficiencies of the performed drop tests forFig. 11 are labeled in Fig. 12 via a1) to d3). A load deviation from thedesign optimum significantly reduces compression efficiency, with theP variant deteriorating more than the PMP variant under higher loads.However, this reduction is not as pronounced in the PMP version, as themetering pin contributes to the rather uniform force distribution. Moreover, the overshoot is comparatively weaker, cf. Figs. 11 a3) and b3).Consequently, the rebound under high load is less significant, and theoscillation around the steady-state position is more effectively dampened, which is reflected by the decompression efficiency, that is above = 0.9 for the PMP variant over a larger load spectrum comparedto the P variant, cf. Figs. 12 a) and b).

Compared to the passive variants, the semi-passive variants have ahigher and almost constant compression efficiency over the consideredload spectrum, cf. Fig. 12, which ensures minimal stress on the aircraftstructure. With the SP variant, the compression efficiency decreasesslightly as the load rises, which can be explained by the greater extentof the notch at higher loads. However, due to the guaranteed overshoot,the recoil of the semi-passive variants is on average more severe thanthat of the passive variants, cf. Figs. 11 a1) to d1). This caused by theexcessively hard damping in the lower load spectrum and reflected bya larger decompression efficiency. On the one hand, this makes a rebound less likely, as a large part of the impact energy dissipates in thecompression phase. On the other hand, this leads to an excessive loadon the aircraft structure, which should be avoided. At high loads, the decompression efficiency of the passive variants decreases significantly and falls below that of the semi-passive variants, cf. Fig. 12. Due to theincreased flow resistance induced by the metering pin at low deflection, the rebound is more effectively damped than with the SP variant,compare Fig. 11 c3) with Fig. 11 d3), which effectively suppresses oscillations around the steady-state position and reduces the undershoot inthe decompression phase, making a rebound less likely. Moreover, theformation of the notch, cf. Figs. 11 c3) and d3), is suppressed, whichimproves compression efficiency.

A more comprehensive drop test analysis was performed for the critical load spectrum, cf. Fig. 13, where drop mass and the ground speed are high, while the sink speed is low. Hence, the hydraulic resistancemust be significant to avoid excessive overshoot, cf. Fig. 9. The passive variants with moderate hydraulic resistance would deflect deeply into the gas spring, especially as the generated viscous forces are insufficient to slow down the system. However, if the hydraulic resistance isdesigned to perform competitively, the damping for the most landing scenarios would be too hard. Here, the semi-passive systems perform excellently by reducing the average maximum load to 9.84 kN (SP)and 9.39 kN (SPMP) compared to the passive variants 16.04 kN (P) and14.33 kN (PMP). Moreover, the compression and decompression efficiencies of the semi-passive variants are on average significantly higher thanthose of the passive variants, cf. Fig. 13. By adapting the hydraulic resistance to the load conditions, the standard deviation of the efficienciesfor the SP variant is significantly higher than for the passive variants. Itis only superseded by the SPMP variant.

6. Conclusion

This study investigated a single-action control concept for oleopneumatic shock absorbers of CS-23 aircraft, which ensures a minimal maximum load and reduces rebound tendency in different impact sce narios. The conducted tests revealed that the SPMP variant successfullyachieves a peak load reduction to only 28.4 kN compared to 42.5 kN forthe passive variant P, highlighting the advantages of semi-passive damping by combining a proportional valve and a coned metering pin. Thecompression efficiency of the semi-passive variants remains almost constant over a broad load spectrum, with the SP variant demonstratingan average efficiency of over $\approx 90\%$. In contrast, the passive variantsshow significant efficiency deterioration at high load. A metering pinleads to increased damping at low deflection. It reduces rebound oscillations, which is particularly advantageous for hard touchdowns, and theSPMP variant maintains a decompression efficiency of over 90% acrossa more extensive load range. Present tests showed that the semi-passivevariants (SP and SPMP) offer higher compression efficiency than thepassive variants in different load scenarios, especially in the high-loadspectrum. While the passive shock absorber variants significantly deteriorate in their efficiency at high load, the compression efficiency of thesemi-passive solutions remains almost constant over a wide load spec trum. The chosen approach thus minimizes the structural load on theaircraft by distributing the forces generated upon impact more evenly.Ultimately, this semi-passive system offers a promising solution to improve safety and comfort during aircraft landings while keeping systemweight and energy consumption low. Future work could focus on furtheroptimization of the control algorithms and testing under actual flight conditions.

7. Appendix

Reverse triangular inequality

Applying $a = p + q$ and $b = -q$ in the triangle inequality

$$\|a + b\| \leq \|a\| + \|b\|$$

for real numbers of a and b, one gets

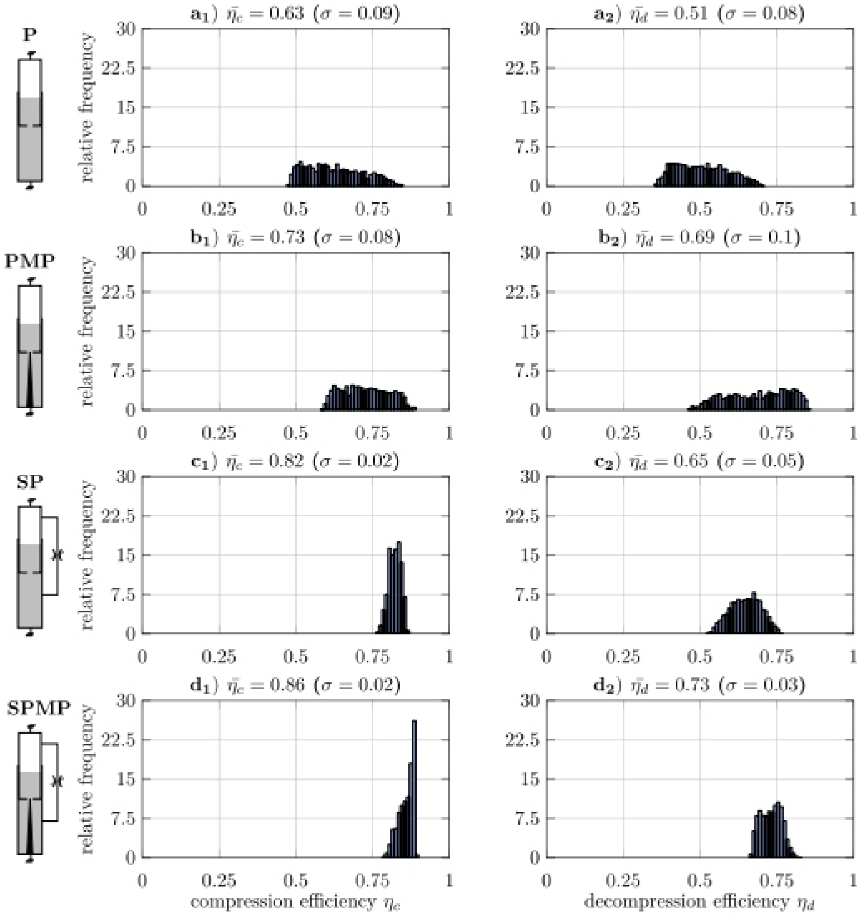

Fig. 13. Compression and decompression efficiencies (binwidth 0.01) as a histogram over a total of 2,067 critical load scenarios in a drop test mass range of $m = 650...900\,\mathrm{kg}$, sink speed range of $v_s = 1...1.5\,\mathrm{m \cdot s^{-1}}$ and ground speed range of $v_g = 25...30\,\mathrm{m \cdot s^{-1}}$.

$$\begin{aligned} &\|p + q - q\| \leq \|p + q\| + \|-q\| \\ \Leftrightarrow\ &\|p\| \leq \|p + q\| + \|q\| \\ \Leftrightarrow\ &\|p\| - \|q\| \leq \|p + q\| . \end{aligned} \tag{36}$$

On the other hand, if applying $a = p + q$ and $b = -p$ in Eq. (35), one gets

$$\begin{aligned} &\|p + q - p\| \leq \|p + q\| + \|-p\| \\ \Leftrightarrow\ &\|q\| \leq \|p + q\| + \|p\| \\ \Leftrightarrow\ &\|q\| - \|p\| \leq \|p + q\| . \end{aligned} \tag{37}$$

Eqs. (36) and (37) combined lead to the reverse triangle inequality

$$\|q + p\| \geq |\|q\| - \|p\|| . \tag{38}$$

CRediT authorship contribution statement

Felix Willich: Writing -- original draft, Visualization, Validation, Software, Resources, Methodology, Investigation, Formal analysis, curation, Conceptualization. Jadran Vrabec: Writing -- review & edit ing. **Florian Holzapfel:** Writing -- review & editing, Supervision, Projectadministration.

Declaration of competing interest

The authors declare that they have no financial interests.The authors declare that they have no conflict of interest. All authors read and approved the final manuscript. This research project is supported by the Federal Ministry for Economic Affairs and Climate Action (BMWK) on the basis of a decision bythe German Bundestag (grant number: ZF4630901LP8).Felix Willich received technical support from HEGGEMANN AG andSmart Mechatronics GmbH.

Data availability

Data will be made available on request.

References

[1] L.A. Ahuré Powell, Y.T. Choi, W. Hu, N.M. Wereley, Nonlinear modeling of adaptive magnetorheological landing gear dampers under impact conditions, Smart Mater. Struct. 25 (2016) 115011, https://doi.org/10.1088/0964-1726/25/11/115011.

[2] A.E. Arik, B. Bilgic, Fuzzy control of a landing gear system with oleo-pneumatic shock absorber to reduce aircraft vibrations by landing impacts, Aircr. Eng. Aerosp. Technol. 95 (2023) 284--291, https://doi.org/10.1108/AEAT-01-2022-0028.

[3] C.B. Asthana, R.B. Bhat, A novel design of landing gear oleo strut damper using MR fluid for aircraft and UAV's, Appl. Mech. Mater. 225 (2012) 275--280, https://doi.org/10.4028/www.scientific.net/AMM.225.275.

[4] L.K. Bohra, L.M. Mincks, S. Garimella, Experimental investigation of pressure drop characteristics of viscous fluid flow through small diameter orifices, J. Fluids Eng. 143 (2021), https://doi.org/10.1115/1.4048617.

[5] Chevron Products UK Limited, Data sheet MIL-PRF-5606: high performance general purpose hydraulic oil, https://cglapps.chevron.com/sdspds/PDSDetailPage.aspx?docDataId=481759&docFormat=PDF, 2016.

[6] Dassault Systèmes, CATIA: V5-6R2019, https://www.3ds.com/products-services/ catia/, 2019

[7] Y.W. Ding, X.H. Wei, H. Nie, Y.P. Li, Discharge coefficient calculation method of landing gear shock absorber and its influence on drop dynamics, J. Vibroeng. 20(2018) 2550--2562, https://doi.org/10.21595/jve.2018.19049.

[8] X.M. Dong, G.W. Xiong, Vibration attenuation of magnetorheological landing gearsystem with human simulated intelligent control, Math. Probl. Eng. 2013 (2013)1--13, https://doi.org/10.1155/2013/242476.

[9] Diamond Aircraft Industries GmbH, The Definition of Perfection, DA42-VI, https://www.diamondaircraft.com/fileadmin/diamondaircraft/documents/da42/DA42-VI_Product_Folder_2022_SCREEN.pdf, 2022. (Accessed 31 January 2025).

[10] G.R. Doyle, A review of computer simulations for aircraft-surface dynamics, J. Aircr.23 (1986) 257--265, https://doi.org/10.2514/3.45298.

[11] European Aviation Safety Agency, Certification specifications for normal, utility,aerobatic, and commuter category aeroplanes: CS-23, https://www.easa.europa.eu/sites/default/files/dfu/CS-23%20Amdt%203.pdf, 2012.

[12] R. Faraj, C. Graczykowski, J. Holnicki-Szulc, Adaptable pneumatic shock absorber,J. Vib. Control 25 (2019) 711--721, https://doi.org/10.1177/1077546318795532.

[13] R. Faraj, G. Mikułowski, R. Wiszowaty, Study on the state-dependent path-trackingfor smart pneumatic shock-absorber, Smart Mater. Struct. 29 (2020) 115008,https://doi.org/10.1088/1361-665X/ab9adc.

[14] S. Gan, X. Fang, X. Wei, Parametric analysis on landing gear strut friction of lightaircraft for touchdown performance, Appl. Sci. 11 (2021) 5445, https://doi.org/10.3390/app11125445.

[15] G.L. Ghiringhelli, Testing of semiactive landing gear control for a general aviationaircraft, J. Aircr. 37 (2000) 606--616, https://doi.org/10.2514/2.2672.

[16] G.L. Ghiringhelli, S. Gualdi, Evaluation of a landing gear semi-active control systemfor complete aircraft landing, Aerotecnica Missili E Spazio 83 (2004) 21--31, https://www.researchgate.net/publication/241252326_EVALUATION_OF_A_LANDING_GEAR_SEMIACTIVE_CONTROL_SYSTEM_FOR_COMPLETE_AIRCRAFT_LANDING.

[17] C. Graczykowski, R. Faraj, Adaptive impact mitigation based on predictive controlwith equivalent mass identification, Sensors 23 (2023), https://doi.org/10.3390/

[18] J. Holnicki-Szulc, C. Graczykowski, G. Mikułowski, A. Mróz, P. Pawłowski, Smart technologies for adaptive impact absorption, Solid State Phenom. 154 (2009)187--194, https://doi.org/10.4028/www.scientific.net/SSP.154.187.

[19] J. Holnicki-Szulc, C. Graczykowski, G. Mikulowski, A. Mróz, P. Pawlowski, R. Wiszowaty,

Adaptive impact absorption -- the concept and potential applications, Int. J. Prot. Struct. 6 (2015) 357--377, https://doi.org/10.1260/2041-4196.6.2.357.

[20] B.H. Jo, D.S. Jang, J.H. Hwang, Y.H. Choi, Experimental validation for the performance of MR damper aircraft landing gear, Aerospace 8 (2021) 272, https://doi.org/10.3390/aerospace8090272.

[21] B.H. Kang, J.H. Hwang, S.B. Choi, A new design model of an MR shock absorber for aircraft landing gear systems considering major and minor pressure losses: experimental validation, Appl. Sci. 11 (2021), https://doi.org/10.3390/app11177895.

[22] D. Karnopp, M.J. Crosby, R.A. Harwood, Vibration control using semi-active force generators, J. Eng. Ind. 96 (1974) 619--626, https://doi.org/10.1115/1.3438373.

[23] W. Krüger, Integrated Design Process for the Development of Semi-Active Landing Gears for Transport Aircraft, PhD thesis, University of Stuttgart, Stuttgart, 2000, https://elib.uni-stuttgart.de/bitstream/11682/3675/1/krueger.pdf.

[24] J.H. Lienhard, Velocity coefficients for free jets from sharp-edged orifices, J. Fluids Eng. 106 (1984) 13--17, https://doi.org/10.1115/1.3242391.

[25] D. Lin, F. Yang, R. Li, G. Di, Cavitation phenomenon in hydro-pneumatic interconnected suspension: modeling and parametric analysis, Nonlinear Dyn. 111 (2023) 8173--8189, https://doi.org/10.1007/s11071-023-08276-2.

[26] H. Liu, H. Gu, D. Chen, Application of high-speed solenoid valve to the semi-active control of landing gear, Chin. J. Aeronaut. 21 (2008) 232--240, https://doi.org/10.1016/S1000-9361(08)60030-8.

[27] Q.V. Luong, D.S. Jang, J.H. Hwang, Intelligent control based on a neural network for aircraft landing gear with a magnetorheological damper in different landing scenarios, Appl. Sci. 10 (2020) 5962, https://doi.org/10.3390/app10175962.

[28] Q.V. Luong, D.S. Jang, J.H. Hwang, Robust adaptive control for an aircraft landing gear equipped with a magnetorheological damper, Appl. Sci. 10 (2020) 1459,https://doi.org/10.3390/app10041459.

[29] Q.V. Luong, B.H. Jo, J.H. Hwang, D.S. Jang, A supervised neural network control for magnetorheological damper in an aircraft landing gear, Appl. Sci. 12 (2022) 400, https://doi.org/10.3390/app12010400.

[30] G. Mikułowski, Ł. Jankowski, Adaptive landing gear: optimum control strategy and potential for improvement, Shock Vib. 16 (2009) 175--194, https://doi.org/10. 1155/2009/732803.

[31] N. Paletta, A. Dmytriv, M. Belardo, D. Cristillo, M. Pecora, Landing gear concept and dynamic landing loads of the unmanned space re-entry vehicle USV3, Proc. Eng. 114 (2015) 38--45, https://doi.org/10.1016/j.proeng.2015.08.030.

[32] R. Pecora, A rational numerical method for simulation of drop-impact dynamics of oleo-

-pneumatic landing gear, Appl. Sci. 11 (2021), https://doi.org/10.3390/ app11094136.

[33] M. Pirooz, S.H. Mirmahdi, A.R. Khoogar, Robust force and displacement control of an active landing gear for vibration reduction at touchdown and during taxiing, SNAppl. Sci. 3 (2021), https://doi.org/10.1007/s42452-021-04320-1.

[34] P.K. Sahoo, T. Riedel, Mean Value Theorems and Functional Equations, World Scientific, 1998.

[35] L. Schickhofer, A universal nonlinear model for the dynamic behaviour of shockabsorbers, Nonlinear Dyn. 111 (2023) 1071--1093, https://doi.org/10.1007/s11071-022-07896-4.

[36] Y. Shimizu, S. Takagi, T. Sawada, Effect of tapered metering pin on magnetorheological fluid subjected to shock loading, Mater. Sci. Forum 856 (2016) 3--8, https://doi.org/10.4028/www.scientific.net/MSF.856.3.

[37] The MathWorks, Inc., Simscape Multibody: 9.13 R2022b, https://www.mathworks.com/products/simmechanics.html, 2021.

[38] F. Willich, B. Balaji, S. Knaup, F. Holzapfel, Modelling and validation of an oleopneumatic damper with mechatronic subsystems for CS-23 general aviation aircraft, in: IEEE Conference on Control Technology and Applications (CCTA), 2022,pp. 706--713.

[39] F. Willich, F. Holzapfel, J. Vrabec, Modeling dynamic pressure loss by absorptionin oleo-pneumatic shock absorbers without separator (preprint), https://doi.org/10.21203/rs.3.rs-4039079/v1, 2024.

[40] F. Willich, C. Wolff, A. Sutorma, U. Jahn, M. Stampa, Model-based systems engineering of an active, oleo-pneumatic damper for a CS-23 general aviation aircraftlanding gear: Dortmund, Germany, in: IEEE European Technology and EngineeringManagement Summit (E-TEMS), 2021, pp. 166--172

[41] D. Wu, H. Gu, H. Liu, GA-based model predictive control of semi-active landinggear, Chin. J. Aeronaut. 20 (2007) 47--54, https://doi.org/10.1016/S1000-9361(07)60006-5.

[42] J.Y. Yoon, B.H. Kang, J.H. Kim, S.B. Choi, New control logic based on mechanical energy conservation for aircraft landing gear system with magnetorheologicaldampers, Smart Mater. Struct. 29 (2020) 084003, https://doi.org/10.1088/1361-665X/ab9e11

ISSN 2348-0386

Aerodynamics and ice tolerance of the large passenger aircraft advanced rear end forward swept horizontal tailplane with leading edge extension

James H. Page a,*, Isik Ozcer b, Alessandro Zanon a, Michele De Gennaro a ,
Raul C. Llamas-Sandin c
a AIT Austrian Institute of Technology GmbH, Giefinggasse 4, 1210 Vienna, Austria
b ANSYS Inc, ANSYS Canada Ltd, 1000 Sherbrooke Street West Suite 2120, Monttreal, Q C H3A 3G4, Canada
c Airbus Operations SL, Paseo John Lennon, S/N 28906 Getafe, Madrid, Spain

A B S T R A C T

The advanced rear end (ARE) forward swept horizontal tailplane (FSHT) may allow a more compact empennage, reducing weight, drag, and, thus, fuel burn. Large passenger aircraft (LPA) empennages are typically sized up tosatisfy performance and handling requirements under critical icing conditions. One such requirement is sufficientlow speed (negative) lifting performance for the roundout manouevre following 45 min of flight in a holdingpattern in icing conditions. The FSHT geometry has the possibility to include a leading edge extension (LEX) inthe droplet shadow zone of the fuselage contraction where it could have some protection from icing, allowing tailsize reduction. This paper addresses the topics of three-dimensional inflight icing simulation and CFD analysis oficed tails in the industrial environment, inflight icing of the FSHT with LEX, and lifting performance andaerodynamics of the iced FSHT with LEX. Full aircraft air flow and droplet calculations were carried out using thefinite element method with solution error-based anisotropic mesh adaptation, on a single geometry, to calculateinlet and outlet condition profiles for an empennage-only icing simulation domain. Full aircraft-representative,three-dimensional, multishot icing simulations were then carried out to calculate 45 min ice accretion in aholding pattern in Appendix C glaze icing conditions, for eight different FSHT geometries. Following that, threedimensional CFD with the k-ω SST turbulence model was used to calculate the lifting performance and aerodynamics of each geometry, with and without ice, in a roundout flight condition from 0◦ to -15◦ angle of attack (AoA). The practice and feasibility of using three-dimensional multishot icing simulation in the LPA designenvironment are described. Analysis is then presented for three variations in FSHT forward sweep with a fixedgothic LEX, three variations in LEX chord with a 10◦ FSHT, and three variations in LEX span with a 10◦ FSHT. Iced lifting performance is found to correlate positively with forward sweep and exhibit a more nuanced relationship to LEX chord and span. In addition to the expected LEX vortex, a tip leading edge vortex is identified as key ice tolerant FSHT lifting flow mechanism. Detailed flow field analysis provides insight into the complexinterplay between the two flow mechanisms and the implications for iced lifting performance.

Keywords: Advanced rear endLarge passenger aircraftForward swept horizontal tailplaneIce toleranceInflight icing Empennage Passive ice protection Leading edge extension

INTRODUCTION

Aviation is energy intensive and the second greatest contributor of greenhouse gas (GHG) emissions in the EU transport sector, directemissions having contributed 3.8 % to 4.0 % of total EU GHG emissions in 2022 [1]. Aviation also contributes to climate change via high altitude emission of nitrogen oxides (Nox), sulphur dioxide (SO2), water vapour,and sulphate and soot particles [1], to local environmental degradationvia emissions of NOx and fine particles [2], and to harmful noise exposure in the vicinity of airports [3]. European air traffic is expected toreach pre-pandemic levels in 2025 and increase at an average of 2 % perannum to over 12 million flights in 2030 [4]. In the quests for competitive advantage and emissions reduction [5], the aerospace industry is continually researching novel and uncommon aircraft configurations and technology. Examples of such are: boundary layer ingestion[6], blended-wing-body [7], hydrogen propulsion [8], higher aspectratio wings [9], and the advanced rear end (ARE) forward swept horizontal tailplane (FSHT) featured in this paper.

Corcione et al. [10] summarized the well-known aerodynamic andstructural characteristics of forward swept wings in the context of theFSHT. This is recalled here. Contrary to rearward swept wings, forwardswept wing vertical deformation changes the local angle of attack (AoA)in the way that increases the aerodynamic load causing the deformation[10]. This can lead to static divergence and structural failure [10].Consequently, forward swept wings must be structurally capable ofwithstanding greater off-design vertical loads [10]. This confers extraweight [10]. However, the effect is less significant in low aspect ratiowings such as the FSHT [10]. In addition to this, the FSHT offers severalpotential advantages over the conventional rearward swept tail [10].The FSHT does not require a structural opening where the fuselage is significantly affected by structural loads [10]. This enables reductions inlocal reinforcements and therefore weight, and it reduces fuselagedeformation, leading to a more stable, efficient horizontal stabilizer[10]. Forward swept wings have a shock sweep about 5◦ greater thanthat of equally rearward swept wings and, therefore, require less sweepfor the same reduction in wave drag [10]. This results in less spanwiseflow and, thus, aerodynamic drag [10]. FSHT spanwise flow is from thetip to the root, which allows a greater stalling AoA than with the rearward swept equivalent [10]. Lastly, the increase in incidence of a FSHTunder an upward bending load results in a greater aerodynamic liftgradient, improving stabilizing performance [10]. The FSHT is thesubject of attention due to the consequential potential to reduce size andweight.

In new research, Corcione et al. [10] used a low fidelity aeroelastic method to evaluate the potential reductions in tailplane size offered bythe FSHT configuration. The aeroelastic efficiencies of reference FSHTand conventional horizontal stabilizer geometries were calculated toimply a potential 2 % reduction in tailplane surface offered by the FSHT[10]. This was translated to a 0.5 % fuel saving over a 3400 nm missionprofile[10]. Corcione et al. [11] used high-fidelity CFD to investigate thepotential reductions in size offered by the FSHT due to rigid aerodynamics alone. A three-dimensional Reynolds-averaged Navier-Stokes(RANS) based design of experiments optimization was carried out on the

FSHT [11] . Comparison of the resulting lift coefficient versus AoA (CL-α) curves with those of the conventional geometry suggested a %reduction in FSHT planform area [11]. Corcione et al. [12] used low- tomedium-fidelity aeroelastic calculation-based and high-fidelityCFD-based design of experiments to calculate two response surfaces,which were, in turn, used in a multidisciplinary optimization (MDO)process on the FSHT. The results indicated that a 9 % reduction intailplane area and 16 % reduction in tailplane mass could be achieved,for the same handling and stability performance as the conventional tail,if it included a leading edge extension (LEX) [12]. It could also deliverbetter aeroelastic performance [12]. The FSHT with LEX is based on twoAirbus patents [13] and [14]. Fig. 1 shows the geometry with a 10◦forward swept leading edge beside the conventional tail geometry for context.

A present trend in LPA empennage design is towards passive ice protection (private communication). This is in line with the guidance inAdvisory Circular (AC) 25–25A, which advises that the tailplane may bedesigned for full operation in icing conditions without active ice protection [15]. Inflight icing can occur under a wide range of commonatmospheric and cloud conditions, and cause a wide range of adverseeffects on lift, drag, speed, stability, and controllability, presenting asignificant threat to safety, as reported in [16]. The Code of RegulationsTitle 14, Appendix C to Part 25 states that the "most critical ice accretionin terms of airplane performance and handling qualities for each flightphase must be used to show compliance with the applicable airplane

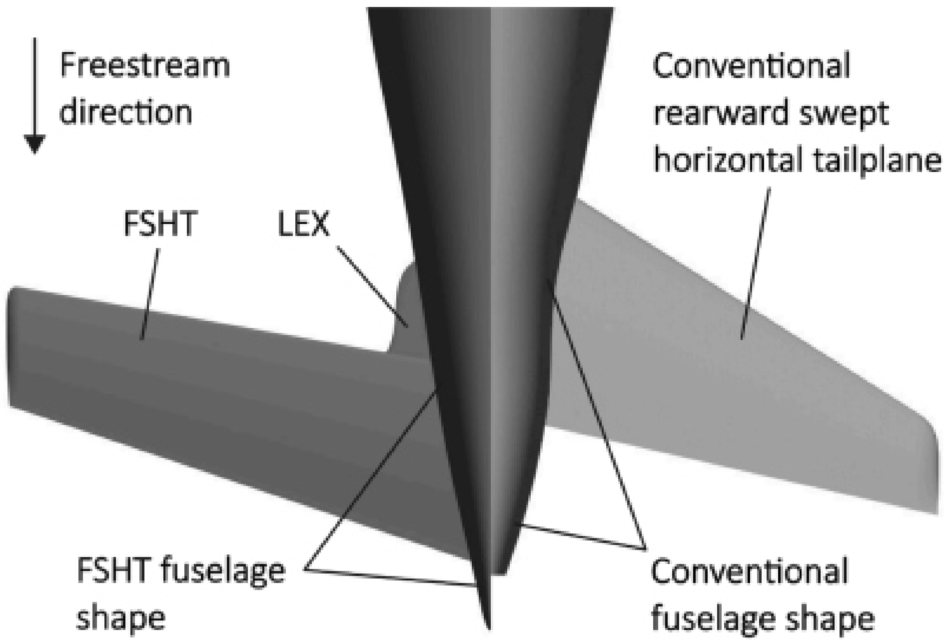

Fig. 1. FSHT with LEX geometry with a 10° forward swept leading edge (left) and the conventional reference geometry (right).

performance and handling requirements in icing conditions” [17]. It also specifies the ice accretion flight phases and states that the full rangeof specified atmospheric icing conditions must be considered [17].One of the initial motivations for this work was the location of theLEX inside a droplet shadow zone, where the liquid water content (LWC)of the air is locally very low, even in heavy cloud or rain, in the lee of therear end contraction of the fuselage. This offers the LEX some passive iceprotection and thus the chance to mitigate some of the adverse effects oficing on lift. Sufficient ice tolerance is typically achieved in conventionalLPA empennages by increasing the size of a well optimized clean(uniced) design (private communication). It is hypothesized that theFSHT with LEX configuration could offer improved ice tolerance withless reliance on size increase. Fig. 2 shows the FSHT with LEX with thedroplet trajectory and shadow zone effect annotated.

In this paper, three-dimensional inflight icing simulation, along with CFD, was used to explore the iced aerodynamics and potentially icetolerant flow mechanisms of this configuration. The full range of flightphases and icing conditions was considered impractical, therefore apotential worst-case scenario was defined whereby the horizontal stabilizer is required to generate sufficient downward lift to complete theroundout manoeuvre after 45 min holding at 16,000 ft in Appendix Ccloud [17,19].

There is a reasonable volume of literature available on iced aerofoilaerodynamics. For an early example, Kwon and Sankar [20] carried outa three-dimensional, compressible, Navier-Stokes calculation of a 30◦swept NACA 0012 wing with a two-dimensional extruded glaze iceshape. The results showed the formation of full span leading edge

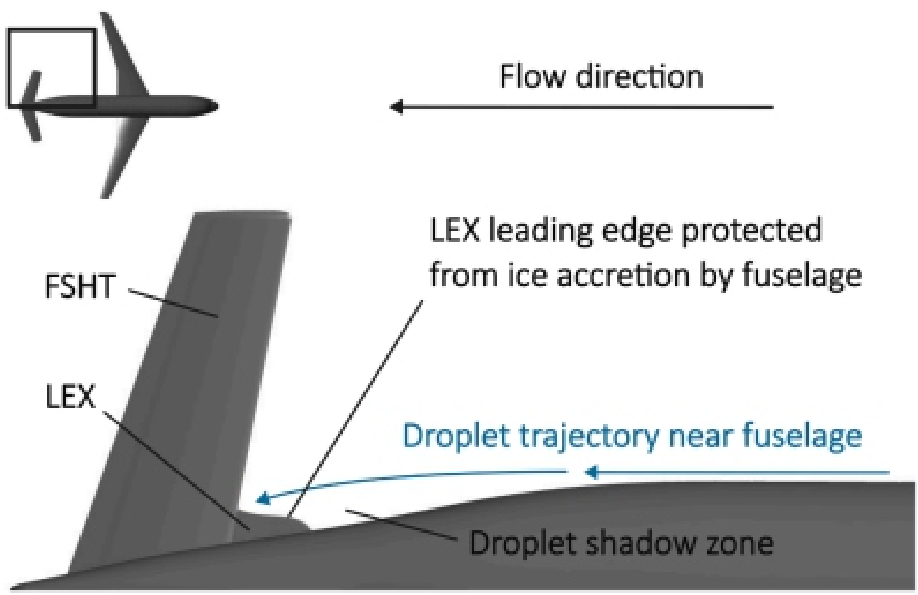

Fig. 2. FSHT combined with a LEX located in a droplet shadow zone. This figure has been adapted from [18] with permission, © 2023 SAE International.

vortices covering part of the chord at 4◦ AoA and part-to-full chord at 8◦ AoA [20]. A review by Bragg et al. [21] summarized research from 1978to 2005 on iced aerofoil aerodynamics for four main classes of aerofoilice: roughness, streamwise, horn (typical of glaze icing), andspanwise-ridge. In addition to aerodynamic penalties, the work discussed the identification of leading edge vortices as the main feature ofrearward swept wings with horn ice, and the importance of horn height,location, and angle [21]. In more recent research, Bragg et al. [22]considered aerodynamics and geometry to propose the swept wing iceshape classes: roughness, streamwise, three-dimensional leading edgehorn, highly three-dimensional leading edge horn, and spanwise ridge.The term type I flowfield was used to refer to that with one or morespanwise running leading edge vortices resulting from ice-inducedseparation, and type II flowfield to refer to that without leading edgevortices and, instead, many streamwise (oil) streaks [22]. The streakswere suggested to be counter-rotating vortices coming from highlythree-dimensional ice shape features [22]. Broeren et al. [23] carried outan experimental study of glaze-iced swept wing aerodynamics usingscale models of the 37◦ rearward swept CRM65 wing with Reynoldsnumber 1.8 × 106 at Mach 0.18 and Reynolds number 11.9 × 106 atMach 0.23. Several representations of an experimental swept wing glazeice shape were used to compare effects of ice shape fidelity and roughness on lift and drag coefficients, stall, and flow dynamics [23]. Differences in maximum lift coefficient (CL,max) reduction were observedbetween the ice shape fidelity levels [23]. With the reduced fidelity iceshapes, type I flows developed with increasing AoA [23]. However, withthe high fidelity shape, combinations of type I and II were observed at4.3◦ and 5.3◦ AoA, before type I became more dominant at 6.4◦ and 7.4◦AoA [23].

This paper focusses on two themes: the first is high-fidelity threedimensional inflight icing simulation and CFD of iced tails in the industrial environment; the second is the aerodynamics of iced FSHTs with a view to ice tolerance. The objectives of the paper are;

1. To propose an approach to the effective use of high-fidelity threedimensional inflight icing simulation and CFD for ice tolerant design and sizing of LPA empennages.
2. To identify and provide detailed insight into the aerodynamics of iced FSHTs with LEXs.
3. To identify and provide detailed insight into the aerodynamic effects of some of the main design parameters of an FSHT with LEX, under icing conditions.

The topic of three-dimensional inflight icing simulation methodology has been well covered in scientific literature. The reader is directed to references [24–28] for descriptions of droplet trajectory calculation,ice accretion calculation, multishot icing simulation, and multishot icingsimulation with automatic remeshing. Several publications providedparticularly useful guidance for the development of the workflow and choice of specific methods in this paper. Pueyo et al. [19] argued that inthree-dimensions, Eulerian droplet trajectory calculations are simplerand more efficient than Lagrangian calculations, and developed a suggested best practice for droplet trajectory calculations withthree-dimensional geometries [19]. An anisotropic mesh adaptationprocess based on an error metric derived from the Hessian matrices ofthe air and droplet flow fields was presented, and an LPA geometry wasused to show the resulting good resolution of droplet shadow zones andimpingement limits [19]. In a study, particularly relevant to RANSinvestigation of iced swept-wing performance degradation, Ozcer et al.[29] compared the Ansys Fluent-calculated and experimental CL-αcurves for the 37◦ swept CRM65 wing. The experimental curves camefrom research in which thirty min of ice accretion was carried out inglaze icing conditions in the NASA Glenn Research Center IcingResearch Tunnel [30]. The ice shape with prominent lobster tail featureswas scanned, 3D printed and installed on a wing leading edge for AoAsweeps in the Wichita State University wind tunnel [31–34]. Fig. 3

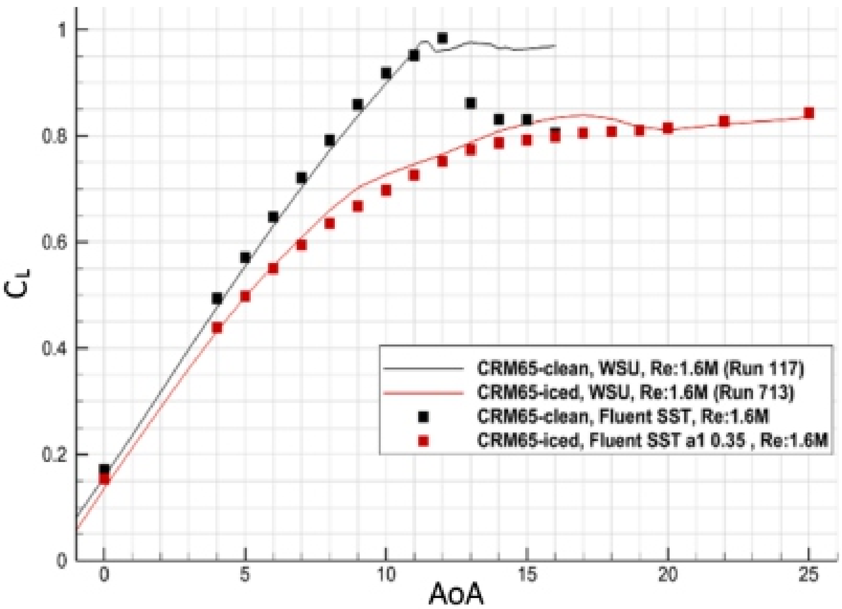

Fig. 3. Comparison between Fluent-calculated and experimental C_L-α curves for the clean and iced CRM65 37° swept wing at a Reynolds number of 1 million and Mach 0.18. This figure has been reprinted with permission from [29], © 2023 SAE International.

shows the CL-α curves for the clean and iced 37◦ swept CRM65 wing at a Reynolds number of 1 million and Mach 0.18 [29]. The numericalmethodology used in the study showed good agreement with up to and including CL,max for the clean wing and throughout the AoArange for the iced wing [29]. The numerical methodology in [29] wasalmost identical to that used for the aerodynamic calculations carriedout for this paper, with which it shares a coauthor. This provides thebasis for reasonable confidence in the results presented in this paper. The topics of inflight icing on the FSHT, lifting performance degradation of the iced FSHT with LEX, and aerodynamics of iced FSHTs, tothe best knowledge of the authors, have yet to appear in scientificliterature. Accordingly, it is in these areas that this paper attempts tooffer novel contributions.

In Section 2, the methodology used for calculating the effects of icing on LPA empennage lifting performance is described. This serves as arecommended practice for the purpose. In Section 3, results for twoseparate studies are presented. The first is the effects of sweep on icedFSHT low speed lifting performance. The second is the effects of LEXspan and chord on iced FSHT low speed lifting performance. Detaileddescriptions of the effects on local lifting performance with accompanying flow field analysis are provided. In Sections 4 and 5 respectively,discussion of the findings and conclusions regarding the implications forthe design are provided.

2. Methodology

Ice accretion on the FSHT with LEX and its iced aerodynamics are complex three-dimensional phenomena, and, therefore, require threedimensional calculation to be adequately considered in computationalresearch studies or design processes. The methodology outlined in thissection is intended to serve as recommended best practices for highfidelity ice accretion and iced geometry aerodynamics calculation inLPA empennage research and design, at a scale and computationalexpense suitable for industry. The methodology used for ice accretionand aerodynamic calculation is the same as that described in the lessextensive reference by the authors, [18], and is described here in full forcompleteness.

2.1. Ice accretion calculations

Ice accretion was calculated on the FSHT by using Ansys FENSAP-ICEto carry out three-dimensional multishot icing simulations [24–28]. Asimulation comprises four calculation steps: 1) steady turbulent flow field calculation, including consideration of surface roughness and calculation of the substrate heat flux, 2) steady Eulerian droplet fieldand substrate impingement calculation [24], 3) unsteady Eulerian substrate water film runback, heat transfer, evaporation, ice accretion andupdated geometry calculation [26], and 4) remeshing [28]. These foursteps calculate the icing over a specified time, typically one to a fewminutes, called a ‘shot’. Multiple shots performed sequentially make upa multishot icing simulation. More detail can be found in references[26–28].

To minimize computational expense, icing simulations were carried out in a half tail-only domain without the vertical stabilizer. Velocitycomponent, temperature and turbulent viscosity inlet conditions, a static pressure outlet condition, and a nose-to-tail vertical symmetryplane were used for the CFD calculations LWC, droplet size distribution,and droplet velocity component inlet conditions were used for thedroplet calculations. The domain is shown in Fig. 4. At 4◦ AoA, trajectory of the main wing wake and wing root vortex, and the taperingof the fuselage at the tail exert considerable influence over the flow anddroplet conditions in the vicinity of the substrate, as demonstrated bythe turbulent viscosity isosurfaces in Fig. 5. This necessitates consideration of full aircraft effects. To achieve this, flow field and droplet calculations were carried out with the full aircraft, including fuselage, mainwing, and horizontal stabilizer, with a symmetry plane, to allow theextraction of full aircraft-based boundary condition profiles for the tailonly geometry.

The full aircraft unstructured mesh was created using Fluent Meshing. Prism elements were used for full boundary layer resolution, with asurface y+ mostly less than or equal to one, and tetrahedra for the volume. Specialized refinement was required for accurate capturing of theLWC shadow zone where the LEX is located. Fluent Meshing generatesisotropic surface and volume elements, which would be prohibitivelyexpensive under enough refinement to sufficiently resolve the wingbody juncture wake from the inlet boundary to the FSHT leadingedge, of key importance to accurate droplet impingement calculation.Therefore, the mesh was optimized using Ansys Optigrid to carry outsolution error-based anisotropic mesh adaptation, based on the dropletand velocity fields, including static pressure, velocity and LWC. Figs. 6and 7 show the adapted mesh, with reflection of the mesh in the symmetry plane for ease of conceptualization. The influence on the LWCseen by the horizontal stabilizer is shown on a plane just upstream of theempennage in Fig. 8. Before adaptation, the shadow zone was highly

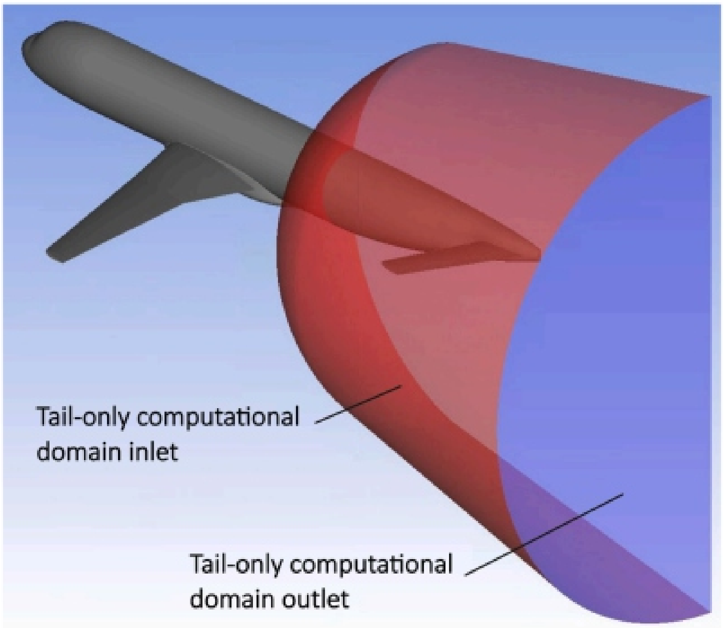

Fig. 4. The tail-only domain used for multishot icing simulations of the horizontal stabilizer, with the inlet and outlet boundaries annotated. This figure has been adapted with permission from [18], © 2023 SAE International.

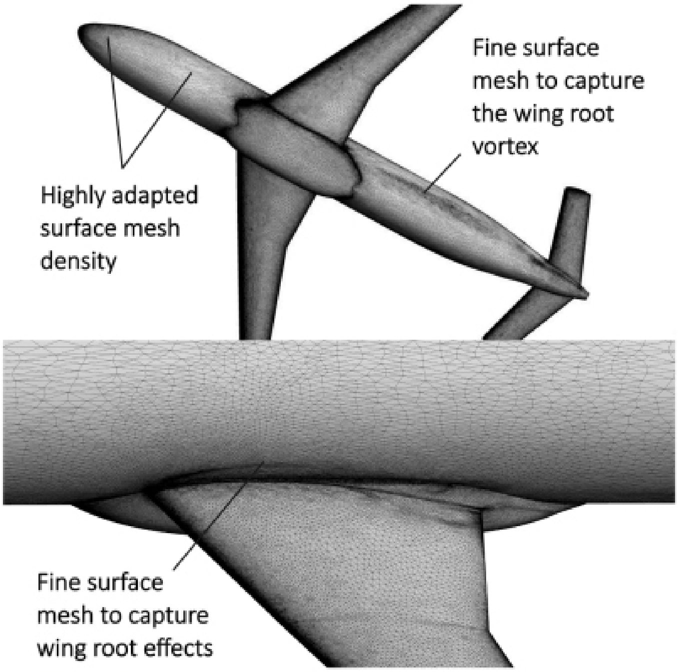

Fig. 6. The results of anisotropic adaption of the aircraft surface mesh based on the air and droplet flow solutions. This figure has been adapted with permission from [18], © 2023 SAE International.

diffused. Following adaptation, the shadow zone was significantly better resolved. Another important feature revealed by the mesh adaptation isa LWC enrichment zone. With a trajectory passing just below the horizontal stabilizer, this would be of relevance to tail vertical positioningand would be very challenging to consider in icing wind tunnel testing,considering the scale of the aircraft, or without the mesh adaptationrecommended here. Ansys FENSAP was used to carry out finite elementmethod CFD calculations for the full aircraft due to the stretched natureof the adapted mesh.

In the tail-only icing simulations performed for this paper, steadyRANS calculations were carried out using the finite element method, andthe original Spalart-Allmaras (SA) turbulence model with the sand-grainroughness extension [35] set to uniform 0.5 mm roughness on icedsurfaces. The flight condition for the calculations was that of a twin jetengine airliner flying in a holding pattern at 16,000′, 220 kts calibratedair speed (145 m/s true air speed), -12 ◦C static temperature, with flapsand slats retracted, at 4◦ AoA. The cloud conditions for the dropletcalculations were 0.38 g/m3 LWC and a seven bin Langmuir-D dropletsize distribution with a 20 μm mean volumetric diameter (MVD). Theseconditions were selected from reference [19]. Table 1 shows a summaryof the flight, icing and solver settings

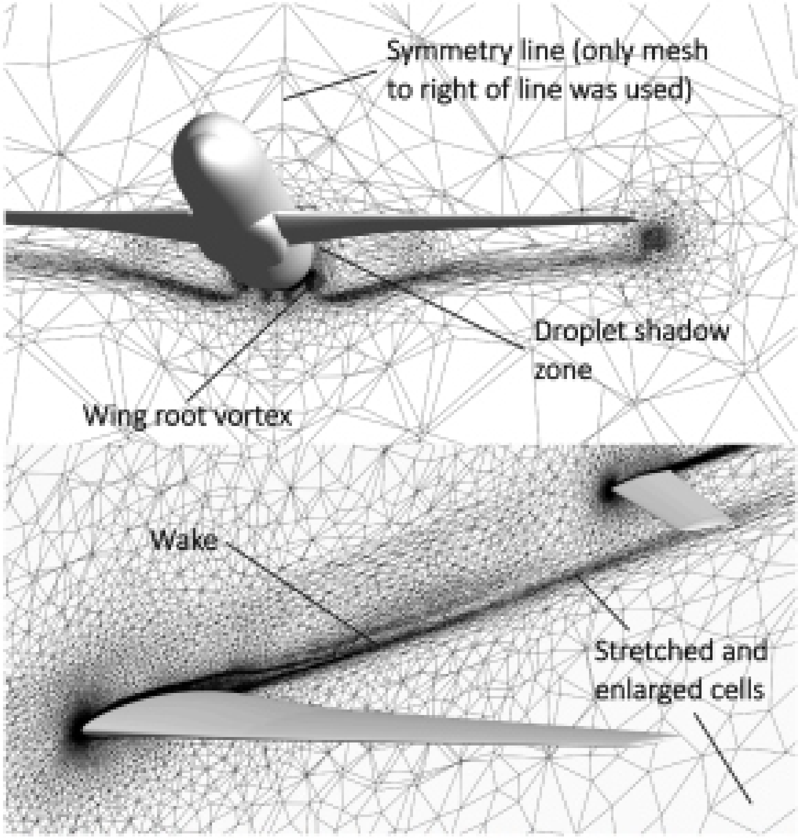

Fig. 7. The results of anisotropic adaption of the volume mesh based on the air and droplet flow solutions. This figure has been adapted with permission from [18], © 2023 SAE International.

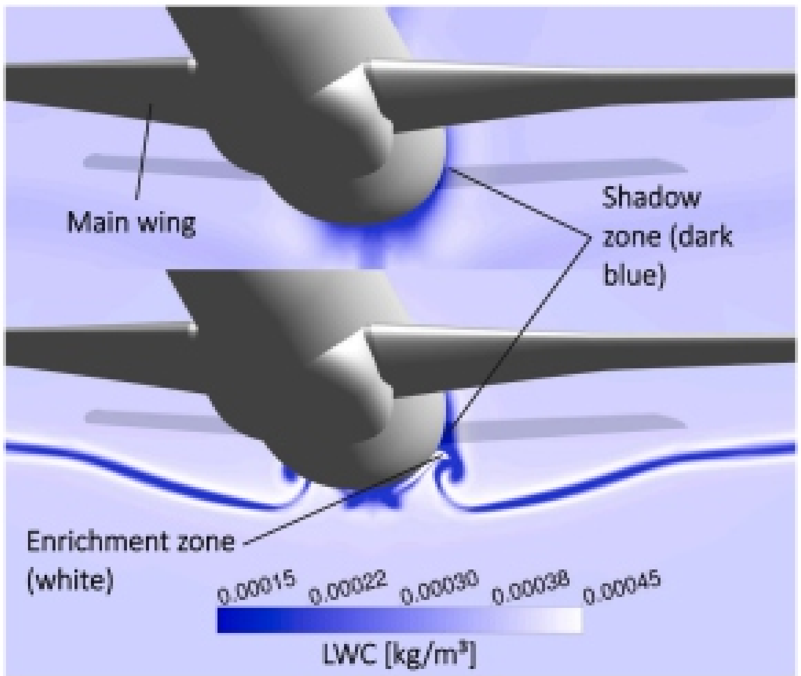

Fig. 8. LWC distribution before (top) and after (bottom) mesh adaptation with annotated shadow and enrichment zones. This figure has been adapted with permission from [18], © 2023 SAE International.

The icing simulations were divided into 20 shots of 2¼ min each to give a total of 45 min ice accretion time. Ansys Fluent Meshing was usedto remesh the new ice shape in the tail-only domain resulting from eachshot. The use of the shrink wrap procedure necessitated remeshing of theentire domain. To avoid progressive diffusion of the boundary conditions, they were re-interpolated from the full aircraft solution. Bodies ofinfluence were used to mimic the cell size distribution of the adaptedmesh.

The workflow for horizontal stabilizer ice accretion calculation can be summarized as follows: 1) fully scripted full aircraft computer aideddesign (CAD) model to mesh, 2) automatic solution error-based anisotropic full aircraft mesh adaptation for pressure, velocity component,

Table 1
Flight, icing and solver settings for icing simulations.

Turbulence model	SA with sand-grain roughness extension
Roughness on iced surfaces	Uniform 0.5 mm sand grain roughness
VCAS	220 kts
Altitude	16,000 ft
Static temperature	-12 °C
AoA	4°
LWC	0.38 g/m^3
Droplet MVD	20 μm
Droplet particle size distribution	7 bin Langmuir-D distribution
Total icing time	45 min
Individual shot icing time	2¼ min

and LWC gradients in a FENSAP-DROP3D-Optigrid loop, 3) extraction of the tail-only geometry and domain, 4) tail-only domain meshing withsizing mimicking that of the adapted mesh, 5) inlet and outlet conditioninterpolation from full aircraft to tail-only domain, 6) tail-only multishoticing simulation. Each icing simulation took approximately one week torun on 140 CPU processes. Fig. 9 shows a summary of the workflow.

2.2. Aerodynamic calculations

To carry out the aerodynamic calculations, each FSHT geometry, with and without ice, was remounted on the full fuselage meshed insidea hemispherical domain, for AoA variation, with an inlet boundary and asymmetry plain. The hemisphere radius was approximately 37 times theFSHT wingspan and 60 times the fuselage cross-sectional radius. The fullfuselage from nose to tail was included in the model to ensure upstreamboundary layer effects were captured throughout the AoA range. Themain wings were excluded to reduce the mesh size as they only exerted upstream influence on the tail at low absolute AoA which was not themain area of interest. Ansys Fluent meshing was used to create mesheswith tetrahedral volume cells and 26 triangular prism layers on solidboundaries with a y+ of less than one almost everywhere. Example icedand un-iced mesh sizes were 156 million and 50 million cells, respec tively. Good agreement of aerofoil pressure coefficient and FSHT lift wasobserved between this and a second grid level with 32 prism layers andrefined prism and near-aircraft volume cells.

Ansys Fluent was used to carry out the CFD calculations for AoA sweeps on the full fuselage and empennage configuration. The pressurebased Navier-Stokes solver was used to carry out steady RANS calculations of ideal gas flow at mean sea level in a standard atmosphere withinlet Mach 0.2. The k-ω SST turbulence model [36] was used withdefault settings. Other settings included viscous heating, second orderspatial integration, pseudo-time steady-state integration with a timestepping factor of 0.01, and Green-Gauss node-based gradient schemewith legacy wall treatment. These solver settings were previouslyestablished during extensive validation campaigns including high liftand drag workshops [37–40]. Table 2 shows a summary of the flight andsolver settings. The AoA was varied from 0◦ to just beyond un-iced FSHTstall at -15◦ via inlet flow pitch and the elevators were maintained in aneutral position. Negative AoA was considered most relevant as it isindicative of the ability of the horizontal stabilizer to provide downwardlift for roundout. The full set of 10 calculations for each geometry took approximately one day clean and one week iced on 140 CPU processes.

3. Results and analysis

In this section, the aerodynamic performance analysis is centred around CL-α plots, suction surface flow and spanwise lift distribution,with the objective of understanding and comparing iced low speeddownward lifting performance of the FSHT variants. Only a negativerange of AoAs is considered, from 0◦ to -15◦ and, accordingly, the abilityof the horizontal stabilizer to exert downforce. The terms negative liftingperformance, lifting performance, and absolute CL are used for this

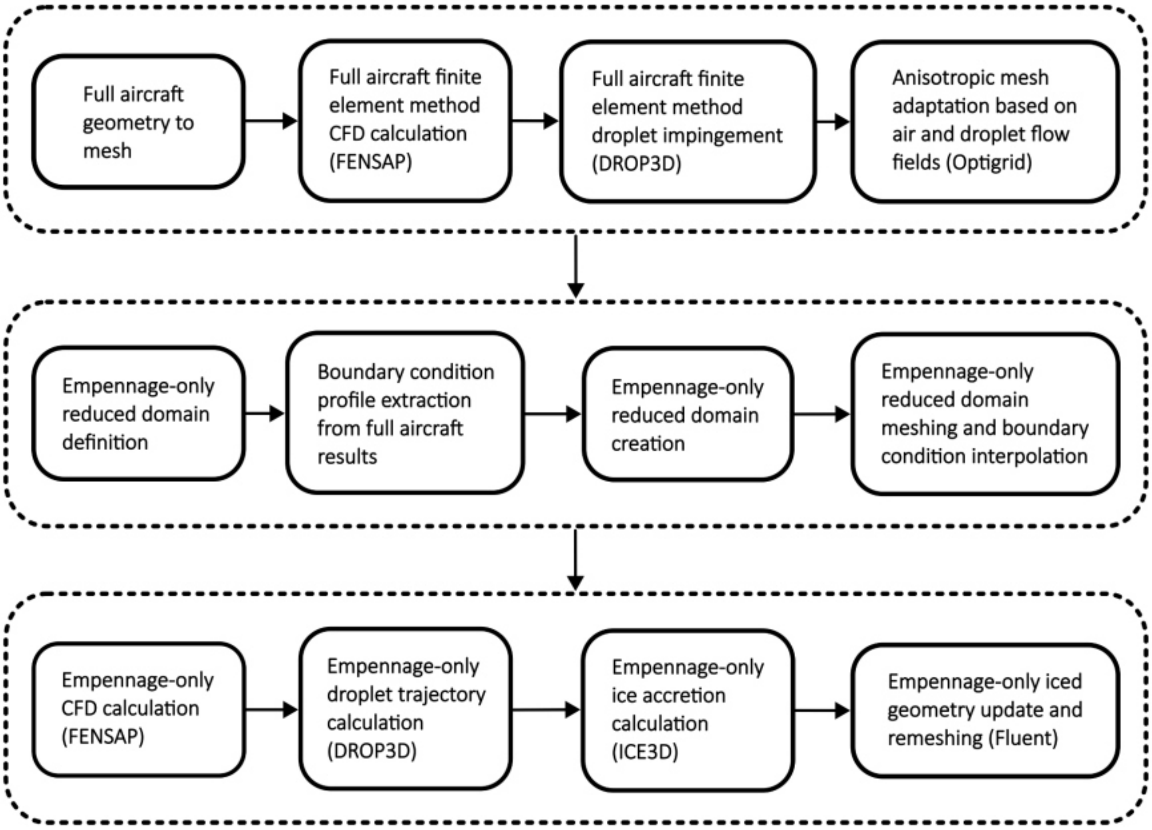

Fig. 9. Flow diagram summarizing the workflow for full aircraft-based empennage inflight icing simulation.

Table 2

Flight and solver conditions for AoA sweeps.

Type	Steady
Solver	Pressure based Navier-Stokes solver
Fluid	Compressible ideal gas
Inlet gauge pressure	101,325 Pa
Inlet static temperature	+15 °C
Inlet Mach	0.2
Turbulence model	k-ω SST turbulence model, default settings
Viscous heating	Enabled
Discretization	Second order
Pseudo-transient time stepping factor	0.01
Gradient scheme	Green-Gauss node-based with legacy wall treatment

purpose in the same sense and interchangeably. To avoid excessive use of negatives, decreasing or more negative AoA and CL are referred to asincreasing, greater or higher absolute AoA and absolute CL, or equivalent.

The calculated 45-minute ice shapes on the FSHT geometries all show significant ice accretion with sizeable upper and lower horns,typical of glaze icing, with little variation all along the main leadingedge where there is little variation in aerofoil shape and LWC. On theLEX leading edge, the ice shape shows very little ice accretion with atypical rime icing shape, where the LWC is very low in the shadow zone.The transition between the glaze and rime ice shapes is fairly sharp, inline with the shadow zone boundary in Fig. 8. Due to the focus on liftingperformance and the consistency of the main ice shape features acrossall the FSHT geometries, no further analysis of the ice shapes is presented. Fig. 10 shows the calculated ice on one of the FSHTs.

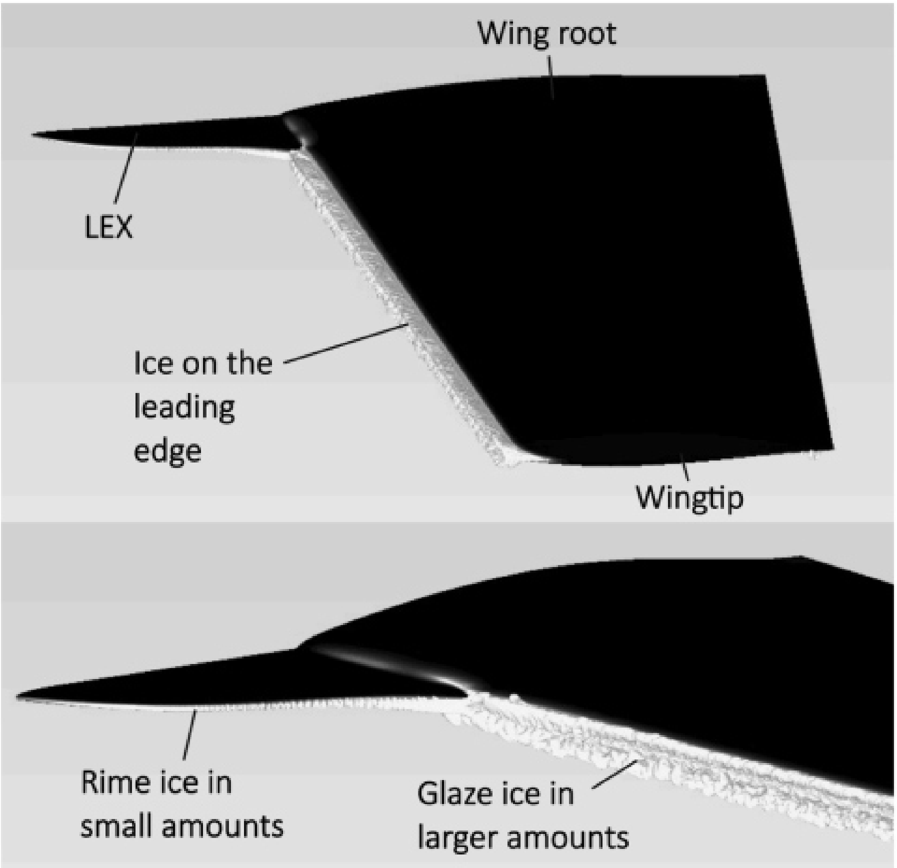

Fig. 10. 45-minute ice shape on the FSHT with LEX. This figure has been reprinted with permission from [18], © 2023 SAE International.

3.1. Effects of forward sweep

Fig. 11 shows the CL-α plots for the clean and iced FSHTs with 10◦, 15◦, and 20◦ of forward sweep. The clean plots display typical linear relationships from zero to mid absolute AoA, then a gradual change tozero gradient at absolute CL,max at higher absolute AoA. Beyond CL,max,

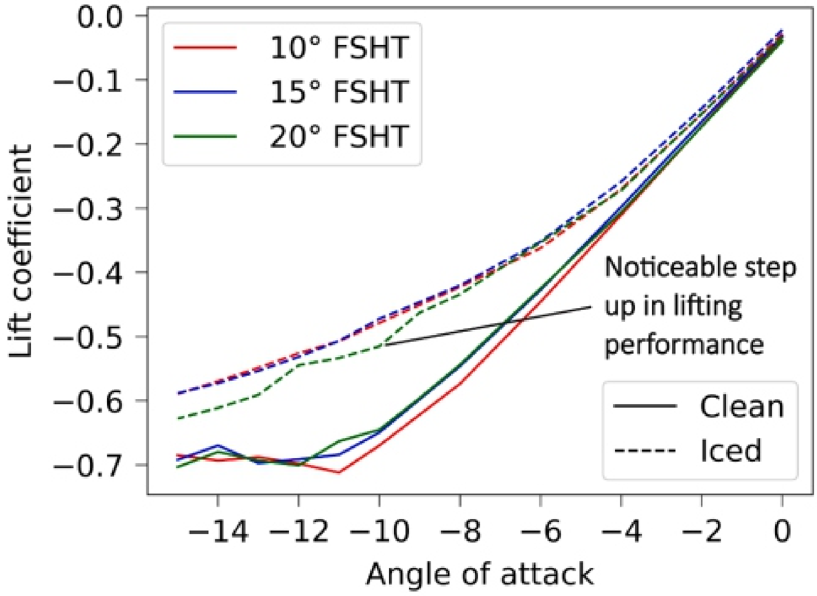

Fig. 11. C_L-α curves for the clean and iced FSHTs with 10°, 15°, and 20° forward sweep.

the clean plots are not considered reliable. The iced FSHTs exhibit CL-α curves significantly different to their clean counterparts, with very littlediscernible linear section or stall point. Rather, they show increasingabsolute CL with increasing absolute AoA. The gradient gradually decreases and CL,max is not reached. This behaviour is characteristic of allthe iced CL-α curves in this paper. The iced 10◦ and 15◦ FSHTs displayvery similar lifting performance throughout the AoA range. The moreforward swept iced 20◦ FSHT shows a tendency towards greater absoluteCL than the iced 10◦ and 15◦ cases, from 0◦ to -8◦ AoA. Between -8◦ and-10◦ AoA it shows a noticeable step up in lifting performance, which isdiscussed more detail below. Below -10◦ AoA, the 20◦ FSHT showsconsistently superior lifting performance. All three iced FSHT CL-α curves show the potential for further increases in lift well past the stallpoints of the clean counterparts. Fig. 12 shows the reductions in CL due to ice versus AoA, expressed as a percentage of clean CL. Thelimitation of calculated clean CL validity to absolute AoA up to that atabsolute CL,max confines comparison of the curves to the range -4◦ to -12◦AoA. Within this, a positive correlation of ice tolerance with forwardsweep is clearly visible.

Fig. 13 shows the wall shear stress (WSS) based surface streamlines along with contours of the X-component of WSS (WSSX), right to leftaligned with the aircraft longitudinal axis, on the suction surface of theiced 10◦ FSHT, at 0◦ AoA. The flow immediately separates (dark blue) atthe iced leading edges and reattaches shortly downstream. Local patches

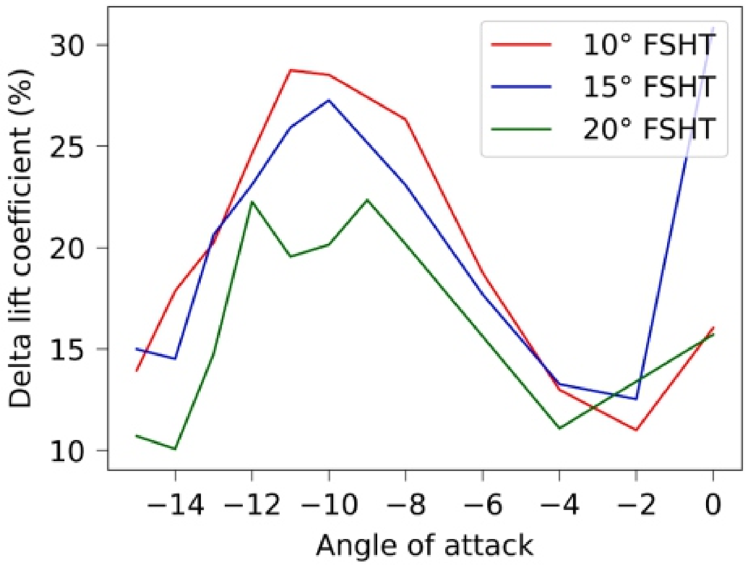

Fig. 12. Reduction in absolute C_L due to ice, expressed as a percentage of clean C_L, for the FSHTs with 10°, 15°, and 20° forward sweep.

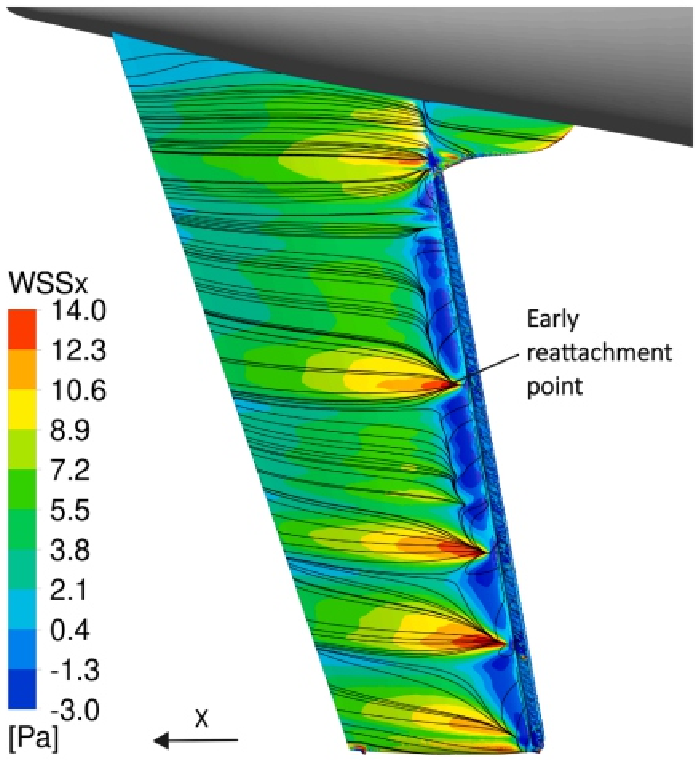

Fig. 13. Iced 10° FSHT suction (lower) surface WSS_X colour plot with surface WSS vector-based streamlines, at 0° AoA. This figure has been adapted with permission from [18], © 2023 SAE International.

of high WSS (orange and red) correspond to early flow reattachment points. These are due to the presence of local leading edge verticesmixing high momentum flow into the boundary layer. Fig. 14 showscontours of the WSS Y-component (WSSY), aligned with the aircraftlateral axis, vertically up in the plane of the figure, for comparison withFig. 13. The WSSY pattern with the high positive (red) patch immediately above the annotation shows the development of the correspondingvortex which aligns with the freestream very close to its origin.

Figs. 15 and 16 show the surface streamlines and WSSX contours for the iced 15◦ and 20◦ FSHTs, respectively, at 0◦ AoA. The spanwise frequency of the early reattachment points clearly increases with forwardsweep, with a total of four in the 10◦ case in Fig. 13, six in the 15◦ case in

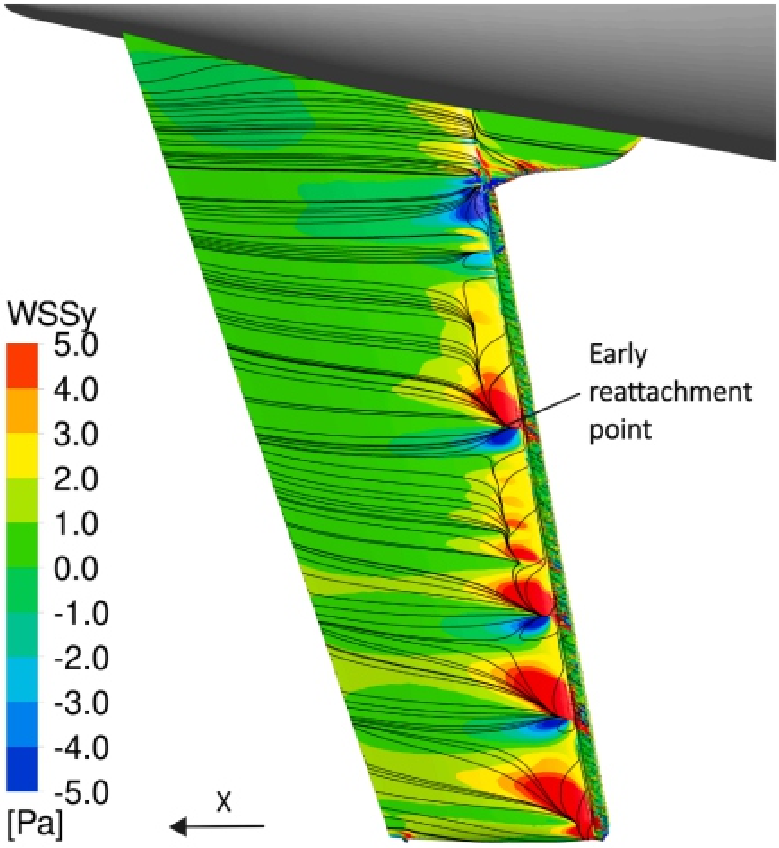

Fig. 14. Iced 10° FSHT suction (lower) surface WSS_Y colour plot with surface WSS vector-based streamlines, at 0° AoA.

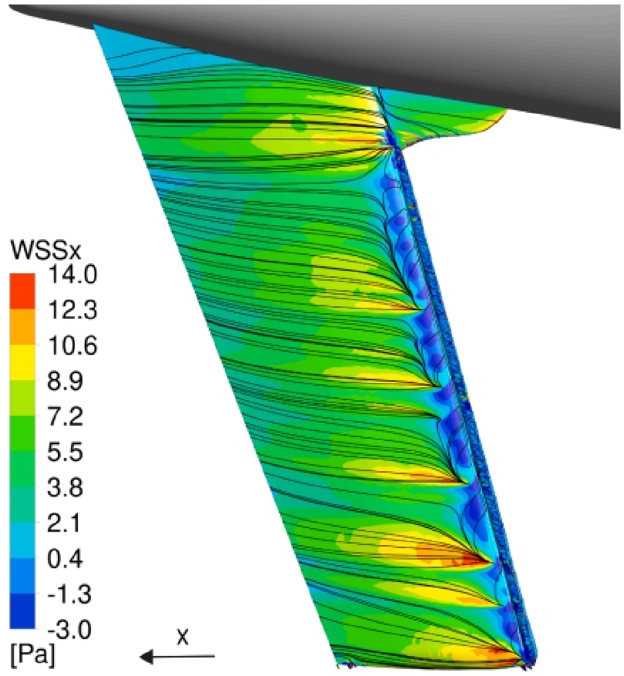

Fig. 15. Iced 15° FSHT suction (lower) surface WSS_X colour plot with surface WSS vector-based streamlines, at 0° AoA. This figure has been adapted with permission from [18], © 2023 SAE International.

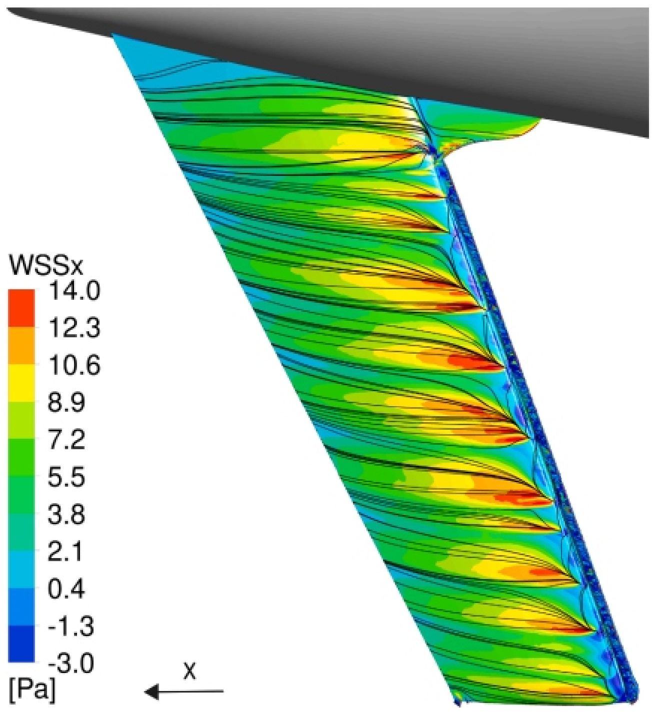

Fig. 16. Iced 20° FSHT suction (lower) surface WSS_X colour plot with surface WSS vector-based streamlines, at 0° AoA. This figure has been adapted with permission from [18], © 2023 SAE International.

Fig. 15, and ten in the 20◦ case in Fig. 16. A more detailed threedimensional visualization of the early reattachment point mechanism on the suction surface is shown in Fig. 17. The figure combines WSSXcontours on the same scale as in Fig. 16, a turbulent viscosity isosurfaceto highlight vortices, a line of black streamlines passing just below theice (above in the figure) to locate the vortices, and a line of greenstreamlines slightly below (above in the figure) the black ones to showthe high momentum flow pulled into the suction surface. The figuredemonstrates the underlying reason for the early reattachment point tobe the local formation of a tightly wound leading edge vortex behind the

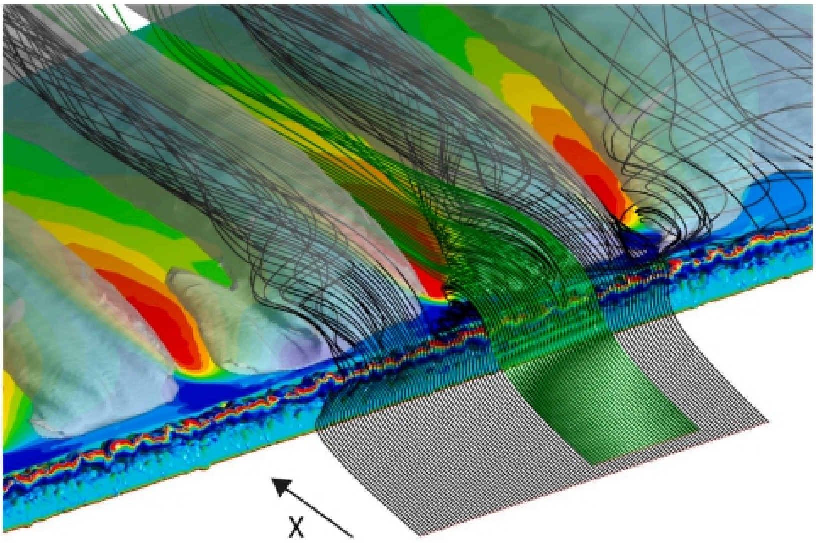

Fig. 17. Three dimensional visualization of early reattachment points on the suction surface of the 20° FSHT at -4° AoA. There are WSS_X surface contours on the same scale as in Fig. 16, a turbulent viscosity isosurface, black streamlines impinging on the leading edge ice, and green streamlines 3 cm below (above in the image).

horn of the ice, with the initially leading edge-aligned rotational axis turning quickly downstream. The vortex appears to originate betweentwo small bulges in the ice shape. However, the strong correlation of theearly reattachment points with sweep suggests that the spatial frequencyof the flow mechanism is rather more dependent on sweep and possiblythe general ice shape than the minutiae.

Figs. 18–20 show the suction surface streamlines and WSSX contours for the 10◦, 15◦, and 20◦ FSHTs, respectively, at -8◦ AoA. Inspection ofthe flow patterns reveals two aspects of interest: firstly, the continuedpresence of an early reattachment point in the 20◦ FSHT case, whichindicates persistence of that flow mechanism at higher absolute AoAwith greater forward sweep; and secondly, the development of twoopposing surface crossflows, one emanating from a tip leading edgevortex and another from the LEX vortex. These are annotated in Fig. 18 and will be referred to as the tip inward crossflow and root outward crossflow. The crossflows coincide in the mid spans towards the trailing

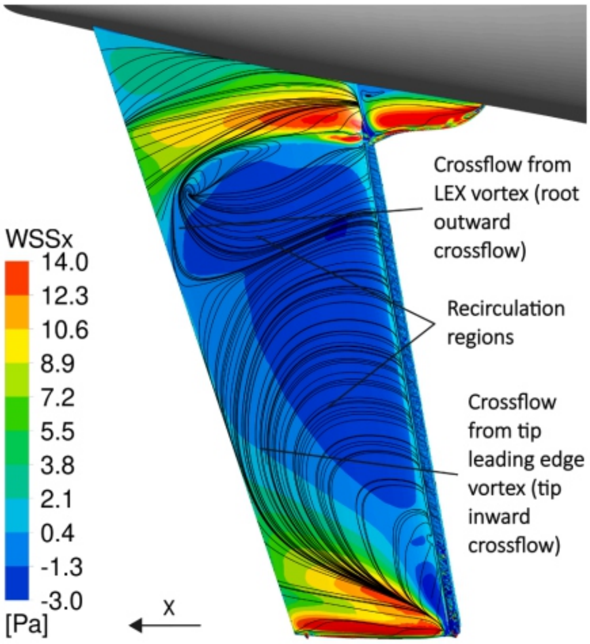

Fig. 18. Iced 10° FSHT suction (lower) surface WSS_X colour plot with surface WSS vector-based streamlines, at -8° AoA. This figure has been adapted with permission from [18], © 2023 SAE International.

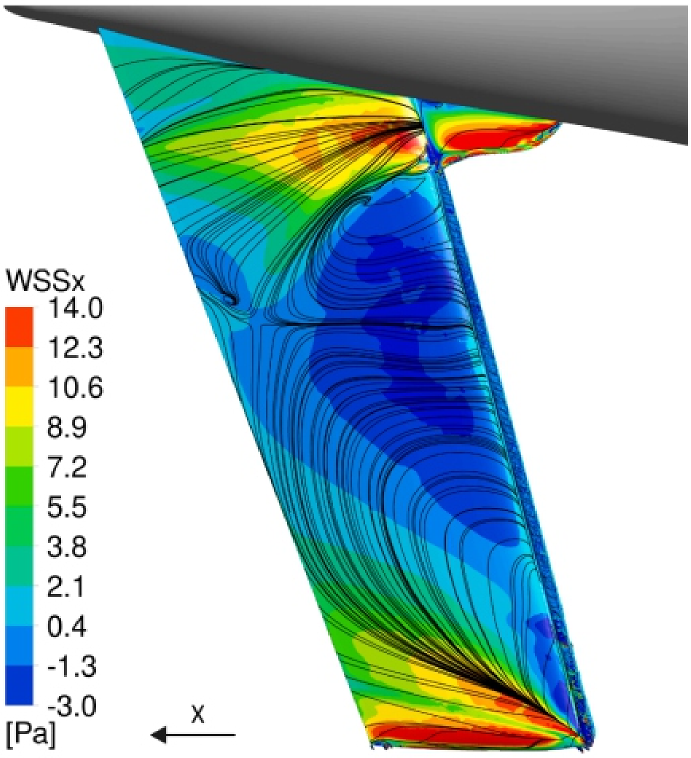

Fig. 19. Iced 15° FSHT suction (lower) surface WSS_X colour plot with surface WSS vector-based streamlines, at -8° AoA. This figure has been adapted with permission from [18], © 2023 SAE International.

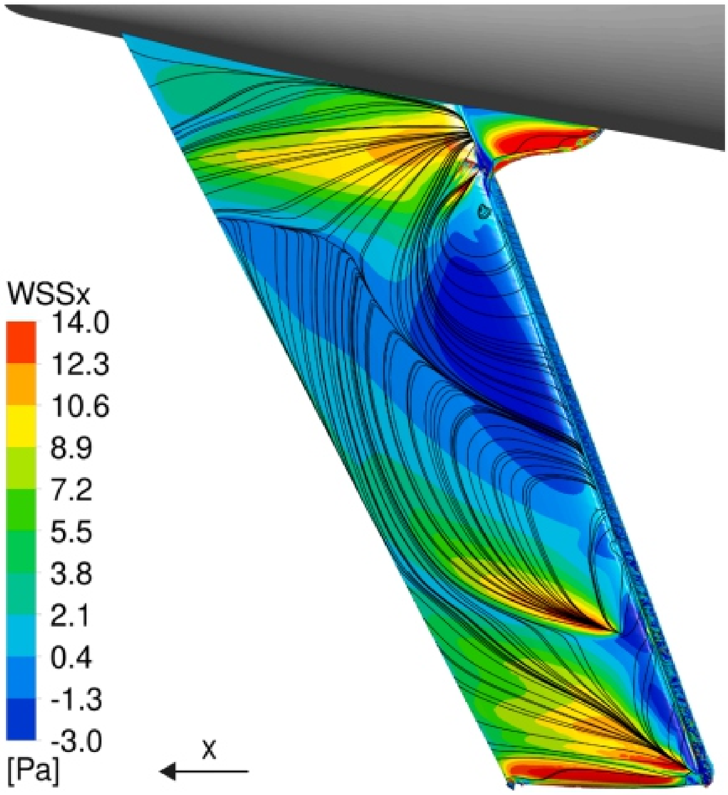

Fig. 20. Iced 20° FSHT suction (lower) surface WSS$_X$ colour plot with surface WSS vector-based streamlines, at -8° AoA. This figure has been adapted with permission from [18], © 2023 SAE International.

edge behind two regions of reverse flow, also annotated in Fig. 18, which extend forwards to the leading edge. The extension of the tip inward crossflow towards the wing root increases with forward sweep until itinteracts with the LEX vortex flow. The area covered by reverse flow,indicated by the dark blue patches in the figures, is reduced and moreconfined towards the inner spans with greater forward sweep.Fig. 21 shows the suction surface streamlines and WSSx contours,plotted on the same scale as above, for the 10◦, 15◦, and 20◦ FSHT casesat 0◦, -4◦, -8◦, -10◦, and -13◦ AoA. The progression of the early reattachment point flow mechanism with AoA clearly shows the increase in spanwise frequency and persistence to higher absolute AoA with greater forward sweep. In contrast to the 10◦ and 15◦ cases, the 20◦case continues to exhibit the mechanism fully and partially at -4◦ and -8◦AoA where it also has the greatest absolute CL. This gives an indicationof a mid to outer span ice tolerance flow mechanism positively correlated with forward sweep at low to medium absolute AoA.

From -8◦ AoA, the progressions of the tip inward and root outward crossflow interplays shows a clear trend with increase in forward sweep.In the 10◦ FSHT case, the root outward crossflow emanating from theLEX vortex increases in extent towards the tip as absolute AoA isincreased, reaching the mid span at -13◦ AoA. In the 15◦ case, however,this does not happen and the spanwise extents of both crossflows remain largely unchanged, with them meeting in the mid span. In the 20◦ case,at -8◦ AoA, the transition from multiple local leading edge vortices to alarger single tip leading edge vortex is not yet complete. At -10◦ AoA, thetip inward crossflow emanating from the tip leading edge vortex extendsall the way to the LEX vortex, and remains as such at -13◦ AoA. The rootinward crossflow is completely contained. The establishment of this flowpattern at -10◦ AoA coincides with the step up in lifting performanceannotated in Fig. 11. This gives an indication of another ice toleranceflow mechanism positively correlated with forward sweep, this time at higher absolute AoA.

To quantify this, Fig. 22 shows the spanwise lift distributions on the clean and iced 10◦, 15◦, and 20◦ FSHTs, at -10◦ AoA. Fig. 23 shows thesame, with focus on the LEX and inner span. The clean lift distributionshave a typical shape with the addition of significant lift spikes local tothe LEXs. The iced lift distributions all have a spike at the LEX, aninner-mid span region of relatively low lift corresponding to the rootoutward crossflow, an outer-mid span region of lift linearly increasing inmagnitude towards the tip corresponding to the tip inward crossflow,and an ice tolerant outer span region, with iced lift similar to clean lift,corresponding to the origin of the tip leading edge vortex. Two keytrends in the lift with respect to forward sweep are observed. The first isthat the ice-induced degradation of the LEX lift spike increasessignificantly with forward sweep. The reductions in peak absolute liftper m span are 16 %, 25 %, and 29 % for the 10◦, 15◦ and 20◦ FSHT,respectively. The second trend is that the spanwise extent of the icetolerant outer span region increases with forward sweep. This highlightsan interplay between the inner and outer span lifting flow mechanisms,which is enough to mitigate the increase in ice-induced LEX liftdegradation between the 10◦ and 15◦ cases. The trend is morepronounced between the 15◦ and 20◦ cases. Significantly greaterbreadth of the tip leading edge vortex ice tolerant outer span lift region, in the 20◦ case, outweighs the greater ice-induced LEX lift degradation, leading to the step up in lifting performance annotated in Fig. 11.

To contextualize the spanwise lift distribution observations, Fig. 24 shows the suction surface streamlines and static pressure contours, forthe 10◦, 15◦, and 20◦ FSHT cases at 0◦, -4◦, -8◦, -10◦, and -13◦ AoA. At -4◦AoA the greater persistence of small low (dark blue) static pressure areasalong the leading edge in the 20◦ case are clearly visible. At -8◦ AoA theemergence of larger low static pressure areas can be seen as the flowsdevelop into those with single leading edge vortices at the tip.At -10◦ and -13◦ AoA the development of a much larger low staticpressure area at the tip leading edge vortex in the 20◦ FSHT casecorresponds to the much larger ice tolerant outer span region identifiedin Fig. 22. This is clearly observable as due to the strength of the tipleading edge vortex, which extends all the way inwards to the LEX. Atthese AoAs, the areas of moderately low (light blue)static pressure in theinner mid span seen in the 10◦ and 15◦ case are also not present in the20◦ case. A graphical summary of the major identified iced FSHT flowmechanisms at higher absolute AoA is shown in the schematic diagram involves 10 % and 20 % chordwise size increases. The second type involves 10 % and 20 % spanwise size increases. Fig. 26 shows the FSHT geometries resulting from the first LEXchordwise size increases.

Fig. 27 shows the CL-α plots for each LEX chord variant, clean and iced, alongside those for one without LEX for context. The clean plotsshow increased stalling absolute AoAs and absolute CL,max for the plus 10% and plus 20 % chord LEXs. The iced CL-α curves show little noticeablevariation between the variants until -9◦ to -10◦ AoA, beyond which theCL values are again very similar. At -9◦ AoA, the plus 10 % chord case hasthe greatest absolute CL of the three cases, before a noticeable step downin lifting performance, to that of the baseline LEX case, by -10◦ AoA. Theplus 20 % chord case displays a more subtle version of the same patternbetween -10◦ and -11◦ AoA. The iced CL-α curve for the variant without

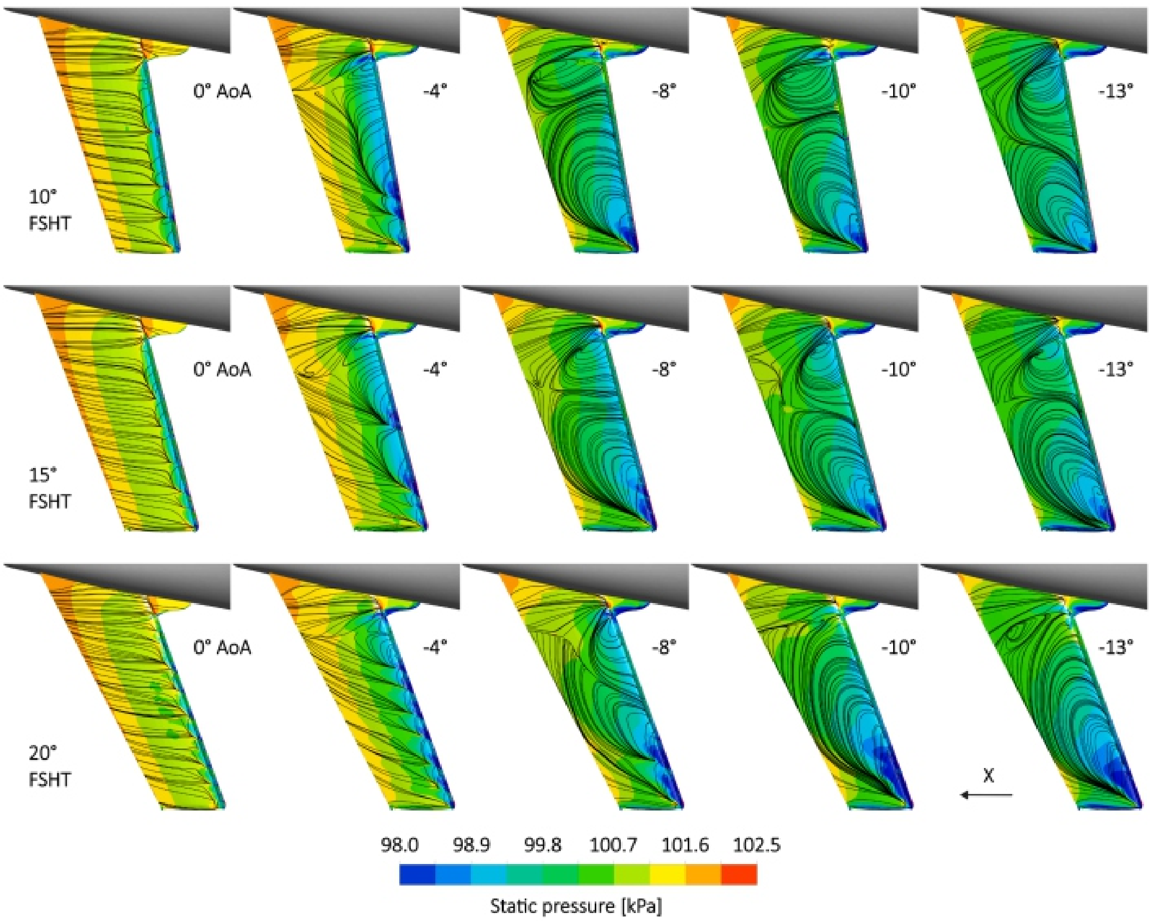

Fig. 24. Suction (lower) surface static pressure colour plots with surface WSS vector-based streamlines. The rows are iced 10°, 15°, and 20° FSHTs. The columns are 0°, -4°, -8°, -10°, and -13° AoA.

in Fig. 25.

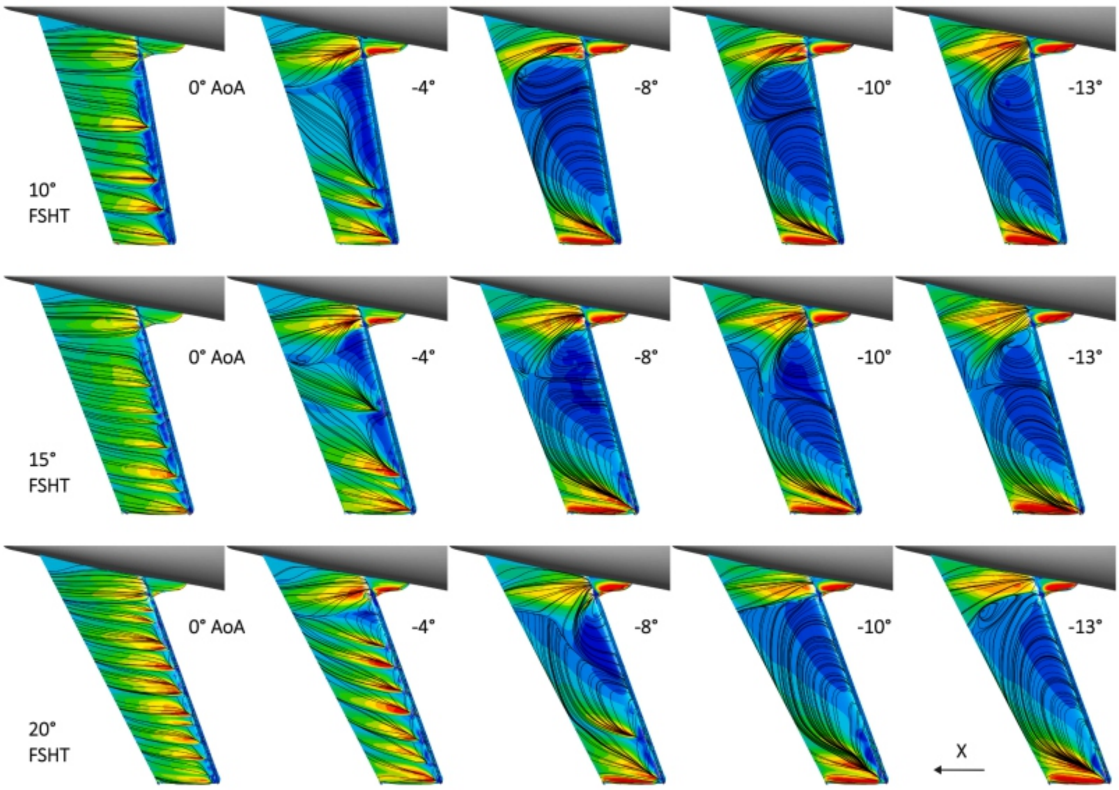

Fig. 21. Suction (lower) surface WSS_X colour plot, with the same scale as Fig. 18 to Fig. 20, with surface WSS vector-based streamlines. The rows are iced 10°, 15°, and 20° FSHTs. The columns are 0°, -4°, -8°, -10°, and -13° AoA. The 0° and -8° AoA results have already appeared in different format in reference [18].

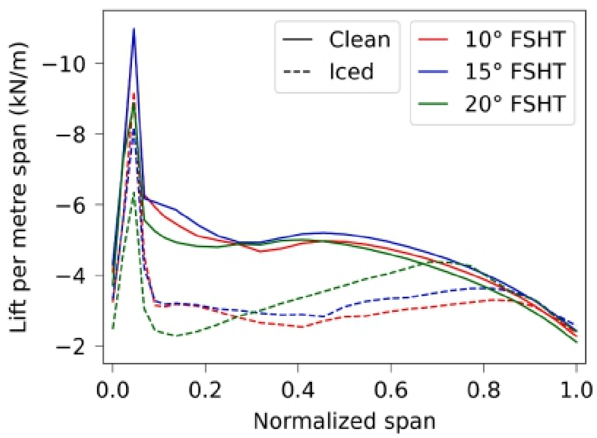

Fig. 22. Spanwise distribution of lift in the form of the integral of streamwise surface static pressure cuts, at -10° AoA.

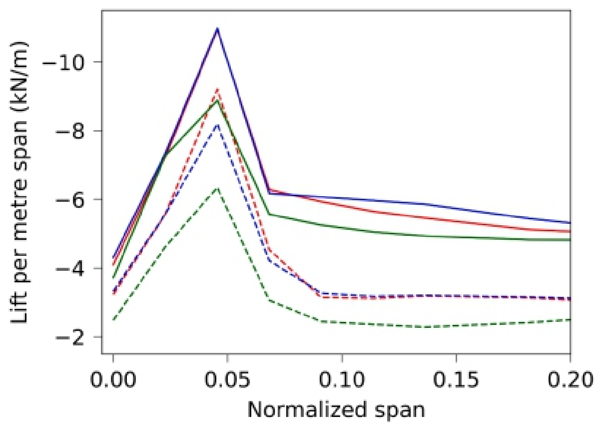

Fig. 23. Spanwise distribution of lift in the form of the integral of streamwise surface static pressure cuts, at -10° AoA.

3.2. Effects of LEX sizing

Two types of LEX sizing variation were investigated with the 10° FSHT. The first type analyzed

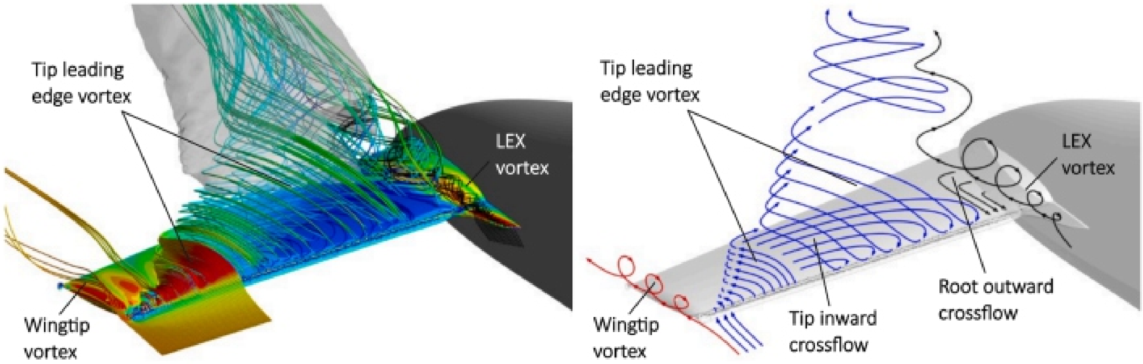

Fig. 25. Iced FSHT CFD-calculated streamlines (left) and corresponding schematic diagram (right) showing the dominant suction (lower) surface flow mechanisms at medium to large negative AoA. Note: the image presents the FSHT suction surface as if it were the upper surface for ease of viewing.

LEX has a noticeably lower absolute CL from between -4◦ and -8◦ AoA all the way to the limit of the range at -15◦. The deficit relative to thebaseline is relatively subtle until -11◦ AoA where the ice-induced CLreduction is 30.1 % compared with 28.7 % for the baseline. However, astep down in lifting performance of the FSHT without LEX between -11◦and -12◦ AoA puts absolute CL 7.1 % lower than that of the baseline by-14◦ AoA, 8.3 % lower by -15◦, and on a trajectory to further divergebeyond range. This gives an indication of the ice tolerance value of theLEX.

Fig. 28 shows the progressions of the suction surface streamlines andWSSx contours for the three LEX chord variants, plotted on the samescale as Figs. 13 and Figs. 15–20. Observing from left to right with

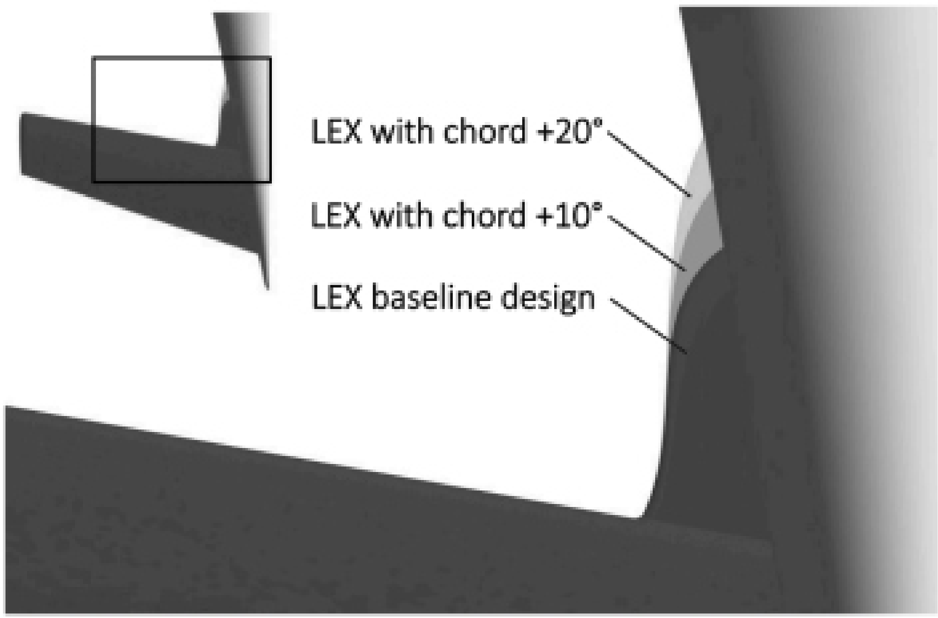

Fig. 26. LEX chordwise geometry variations baseline, plus 10 % chord, and plus 20 % chord.

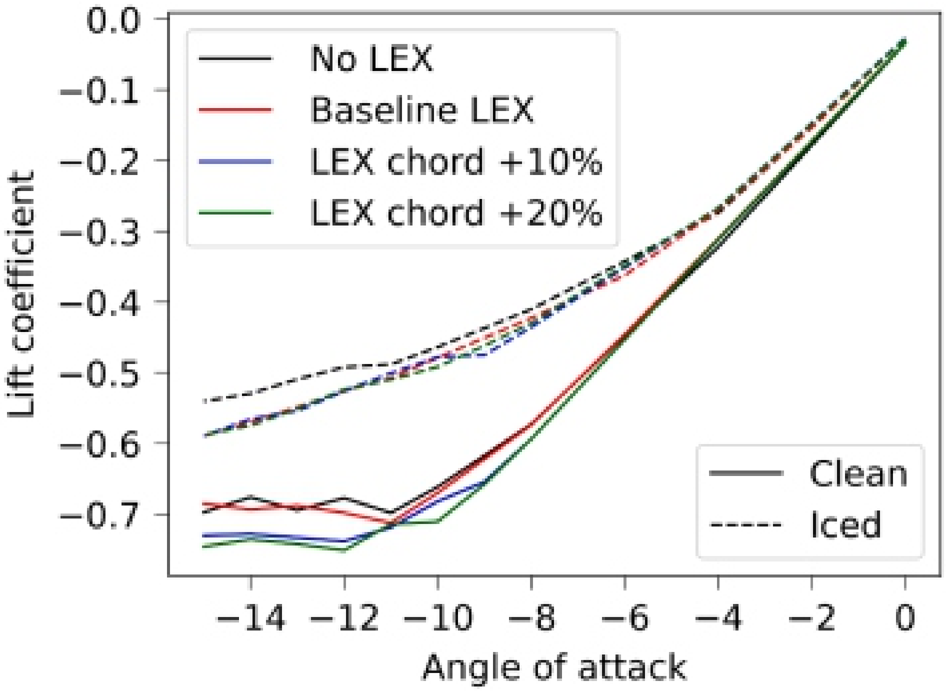

Fig. 27. C_L-α curves for the clean and iced 10° FSHTs with no LEX, baseline LEX, plus 10 % chord LEX, and plus 20 % chord LEX.

increasing absolute AoA, the first observation is the variation in the spanwise distribution of early reattachment points, at 0◦ and -4◦ AoA,which was analysed in the context of forward sweep in Section 3.1above. This gives some indication of flow variation attributable to differences in the three-dimensional ice shape undulations along theleading edge.

At -8◦ AoA, the effects of the LEX vortex can be seen, along with thetip leading edge vortex and tip inward crossflow. Here, the extent of theroot outward crossflow from the LEX is greatest for the baseline reduces with increase in LEX chord, being minor for the plus 10 % chordLEX and non-existent for the plus 20 % chord LEX with the tip inwardcrossflow extending all the way to the LEX. This coincides with theimproved CL with increased LEX chord at this AoA. Following the AoA to-10◦ and -13◦, the spanwise extent of the baseline LEX root outwardcrossflow progressively increases towards half span, pushing out theboundary with the tip inward crossflow. The root outward crossflow forthe plus 10 % chord LEX, having been largely suppressed, makes a morerapid advance to half span by -10◦ AoA, coinciding with the step down inlifting performance between -9◦ and -10◦ AoA in Fig. 27. The rootoutward crossflow for the plus 20 % chord LEX remains suppressed at-10◦ AoA and advances to half span by -13◦ AoA. Here the spiralingsurface streamlines indicate tip leading edge vortex breakdown. Thisidentifies a trend towards persistence of the (almost) full span tipleading edge vortex to greater absolute AoA with increased LEX chord,but then also more rapid subsequent retreat and

and potential breakdown.

Figs. 29–34 show the spanwise lift distributions for the three LEX chord variants, clean and iced, at -8◦, -10◦, and -13◦ AoA. The iced liftdistributions broadly exhibit the same regions, LEX lift spike, inner-midspan, outer-mid span linearly increasing lift magnitude, and outer spanice tolerant region, as seen in Fig. 22. In Figs. 29 and 30, at -8◦ AoA, apositive correlation between LEX lift spike magnitude and LEX chordlength, is clearly visible, both clean and iced. There is also a positivecorrelation between ice-induced lift spike deficit and LEX chord length,with the percentages being 8.0 %, 11.4 %, and 13.3 % for the baseline,plus 10 % case, and plus 20 % case, respectively. The baseline LEXdistribution has a larger inner-mid span region, less lift in its inner- andouter-mid span regions, and a smaller outer ice tolerant region than thatof the plus 10 % and 20 % cases. This coincides with its extended rootoutward crossflow in contrast to the almost full span tip inward crossflows of the plus 10 % and 20 % cases. In Figs. 31 and 32, at -10◦AoA, the plus 10 % case has the largest spike, inner span lift magnitude,and inner-mid span region of the iced cases. It also has the lowest lift inthe outer-mid and outer spans. This corresponds to it now having thegreatest extent of the root outward crossflow from the LEX vortex. InFigs. 33 and 34, at -13◦ AoA, with all three LEX cases now havingsignificant and similar root outward crossflows, the positive correlationbetween LEX lift spike magnitude and LEX chord length is again present,and all have reduced lift in the outer-mid spans and degraded outer spanice tolerant regions. The case without LEX maintains an outer span icetolerant region lifting performance which is comparable with that of the20 % chord case at -8◦ and -10◦ AoA and noticeably superior at -13◦ AoA.Its inner span lift, however, is comparatively very low and reduces between -10◦ and -13◦ AoA. This is in contrast with the LEX spikes whichcontinue to increase in magnitude. This observation coincides with therelative step down in lifting performance of the case without LEX beyond-11◦ AoA in Fig. 27. As observed in the forward sweep study above, thereis an interplay between the inner and outer span lifting mechanisms,where strengthening of one tends to be accompanied by weakening ofthe other.

Fig. 35 shows the FSHT geometries resulting from the LEX spanwise variations. Fig. 36 shows the 45-minute ice shapes on the three LEXvariants. The baseline LEX has only a small amount of rime ice lining theleading edge. The plus 10 % and plus 20 % span LEXs, on the other hand,have considerably greater amounts of scallop shaped ice around the sidedue to their extension out of the droplet shadow zone. Fig. 37 shows theCL-α curves for each variant, clean and iced. The iced CL-α curves forboth the plus 10 % and plus 20 % span cases show similarly reducedlifting performance in comparison to the baseline, throughout the AoArange. In contrast to the forward sweep and LEX chord studies above, nosteps up or down in iced lifting performance are observed here.

Fig. 38 shows the progressions of the suction surface streamlines andWSSx contours for the three LEX span variants, plotted on the same scaleas Figs. 13 and Figs. 15–20. Moving from left to right with increasing absolute AoA, the first observation is a tendency towards reduction insize, strength, and number of high local WSSx patches associated withearly reattachment points, at 0◦ and -4◦ AoA, with increase in LEX span.Already at -4◦ AoA an increased tendency toward extension of the rootoutward crossflow with increased LEX span can be seen. This tendencypersists at -8◦ and -10◦ AoA. In the plus 10 % LEX span case, at -10◦ AoA,the tip leading edge vortex and tip inward crossflow mechanism is seento have broken down mid span. This persists at -13◦ AoA. In the plus 20% LEX span case, the tip leading edge vortex and tip inward crossflowmechanism is seen to have similarly broken down already at -8◦ AoA.This persists at -10◦ AoA. However, by -13◦ AoA, reverse flow hasappeared on the LEX surface and the root outward crossflow hasretreated. The tip leading edge vortex is at this point reestablished.

Figs. 39–41 show the spanwise lift distributions for the three LEXspan variants, clean and iced, at -8◦, -10◦, and -13◦ AoA. The iced liftdistributions again broadly exhibit the same regions as in the previous studies above: LEX lift spike, inner-mid span, outer-mid span linearlyincreasing lift magnitude, and outer span ice tolerant regions. At all

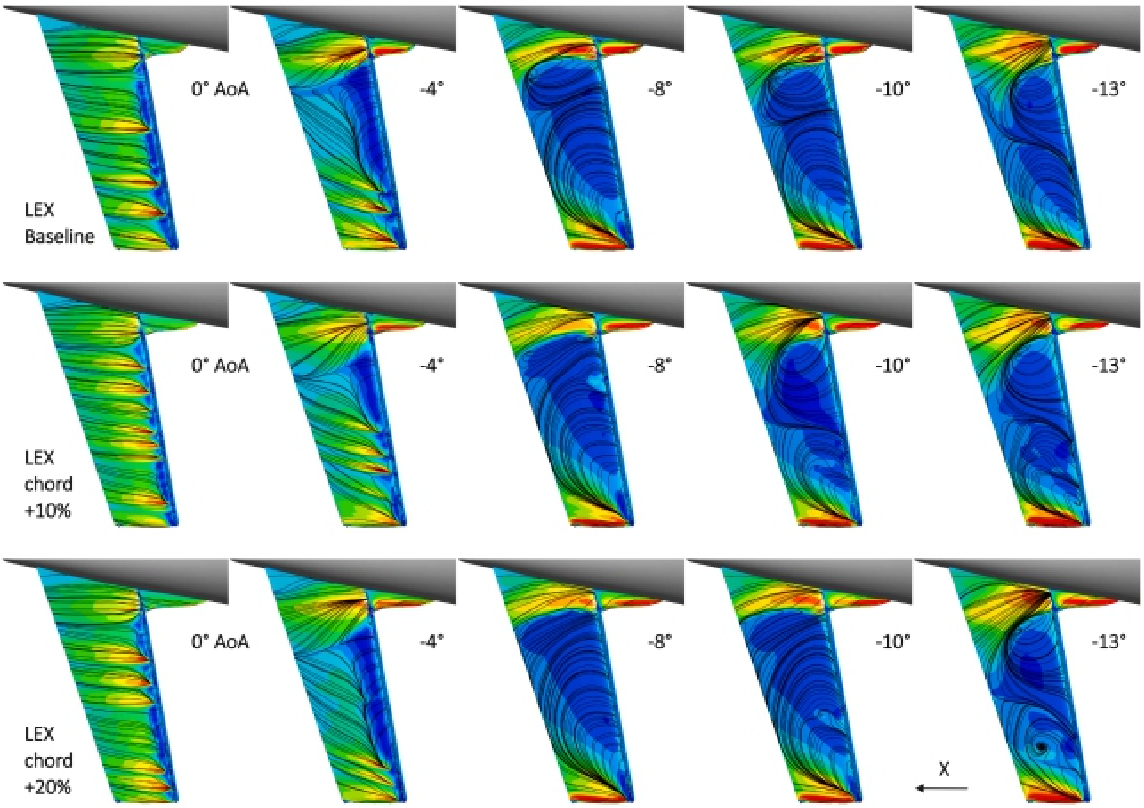

Fig. 28. Suction (lower) surface WSS_X colour plot, with the same scale as used throughout this paper, with surface WSS vector-based streamlines. The rows are the iced 10◦ FSHTs with baseline, plus 10 % chord, and plus 20 % chord LEXs. The columns are 0◦, -4◦, -8◦, -10◦, and -13◦ AoA.

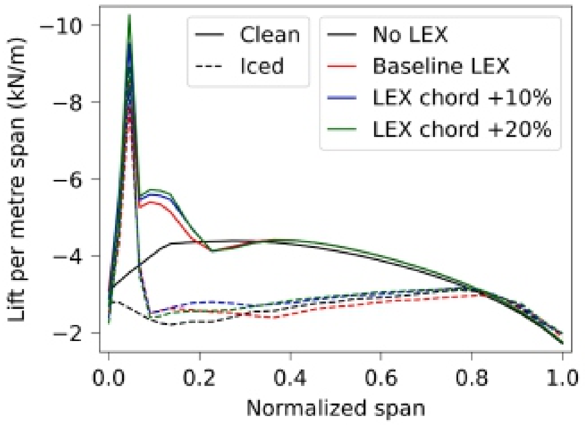

Fig. 29. Spanwise distribution of lift in the form of the integral of streamwise surface static pressure cuts, at -8◦ AoA.

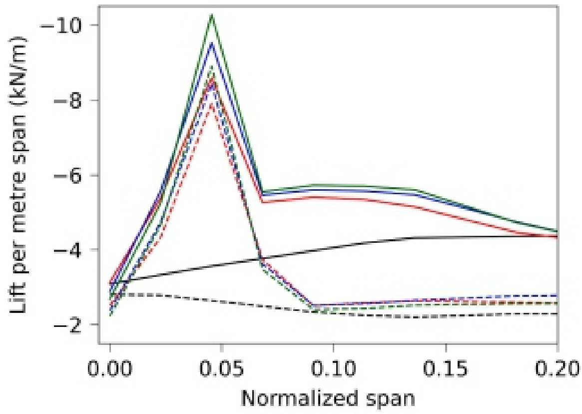

Fig. 30. Same as Fig. 29 with focus on the LEX region.

hree AoAs, the LEX lift spike widens and decreases in amplitude as LEX span is increased, both clean and iced. In Fig. 39 at -8◦ AoA, the iceinduced lift spike deficits are 8.0 %, 12.4 %, and 9.0 % for the base line, plus 10 % span, and plus 20 % span cases, respectively. The increase in deficit between the baseline and the plus 10 % case points to apotential tendency towards reduction in LEX lift spike ice tolerance withincrease in LEX span, as would be expected with the increase in LEX ice.This is, however, not confirmed by the plus 20 % span value. Thebreakdown of the tip leading edge vortex in this case could, previousanalysis in this paper suggests, increase the LEX lift spike magnitude,confounding the comparison with the other cases. The plus 20 % casehas greater lift around 0.2 span with the greater extent of its root outward crossflow, and less lift in the outer-mid and outer ice tolerant regions with the breakdown of the tip leading edge vortex. In Fig. 40 at-10◦ AoA, the ice-induced lift spike deficits are 15.9 %, 19.3 %, and 19.9%, respectively, providing more evidence of reduction in LEX lift spikeice tolerance with increase in LEX span and ice. The plus 10 % case andeven more so the plus 20 % case have reduced lift magnitudes in their

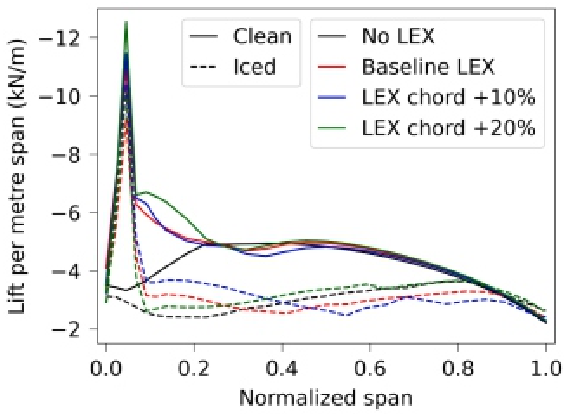

Fig. 31. Spanwise distribution of lift in the form of the integral of streamwise surface static pressure cuts, at -10° AoA.

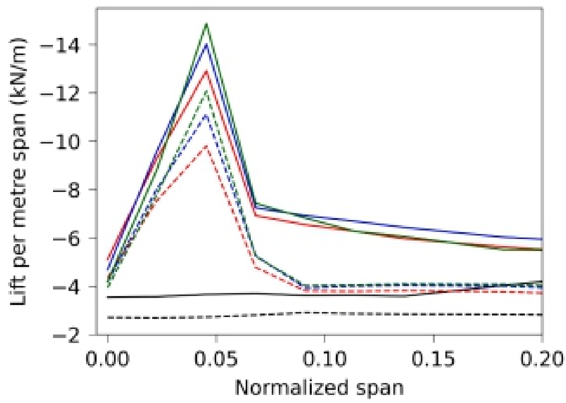

Fig. 34. Same as Fig. 33 with focus on the LEX region.

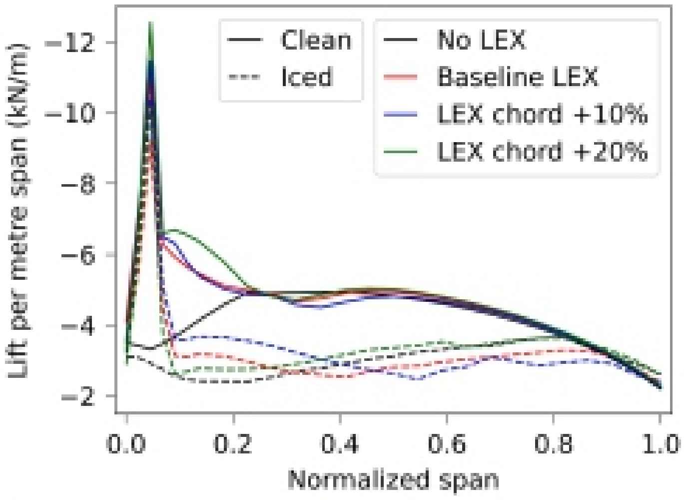

Fig. 31. Spanwise distribution of lift in the form of the integral of streamwise surface static pressure cuts, at -10° AoA.

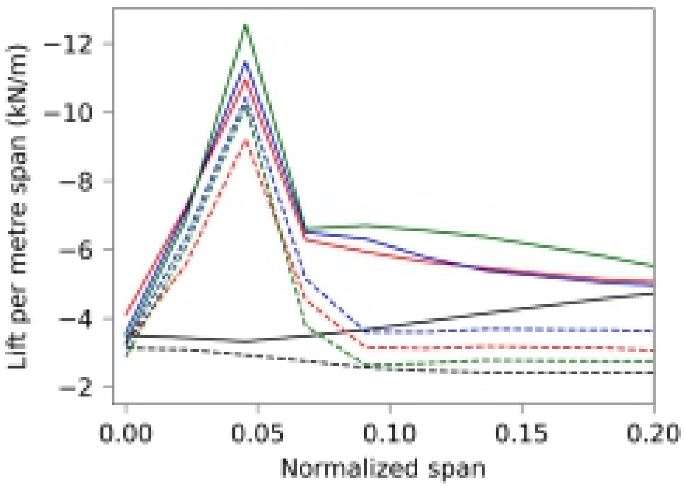

Fig. 32. Same as Fig. 31 with focus on the LEX region.

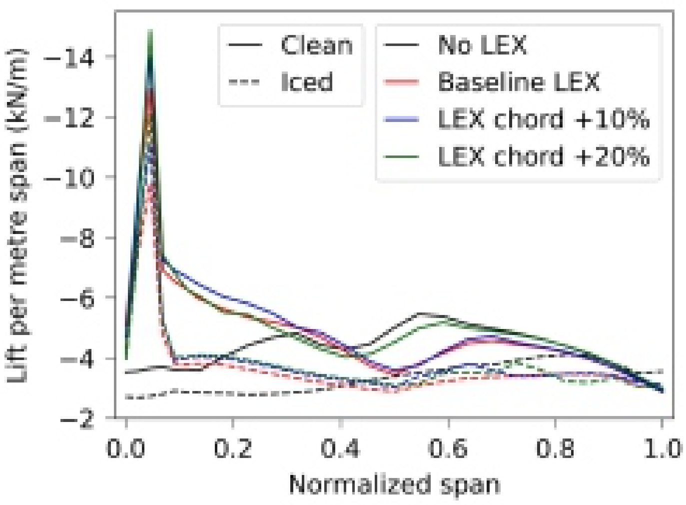

Fig. 33. Spanwise distribution of lift in the form of the integral of streamwise surface static pressure cuts, at -13° AoA.

outer-mid span and ice tolerant outer span regions, in comparison to the baseline. This is in line with the reduced extents and breakdowns of theirtip leading edge vortices. At -13◦ AoA, the appearance of reverse flow onthe iced plus 20◦ span LEX is seen to correspond to a significant

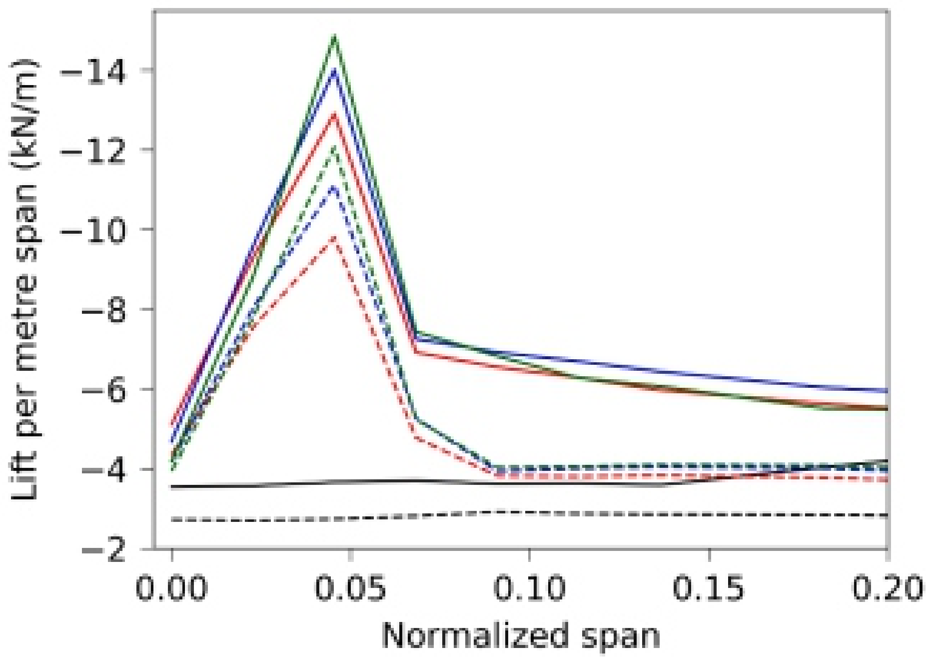

Fig. 34. Same as Fig. 33 with focus on the LEX region.

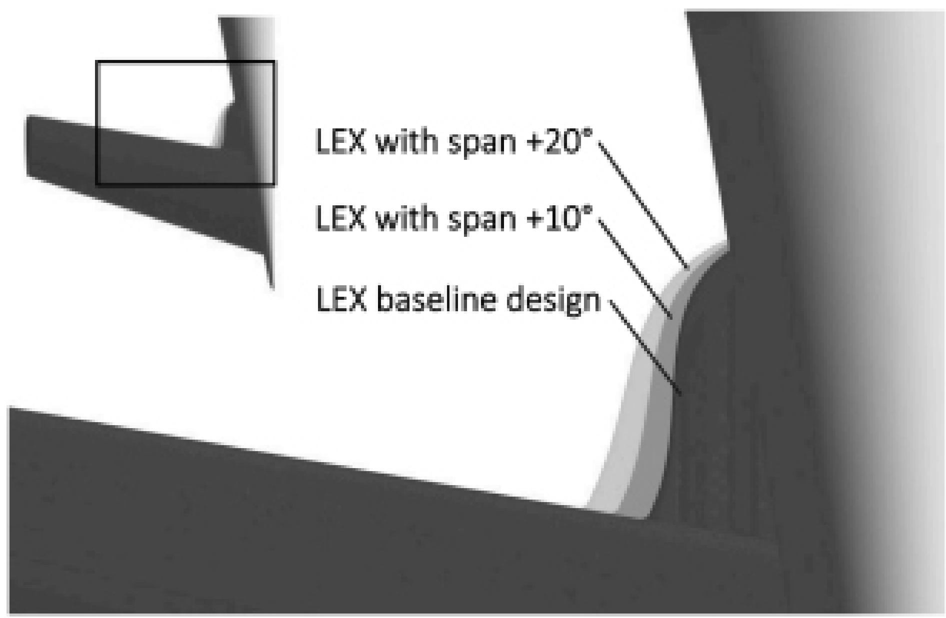

Fig. 35. LEX spanwise geometry variations baseline, plus 10 % span, and plus 20 % span.

reduction of the lift spike and an increase in lift at the mid and outer spans, in line with the reassertion of the tip leading edge vortex. Thedecrease in lift at the LEX due to separation may be underestimated, as isthe case in clean wing stall with the k-ω SST turbulence model. Again, itis observed that a reduction in inner and inner-mid span lifting performance tends to be offset by improvement it the outer-mid and outer spanlift, and vice versa.

4. Discussion

The analysis of iced FSHT suction surface aerodynamics has shown it to be significantly different to that of clean FSHTs. The major flowmechanisms of the iced FSHT with LEX identified are: the LEX vortexand ‘root inward crossflow’, local leading edge vortices and associatedearly reattachment points at low absolute AoA, and the tip leading edgevortex and ‘tip inward crossflow’ at medium to high absolute AoA. Thestudies of the effects of variation in forward sweep, LEX chord, and LEXspan throughout the range of negative AoA reveal variation in the intensity and spatial frequency of the local leading edge vortices and earlyreattachment points, variation in the magnitude and breadth of the vortex lift spike, variation in the extent of and lift magnitude in the icetolerant outer span region and, possibly most interestingly, the complexinterplay between the LEX vortex lift and root outward crossflowmechanism and the tip leading edge vortex and tip inward crossflowmechanism. All these effects are shown to have influence on iced lowspeed lifting performance and, hence, FSHT ice tolerance.

The early reattachment point mechanism is reminiscent of the type II

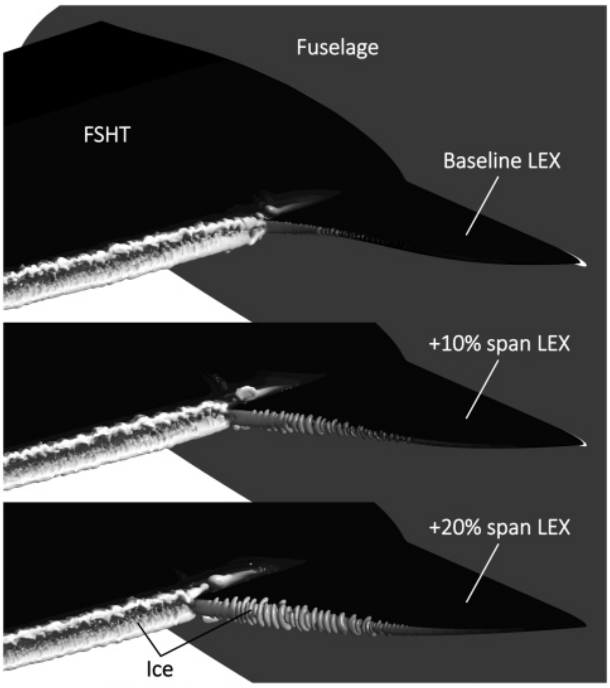

Fig. 36. 45-minute ice shapes on the baseline, plus 10 % span, and plus 20 % span LEXs.

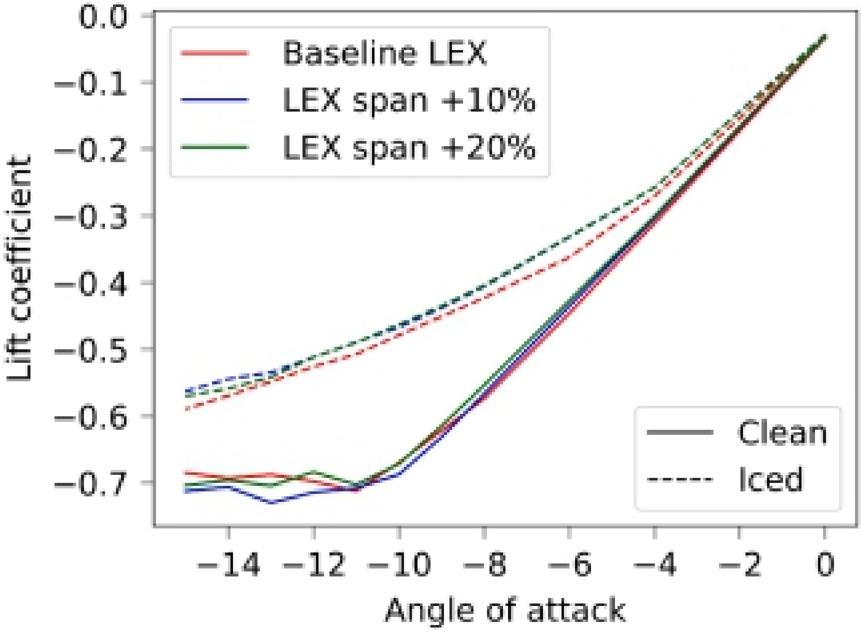

Fig. 37. C_L-α curves for the clean and iced 10◦ FSHTs baseline, plus 10 % span, and plus 20 % span LEXs.

flowfield [22,23] which was suggested in [22] to be formed of many small streamwise aligned counter rotating vortices. In this paper themechanism is characterized by many small leading edge vortices whichturn almost immediately downstream. The tip leading edge vortexmechanism is very similar to the type I flowfield of iced rearward sweptwings [22,23], with the main differences being the interactions with thewingtip vortex at the origin and the root outward crossflow.

The study of the effects of iced FSHT forward sweep was carried outon three geometry variations: 10◦, 15◦, and 20◦ of forward sweep, withthe baseline gothic LEX. On the top level, the research identifies a cleartrend towards increase in ice tolerance with increase in forward sweepwithin the range investigated. In more detail, it is shown that twocompeting effects play out as forward sweep is increased. The first is thedecrease of the spanwise extent (and eventual suppression of) the rootoutward crossflow, reduction of the LEX lift, and reduction of LEX icetolerance. The second is the increase in the spanwise coverages of the tipleading edge vortex, tip inward crossflow, and associated ice tolerantouter span lift region. The increase in absolute CL due to the secondeffect is shown in the CL-α plots to outweigh the reduction due to thefirst. This highlights the tip leading edge vortex as a flow mechanism ofkey importance with respect to low speed iced lifting capability and icetolerance. It also identifies sweep as a key parameter in this context. The apparent tradeoff between the inner and outer span iced lifting mechanisms suggests the possibility that more exotic solutions such as variable forward sweep or boundary layer fences could be relevant.

The study of the effects of LEX chord was carried out with the 10◦ FSHT with three LEX variants: baseline, plus 10 % chord, and plus 20 %

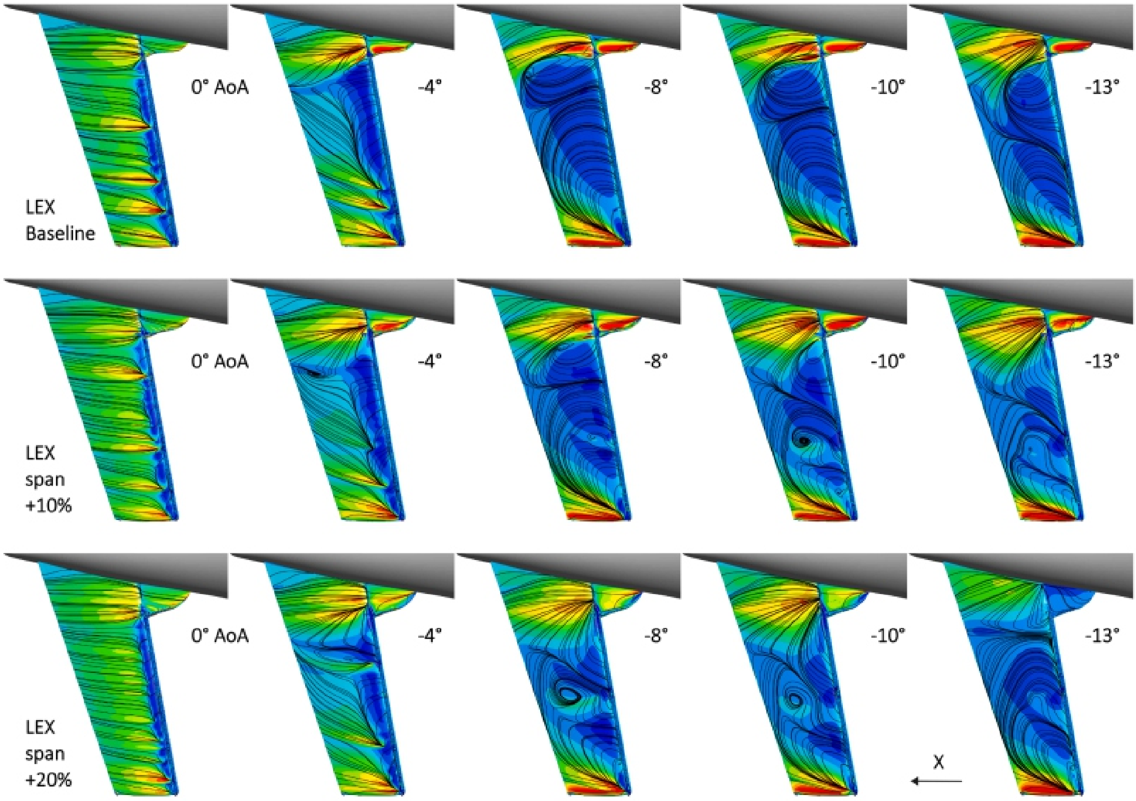

Fig. 38. Suction (lower) surface WSS_X colour plot, with the same scale as used throughout this paper, with surface WSS vector-based streamlines. The rows are the iced 10° FSHTs with baseline, plus 10 % span, and plus 20 % span LEXs. The columns are 0°, -4°, -8°, -10°, and -13° AoA.

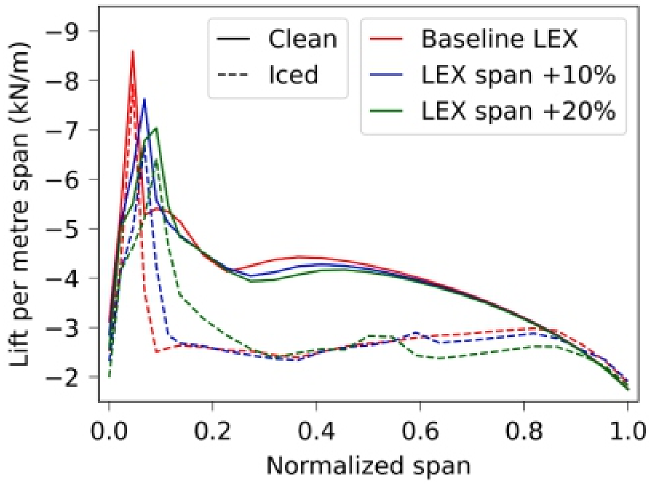

Fig. 39. Spanwise distribution of lift in the form of the integral of streamwise surface static pressure cuts, at -8° AoA.

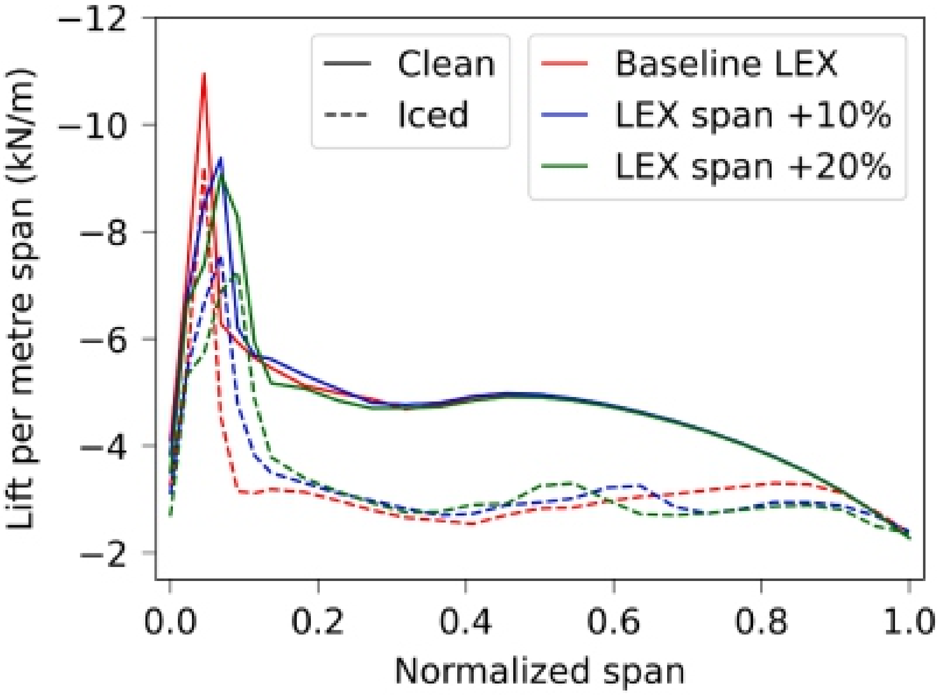

Fig. 40. Spanwise distribution of lift in the form of the integral of streamwise surface static pressure cuts, at -10° AoA.

chord, along with a variant without LEX for comparison. On the top level, the research finds iced CL to be fairly insensitive to the changes inLEX chord. While an advantage to having increased chord is observedbetween -8◦ and -10◦ AoA, the difference is only slight within thatnarrow AoA range. However, the advantage of the baseline LEX over noLEX, particularly at higher absolute AoA, is clearly shown. In moredetail, elongation of the iced LEX tends to lead to an increase in the highlift it provides and to increased spanwise extent of the tip leading edgevortex to higher absolute AoA. Both effects locally improve lifting performance. The changes are, however, more subtle than those seen in theforward sweep study and offset by reductions in lifting performanceelsewhere along the span. Nevertheless, the results shed more light onthe interplay between the inner and outer span flow and lift mechanismsand show LEX chord to have some influence over it. Without LEX, theouter-mid and ice tolerant outer span region iced lifting performance isat the upper end of the range seen with LEX and indeed more stable as

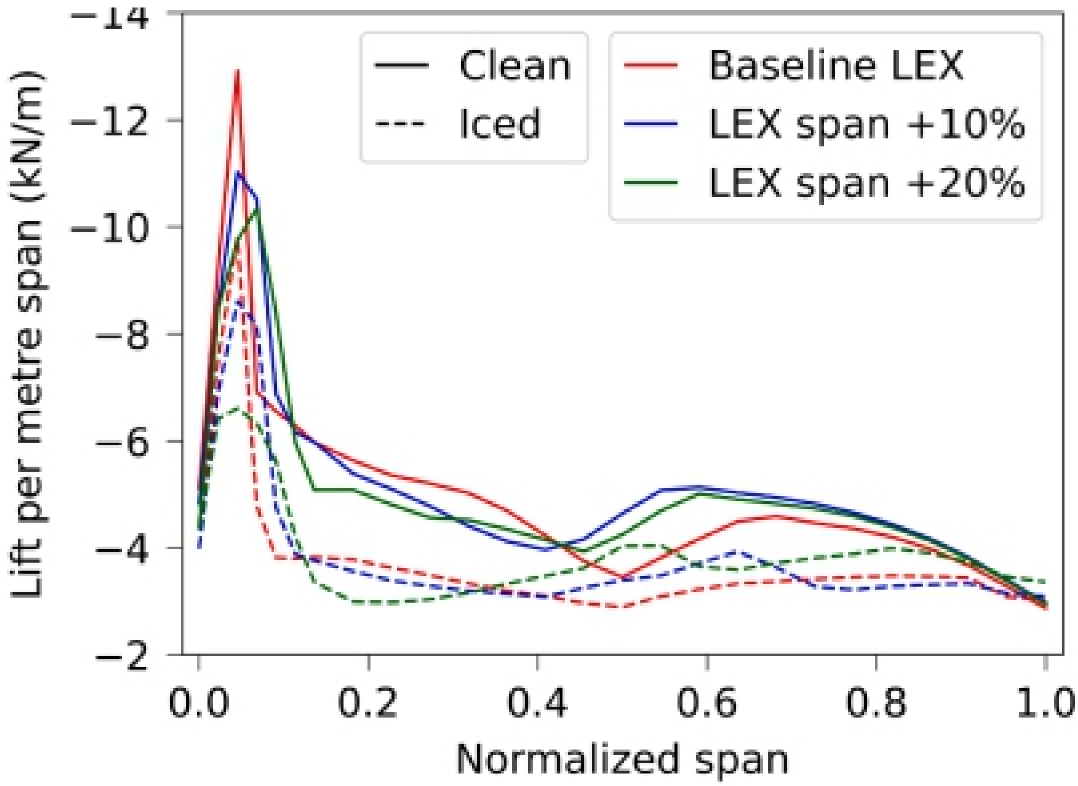

Fig. 41. Spanwise distribution of lift in the form of the integral of streamwise surface static pressure cuts, at -13° AoA.

absolute AoA is increased. However, the inner span iced lifting performance is comparably very low and noticeably deteriorates beyond -11◦ AoA. This demonstrates the value of the gothic LEX in icing conditions.The study of the effects of LEX span was carried out on the 10◦ FSHTwith three LEX variants: baseline, plus 10 % span, and plus 20 % span.On the top level, the research identifies a decrease in iced lifting performance with the increased LEX spans. The increase in LEX span leadsto more ice forming on the LEX. In terms of flow and lift, three trendsplay out as iced LEX span is increased. The first is reduced magnitudeand ice tolerance of the LEX lift spike. The second is increased spanwisecoverage of the root outward crossflow and associated local lift magnitude. The third is reduced spanwise range of the tip inward crossflow,reduced tip leading edge vortex stability, and reduced lift magnitude inthe outer-mid and ice tolerant outer span regions. A further noteworthyeffect is separation of the iced plus 20◦ span LEX flow at high AoA, which reduces LEX lift. This is in turn mitigated by reassertion ofthe tip leading edge vortex and ice tolerant outer span lift. The analysisconfirms the relevance of LEX span to iced lifting performance and icetolerance, and once again highlights the complexity of and trade-offposed by the interaction of the inner and outer span flows.

5. Conclusions

In this paper, research into the aerodynamics and low speed lifting capability of the advanced rear end forward swept horizontal tailplanewith leading edge extension for large passenger aircraft, following flightin icing conditions, has been presented. The flight condition in focus isthe roundout manouevre following 45 min in a holding pattern in Appendix C glaze icing conditions. The work includes: 1) a detailed proposal of best practice methodology for three-dimensional inflight icingsimulation of LPA empennages and aerodynamic CFD calculation of icedgeometries in the industrial environment, 2) an investigation into the effect of forward sweep variation on iced FSHT with LEX lifting performance, 3) an investigation into the effect of LEX chord variation oniced 10◦ FSHT lifting performance, 4) an investigation into the effect ofLEX span variation on iced 10◦ FSHT lifting performance, 5) a com parison of the iced FSHT lifting performance with and without LEX.

Theanalysis includes detailed inspection and discussion of negative CL andspanwise lift distribution of the clean and iced geometries, and the underlying three-dimensional flow mechanisms of the iced geometries. Thefindings offer new insight into aerodynamics, lifting capability and icetolerance of LPA FSHTs with LEXs.The methodology description shows the practice and feasibility ofthree-dimensional multishot icing simulation in the LPA design environment. Feasibility is achieved by limiting the icing simulation domain to only the empennage, using inlet boundary profiles calculated from full aircraft finite element method air flow and droplet calculations withsolution error-based mesh adaptation. The CFD domain includes the fullfuselage and iced FSHT without the main wings. The introduction recallsthe validation in [29] of the use of three-dimensional CFD with the k-ωSST turbulence model, in support of the CFD setup used for the clean andiced FSHT AoA sweeps.

The icing analysis displays the calculated three-dimensional ice shape for the FSHT with LEX, based on 45 min flight in a holding pattern,in representative Appendix C glaze icing conditions. The presence ofsignificant upper and lower horns in the glaze ice shape along theleading edge and minimal ice accretion on the LEX are confirmed. Theresults suggest that positioning the LEX in the fuselage shadow zone canbe effective in preventing ice accretion there.

The main flow mechanisms of an iced FSHT with LEX at zero to lowabsolute AoA are identified to be the LEX vortex, separation at the hornof the glaze ice shape, and small localized leading edge vorticesdistributed along the span with associated early reattachment points.The main flow mechanisms of an iced FSHT with LEX at moderate to high absolute AoA are identified to be the LEX vortex and associated LEX vortex suction surface 'root outward crossflow', a tightly wound tip leading edge vortex and associated suction surface 'tip inward crossflow', and the wingtip vortex.

Forward sweep is found to correlate positively with iced lifting performance and ice tolerance. Increased forward sweep is observed toincrease extension of the tip leading edge vortex and tip inward crossflow towards the wing root. This leads to significantly increased spanwise coverage of the suction surface low pressure region and associatedouter span ice tolerant lift region. In the highest sweep 20◦ FSHT case,the trend becomes more pronounced with increased absolute AoA overthe range studied. This is brought about by the extension of the tipleading edge vortex and tip inward crossflow all the way in adjacent tothe LEX vortex.

LEX chord variation is found to exert little effect on overall CL within the range considered. It is, however, found to influence the interplaybetween the LEX vortex and tip leading edge flow mechanisms, with alonger LEX promoting the spanwise reach of the latter. Given the potential observed for steps up and down in CL, it could therefore representa useful parameter for aerodynamic fine tuning.

The FSHT variant without LEX is found to have overall the lowest absolute CL due to its considerably inferior lift in the inner and inner-midspans. As absolute AoA is increased, the inner span lift eventually beginsto decrease,in contrast with that of the with-LEX variants. This leads tocomparatively even poorer lifting performance of the no-LEX variant.LEX span variation is found to be influential on iced FSHT liftingperformance. Increased LEX span leads to more local ice accretion withmore complex shapes forming. The variants with increased LEX spanhave lower absolute CL values throughout the AoA range than thebaseline LEX. Increased LEX span tends to result in reduced ice toleranceof the LEX lift spike and, in the plus 20 % span case, separation of theLEX flow at -13◦ AoA. It also promotes increased spanwise extent of theroot outward crossflow and destabilization of the tip leading edge vor tex, which improves inner span and degrades outer span iced lift, withan overall negative effect.

The research shows the potential for three-dimensional inflight icing simulation and CFD to play a role in LPA empennage research anddesign. It also provides insight into FSHT with LEX iced low speed liftingperformance and brings forth new understanding of a hitherto unexplored area of iced horizontal stabilizer aerodynamics. Research intoiced low speed lifting performance of conventional horizontal stabilizergeometry for a comparative study is ongoing. With plenty to explore inLPA empennage and

CRediT authorship contribution statement

James H. Page: Writing – review & editing, Writing – original draft, Visualization, Methodology, Formal analysis, Data curation, Conceptualization. Isik Ozcer: Writing – review & editing, Visualization, Validation, Software, Methodology, Formal analysis, Data curation,Conceptualization. Alessandro Zanon: Writing – review & editing,Methodology, Funding acquisition, Formal analysis, Conceptualization.Michele De Gennaro: Writing – review & editing, Supervision, Projectadministration, Funding acquisition, Conceptualization. Raul C.Llamas-Sandin: Writing – review & editing, Supervision,Conceptualization.

Declaration of competing interest

The authors declare the following financial interest/personal relationship which may be considered as a potential competing interest: Raul Llamas Sandin has patent US 2010/0148000 A1 licensed to Airbus Espania S.L.

Acknowledgements

The creation and provision of the FSHT geometries for short-medium range LPA by Salvatore Corcione, Vincenzo Cusati, and Fabrizio Nicolosifrom University of Naples is gratefully acknowledged.

Funding

This project has received funding from the European Union's Horizon 2020 research and innovation funding programme under Grant Agreement No. 885052. This publication reflects only the author's view.The European Commission and the Clean Sky 2 (Clean Aviation) JointUndertaking are not responsible for any use that may be made of theinformation it contains.

Data availability

The data that has been used is confidential.

References

[1] European Commission, Reducing emissions from aviation, 2024. [Online]. Available: https://climate.ec.europa.eu/eu-action/transport/reducing-emissions-aviation_en.

[2] R.C. Miake-Lye, D. Hauglustaine, Innovation for a green transition, ICAO (2022).

[3] ECAC.CEAC, Report on standard method of computing volume 1: applicationsguide, ECAC.CEAC Doc 29 4th Edition, 2016.

[4] EUROCONTROL, Forecast update 2024-2030, 2024.

[5] European Commission, Communication from the commission to EuropeanParliament, the European Council, the Council, the European Economic and SocialCommittee and the Committee of the Regions, The European green deal, EuropeanCommission, Brussels, 2019.

[6] N.G.M. Moirou, D.S. Sanders, P. Laskaridis, Advancements and prospects ofboundary layer ingestion propulsion concepts, Progress in Aerospace Sciences 138(2023) 100897, https://doi.org/10.1016/j.paerosci.2023.100897.

[7] Z. Lyu, J.R.R.A. Martins, Aerodynamic design optimization studies of a blendedwing-body aircraft, Journal of Aircraft 51 (5) (2014), https://doi.org/10.2514/1.C032491.

[8] E.J. Adler, J.R.R.A. Martins, Hydrogen-powered aircraft: fundamental concepts,key technologies, and environmental impacts, Progress in Aerospace Sciences 141(2023) 100922, https://doi.org/10.1016/j.paerosci.2023.100922.

[9] Y. Ma, A. Elham, Designing high aspect ratio wings: a review of concepts andapproaches, Progress in Aerospace Sciences 145 (2024) 100983, https://doi.org/10.1016/j.paerosci.2024.100983.

[10] S. Corcione, V. Cusati, V. Memmolo, F. Nicolosi, R.Llamas Sandin, Impact ataircraft level of elastic efficiency of a forward-swept tailplane, Aerospace Scienceand Technology 140 (2023) 108461, https://doi.org/10.1016/j.ast.2023.108461.

[11] S. Corcione, V. Cusati, F. Nicolosi, Aerodynamic design of advanced rear end for large passenger aircraft, Materials Research Proceedings (2023), https://doi.org/ 10.21741/9781644902813-96.

[12] S. Corcione, M. Mandorino, V. Cusati, Beyond conventional: an integrated aerostructural optimization approach, Aerospace Science and Technology 150 (2024) 109242, https://doi.org/10.1016/j.ast.2024.109242.

[13] R. Llamas Sandin, M. Luque Buzo, Aircraft horizontal stabilizer surface. United States Patent US 2010/0148000 A1, 17 June 2010.

[14] I.R. Whitehouse, C. Weber, M. Fischer, A. Tanguy, Aircraft horizontal stabiliser fitted with leading-edge strake. United States Patent US 2012/0205490 A1, 16 August 2012.

[15] U.S. Department of Transportation Federal Aviation Administration, Advisory Circular AC No:

25-25A, 2014.

[16] Y. Cao, W. Tan, Z. Wu, Aircraft icing: an ongoing threat to aviation safety, Aerospace Science and Technology 75 (2018) 353–385, https://doi.org/10.1016/j.ast.2017.12.028.

[17] Federal Aviation Administration (FAA), Code of federal regulations: title 14,chapter I, subchapter C, part 25, appendix C to part 25, 2024. [Online]. Available:https://www.ecfr.gov/current/title-14/chapter-I/subchapter-C/part-25/appendixAppendix%20C%20to%20Part%2025.

[18] J. Page, I. Ozcer, A. Zanon, M. De Gennaro, IMPACT: Numerical study ofaerodynamics of an iced forward-swept tail with leading edge extension, SAETechnical Paper 2023-01-1371, in: International Conference on Icing of Aircraft,Engines, and Structures, 2023, https://doi.org/10.4271/2023-01-1371.

[19] A. Pueyo, I. Ozcer, G. Baruzzi, An Eulerian approach with mesh adaptation forhighly accurate 3D droplet dynamics simulations, SAE Technical Paper 2019-01-2012, in: International Conference on Icing of Aircraft, Engines, and Structures,2019, https://doi.org/10.4271/2019-01-2012.

[20] O.J. Kwon, L.N. Sankar, Numerical study of the effects of icing on fixed and rotarywing performance, in: 29th Aerospace Sciences Meeting, 1991, https://doi.org/10.2514/6.1991-662.

[21] M.B. Bragg, A.B. Broeren, L.A. Blumenthal, Iced-airfoil aerodynamics, Progress inAerospace Sciences 41 (5) (2005) 323–362, https://doi.org/10.1016/j.paerosci.2005.07.001.

[22] M.B. Bragg, W. Yoshida, A.P. Broeren, S. Lee, B.S. Woodard, Ice shape classificationfor swept wings, in: AIAA AVIATION 2020 FORUM, 2020, https://doi.org/10.2514/6.2020-2845.

[23] A.P. Broeren, S. Lee, B.S. Woodard, M.B. Bragg, Effect of geometric fidelity on theaerodynamics of a swept wing with glaze ice accretion, in: AIAA AVIATION 2020FORUM, 2020, https://doi.org/10.2514/6.2020-2846.

[24] Y. Bourgault, Z. Boutanios, W.G. Habashi, Three-dimensional Eulerian approach todroplet impingement simulation using FENSAP-ICE, part 1: model, algorithm, andvalidation, Journal of Aircraft 37 (1) (2000), https://doi.org/10.2514/2.2566.

[25] F. Morency, H. Beaugendre, G. Baruzzi, W. Habashi, FENSAP-ICE - acomprehensive 3D simulation system for in-flight icing, in: 15th AIAAComputational Fluid Dynamics Conference, 2001, https://doi.org/10.2514/6.2001-2566.

[26] H. Beaugendre, F. Morency, W.G. Habashi, FENSAP-ICE's three-dimensional inflight ice accretion module: ICE3D, Journal of Aircraft 40 (2) (2003), https://doi.org/10.2514/2.3113.

[27] C.N. Aliaga, M.S. Aub´e, G.S. Baruzzi, W.G. Habashi, S. Nadarajah, A thirdgeneration in-flight icing code: FENSAP-ICE-unsteady, SAE Technical Paper 2007-01-3339, in: SAE Aircraft & Engine Icing International Conference, 2007, https://doi.org/10.4271/2007-01-3339.

[28] D.Switchenko Ozcer, G.S. Baruzzi, J. Chen, Multi-shot icing simulations withautomatic re-meshing, SAE Technical Paper 2019-01-1956, in: InternationalConference on Icing of Aircraft,

Engines, and Structures, 2019, https://doi.org/ 10.4271/2019-01-1956.

[29] A.Pueyo Ozcer, F. Menter, S. Hafid, H. Yang, Numerical study of iced swept-wing performance degradation using RANS, SAE Technical Paper 2023-01-1402, in:International Conference on Icing of Aircraft, Engines, and Structures, 2023,https://doi.org/10.4271/2023-01-1402.

[30] A.P. Broeren, M.G. Potapczuk, S. Lee, A.M. Malone, B.P. Paul, B. Woodard, Iceaccretion test results for three large-scale swept-wing models in the NASA IcingResearch Tunnel, AIAA 2016-3733, in: 8th AIAA Atmospheric and SpaceEnvironments Conference, 2016, https://doi.org/10.2514/6.2016-3733.

[31] A.P. Broeren, B.S. Woodard, J.M. Diebold, F. Moens, Low-Reynolds numberaerodynamics of an 8.9% scale semispan swept wing for assessment of icing effects,AIAA 2017-4372, in: 9th AIAA Atmospheric and Space Environments Conference,2017, https://doi.org/10.2514/6.2017-4372.

[32] S.C. Camello, M.B. Bragg, A.P. Broeren, C.W Lum, B.S. Woodard, S. Lee, Effect ofice shape fidelity on swept-wing aerodynamic performance, AIAA 2017-4373, in:9th AIAA Atmospheric and Space Environments Conference, 2017, https://doi.org/10.2514/6.2017-4373.

[33] C.W. Lum, N. Sandhu, J.M. Diebold, B.S. Woodard, M.B. Bragg, The application ofa five-hole probe wake-survey technique to the study of swept wing icingaerodynamics, AIAA 2017-4374, in: 9th AIAA Atmospheric and SpaceEnvironments Conference, 2017, https://doi.org/10.2514/6.2017-4374.

[34] N. Sandhu, M.R. Soltani, M.B. Bragg, C.W. Lum, B.S. Woodard, A.P. Broeren, S. Lee,Effect of simulated scalloped ice on the aerodynamics of a swept-wing at low Reynolds number, AIAA 2018-3495, in: AIAA Atmospheric and Space Environments Conference, 2018, https://doi.org/10.2514/6.2018-3495.

[35] B. Aupoix, P.R. Spalart, Extensions of the Spalart–Allmaras turbulence model to account for wall roughness, International Journal of Heat and Fluid Flow 24 (4) (2003) 454–462, https://doi.org/10.1016/S0142-727X(03)00043-2.

[36] F.R. Menter, Improved two-equation k-ω turbulence models for aerodynamic flows, NASA-TM-103975, NASA (1992).

[37] C.N. Aliaga, G.S. Baruzzi, J. Chen, J. Selvanayagam, I.A. Ozcer, J. Stokes, Automatic mesh optimization for wing-fuselage juncture flow separation predictions, AIAA 2020-2750, in: AIAA Aviation 2020 Forum, 2020, https://doi. org/10.2514/6.2020-2750.

[38] J. Selvanayagam, C. Aliaga, J. Stokes, CFD simulation of ground vortex intake test case using ANSYS FLUENT, AIAA 2022-0222, in: AIAA SciTech 2022 Forum, 2022,https://doi.org/10.2514/6.2022-0222.

[39] K. Zore, A. Matyushenko, S. Shah, C. Aliaga, J. Stokes, F. Menter, Laminarturbulent transition prediction on industrial CFD applications, AIAA 2022-1954, in:AIAA SciTech 2022 Forum, 2022,

1954.

[40] C. Aliaga, M. Kopp, K.B. Salui, D. Mahapatra, A. Sardesai, R. Ranjith, Aerodynamic and stealth studies of canard-wing configurations at transonic speeds using AnsysFluent & Ansys HFSS SBR+, AIAA 2022-3322, in: AIAA Aviation 2022 Forum,2022, https://doi.org/10.2514/6.2022-3322.

Instructions for Authors

Essentials for Publishing in this Journal

1 Submitted articles should not have been previously published or be currently under consideration for publication elsewhere.

2 Conference papers may only be submitted if the paper has been completely re-written (taken to mean more than 50%) and the author has cleared any necessary permission with the copyright owner if it has been previously copyrighted.

3 All our articles are refereed through a double-blind process.

4 All authors must declare they have read and agreed to the content of the submitted article and must sign a declaration correspond to the originality of the article.

Submission Process

All articles for this journal must be submitted using our online submissions system. http://enrichedpub.com/ . Please use the Submit Your Article link in the Author Service area.

Manuscript Guidelines

The instructions to authors about the article preparation for publication in the Manuscripts are submitted online, through the e-Ur (Electronic editing) system, developed by **Enriched Publications Pvt. Ltd**. The article should contain the abstract with keywords, introduction, body, conclusion, references and the summary in English language (without heading and subheading enumeration). The article length should not exceed 16 pages of A4 paper format.

Title

The title should be informative. It is in both Journal's and author's best interest to use terms suitable. For indexing and word search. If there are no such terms in the title, the author is strongly advised to add a subtitle. The title should be given in English as well. The titles precede the abstract and the summary in an appropriate language.

Letterhead Title

The letterhead title is given at a top of each page for easier identification of article copies in an Electronic form in particular. It contains the author's surname and first name initial .article title, journal title and collation (year, volume, and issue, first and last page). The journal and article titles can be given in a shortened form.

Author's Name

Full name(s) of author(s) should be used. It is advisable to give the middle initial. Names are given in their original form.

Contact Details

The postal address or the e-mail address of the author (usually of the first one if there are more Authors) is given in the footnote at the bottom of the first page.

Type of Articles

Classification of articles is a duty of the editorial staff and is of special importance. Referees and the members of the editorial staff, or section editors, can propose a category, but the editor-in-chief has the sole responsibility for their classification. Journal articles are classified as follows:

Scientific articles:

1. Original scientific paper (giving the previously unpublished results of the author's own research based on management methods).

2. Survey paper (giving an original, detailed and critical view of a research problem or an area to which the author has made a contribution visible through his self-citation);

3. Short or preliminary communication (original management paper of full format but of a smaller extent or of a preliminary character);

4. Scientific critique or forum (discussion on a particular scientific topic, based exclusively on management argumentation) and commentaries. Exceptionally, in particular areas, a scientific paper in the Journal can be in a form of a monograph or a critical edition of scientific data (historical, archival, lexicographic, bibliographic, data survey, etc.) which were unknown or hardly accessible for scientific research.

Professional articles:

1. Professional paper (contribution offering experience useful for improvement of professional practice but not necessarily based on scientific methods);
2. Informative contribution (editorial, commentary, etc.);
3. Review (of a book, software, case study, scientific event, etc.)

Language

The article should be in English. The grammar and style of the article should be of good quality. The systematized text should be without abbreviations (except standard ones). All measurements must be in SI units. The sequence of formulae is denoted in Arabic numerals in parentheses on the right-hand side.

Abstract and Summary

An abstract is a concise informative presentation of the article content for fast and accurate Evaluation of its relevance. It is both in the Editorial Office's and the author's best interest for an abstract to contain terms often used for indexing and article search. The abstract describes the purpose of the study and the methods, outlines the findings and state the conclusions. A 100- to 250-Word abstract should be placed between the title and the keywords with the body text to follow. Besides an abstract are advised to have a summary in English, at the end of the article, after the Reference list. The summary should be structured and long up to 1/10 of the article length (it is more extensive than the abstract).

Keywords

Keywords are terms or phrases showing adequately the article content for indexing and search purposes. They should be allocated heaving in mind widely accepted international sources (index, dictionary or thesaurus), such as the Web of Science keyword list for science in general. The higher their usage frequency is the better. Up to 10 keywords immediately follow the abstract and the summary, in respective languages.

Acknowledgements

The name and the number of the project or programmed within which the article was realized is given in a separate note at the bottom of the first page together with the name of the institution which financially supported the project or programmed.

Tables and Illustrations

All the captions should be in the original language as well as in English, together with the texts in illustrations if possible. Tables are typed in the same style as the text and are denoted by numerals at the top. Photographs and drawings, placed appropriately in the text, should be clear, precise and suitable for reproduction. Drawings should be created in Word or Corel.

Citation in the Text

Citation in the text must be uniform. When citing references in the text, use the reference number set in square brackets from the Reference list at the end of the article.

Footnotes

Footnotes are given at the bottom of the page with the text they refer to. They can contain less relevant details, additional explanations or used sources (e.g. scientific material, manuals). They cannot replace the cited literature.

The article should be accompanied with a cover letter with the information about the author(s): surname, middle initial, first name, and citizen personal number, rank, title, e-mail address, and affiliation address, home address including municipality, phone number in the office and at home (or a mobile phone number). The cover letter should state the type of the article and tell which illustrations are original and which are not.

Note